

The deep sea mining horizontal discharge plume

Small-scale experiments and modelling

B. K. Blankenaar

The deep sea mining horizontal discharge plume

Small-scale experiments and modelling

by

B. K. Blankenaar

to obtain the degree of Master of Science
at the Delft University of Technology

Student number: 4281322
Project duration: September 2, 2019 – June 23, 2020
Thesis committee: Dr. ir. A. M. Talmon, TU Delft
Dr. ir. R. L. J. Helmons, TU Delft
Ir. A. Posthuma, Allseas
Ir. F. van Grunsven, Allseas

This thesis is confidential and cannot be made public until June 23, 2022.

An electronic version of this thesis is available at <http://repository.tudelft.nl/>.



Preface

This master thesis deals with the reduction of the spreading of the horizontal discharge plume created during the mining of manganese nodules from the deep sea. It is written as the final part of the Master Offshore and Dredging Engineering from the Delft University of Technology.

I would like to thank Allseas Engineering for providing me with the chance of graduating at their company. Furthermore, I would like to thank the members of my graduation committee, Dr. Ir. Arno Talmon, Dr. Ir. Rudy Helmons, Ir. Andrys Posthuma and Ir. Frans van Grunsven for their input throughout my research.

I want to thank Freek Brakel, Ed Stok and Andre van den Bosch, who helped with repairing and adjusting the experimental setup. Also, I would like to thank Koen Deckers for assisting me with all the experiments.

I would like to thank my family and friends for their support to keep me motivated to finish my thesis.

*B. K. Blankenaar
Delft, June 2020*

Abstract

The rising demand for minerals and metals and the depletion of land-based resources has created a renewed interest in the extraction of resources from the deep ocean, i.g., deep sea mining. This research focuses on the mining of manganese nodules. Manganese nodule are potato-shaped objects composed of metals half buried in the seafloor. The majority are 5-10cm in size. A Seafloor Mining Tool (SMT) is used to mine the nodules, however, during mining besides the nodules, also the sediment around the nodules is collected. This sediment is separated in the SMT and discharged through a horizontal diffuser located at the rear of the SMT, thereby creating a sediment plume. The sediment plume needs to be reduced for environmental, economic and legal reasons. The sediment plume causes changes in the sediment characteristics, clogging of pores of suspension feeding organisms and burying of the benthic fauna. The plume will spread in all directions, thereby burying still to be collected nodules and reducing the pick-up efficiency, making the process inefficient from an economical perspective. Legal issues will arise when the discharged sediment plume spreads to other exploration areas owned by other parties or to environmentally protected areas. The aim of this research is to investigate the influence of the choice of diffuser height on the reduction of the sediment plume.

To achieve this goal a Matlab model was made and small-scale experiments in the laboratory of Dredging Engineering were done. The Matlab model is based on the JETLAG model, described in 'Jets and Plumes' by Lee and Chu (2003), and is a Lagrangian model predicting the centerline trajectory of the plume. The small-scale experiments provide insight in the behaviour of the horizontal discharge plume at different diffuser heights and generate measurements to validate the model. A diffuser designed specifically for these experiments is produced and the height and flow velocity are differed. The experiments consist of visualization experiments, capturing top view and side view images of the buoyant jet, and experiments measuring the velocity and bottom concentration at different locations.

The velocity profiles, sediment concentration, deposition pattern and impingement range are compared and analysed. The combined results from the model and the experiments show that the start of the impingement range increases with increasing diffuser height. Furthermore, a lower diffuser height increases the amount of bottom deposition near the diffuser outlet. The measured velocity profiles, near bottom concentration and impingement range are in agreement with this observation. The measured near bottom velocities at 15D from the diffuser outlet are approximately 0.1 and 0.2m/s, depending on the discharge velocity, both have the potential of resuspending settled sediment.

This research suggests that the spreading of the plume can be reduced by the choice of diffuser height above the seafloor. Based on the diffuser heights tested in this research a diffuser height of 100mm is recommended. Since a higher diffuser decreases the amount of particles settling close to the source and a lower diffuser increases the potential for erosion. This research has shown that up to a distance of 15D from the diffuser, the near bottom velocities are large enough to cause erosion. Research into the near bottom velocity decay and magnitude further away from the source, inside the turbidity current, is necessary as well to understand the full spreading behaviour and the potential for erosion. Furthermore it is recommended to do research into spreading behaviour of finer particles, especially the behaviour of the actual deep sea sediment in combination with salt water causing flocculation. Moreover, research into the influence of the forward motion of the SMT is recommended since the SMT will create a wake that will influence the spreading behaviour of the plume. Research into the potential creation of a recirculation region caused by the limited entrainment at the rear of the SMT is recommended as well, this can be done by aligning the diffuser outlet with a screen.

Contents

Preface	iii
Abstract	v
List of Figures	xi
List of Tables	xv
1 Introduction	1
1.1 Background	1
1.2 Problem statement	2
1.3 Research questions	3
1.4 Research methodology	3
1.5 Thesis outline	4
2 Environmental impact	5
2.1 Deep sea mining sediment plume.	5
2.2 Discharge plume impact	5
2.3 Regulation	6
3 Jets and Plumes	9
3.1 What are jets and plumes?	9
3.1.1 Classification	9
3.1.2 Flow regions	9
3.2 Behaviour.	10
3.2.1 Turbulent entrainment.	10
3.2.2 Terminology	11
3.2.3 Velocity and Concentration Profiles	12
3.2.4 Densimetric Froude number.	13
3.3 Sediment-laden jet	13
3.4 Submerged offset jet	14
3.5 Diffuser	14
3.6 Conclusion	16
4 Influencing parameters	17
4.1 SMT variables.	17
4.1.1 Suspended Sediment Concentration.	17
4.1.2 Discharge Velocity	18
4.1.3 Diffuser Geometry	18
4.1.4 SMT velocity	19
4.2 Local conditions	19
4.2.1 Current	19
4.2.2 Temperature, salinity and turbidity profiles	19
4.2.3 Bottom topography	19
4.2.4 Sediment.	20
4.3 Conclusion	20
5 Lagrangian numerical model	21
5.1 Model explanation	21
5.1.1 Description	21
5.1.2 Input and output.	23
5.1.3 Adaptations and assumptions	23

5.2	Model formulation	24
5.3	Verification	25
6	Experiment	27
6.1	Experiment purpose	27
6.2	Experiment setup	27
6.3	Experiment execution.	29
6.4	Measurement instruments	29
6.4.1	Acoustic Doppler Velocimetry sensor	30
6.4.2	High speed camera and GoPro	30
6.4.3	KATflow 200	30
6.4.4	Aquatic turbidimeter.	31
6.5	Particle choice	31
6.6	Diffuser design	33
6.7	Test matrix	33
6.8	Suspended sediment concentration.	34
7	Results experiment	37
7.1	Results	37
7.1.1	Concentration	37
7.1.2	Velocity profile	37
7.1.3	Bottom deposition pattern.	39
7.1.4	Impingement range	39
7.1.5	Comparison particle sizes	40
7.1.6	Densimetric Froude number <1	42
7.2	Troubleshooting	43
7.2.1	Fall-out of sediment at diffuser outlet	43
7.2.2	Erroneous velocity profile	45
7.3	Analysis	47
7.3.1	Velocity	47
7.3.2	Concentration	49
7.3.3	Bottom deposition pattern.	49
7.3.4	Impingement range	51
8	Results model	53
8.1	Trajectory	53
8.2	Suspended sediment concentration.	53
8.3	Velocity	54
8.4	Impingement range	55
8.4.1	Deposition width to impingement range ratio	56
9	Discussion	57
9.1	Results	57
9.1.1	Velocity	57
9.1.2	Concentration	58
9.1.3	Bottom deposition pattern.	58
9.1.4	Impingement range	58
9.2	Limitations and recommendations	58
9.2.1	Experiment	59
9.2.2	Model	60
10	Conclusion and recommendations	61
10.1	Conclusion	61
10.2	Recommendations	62

Bibliography	63
A Results experiment	67
A.1 Concentration	67
A.2 Velocity	68
A.2.1 SNR profile.	68
A.2.2 Velocity profile.	69
A.3 Bottom deposition pattern	70
A.4 Impingement range.	71
B Results model	73

List of Figures

1.1	World map showing the locations where poly-metallic nodules (blue), poly-metallic sulphides/vents (orange) and cobalt-rich crusts (yellow) can be found [31].	1
1.2	Outside and slice through of a manganese nodule [38].	1
1.3	A deep sea mining system overview for mining manganese nodules (adapted from [15])	2
3.1	Flow regions and the characteristic length and time scales of these regions [9]	10
3.2	Schematic drawing of the turbulent entrainment of ambient fluid by eddies [21]	11
3.3	Schematic overview of the development of a jet, with u_0 , c_0 and d_0 respectively the initial velocity, concentration and slot height, $2r$ the width of the potential core and $b(x)$ the plume half width [25]	11
3.4	Example of a Gaussian and top-hat profile [25]	12
3.5	Schematic overview of the flow zones in a submerged offset jet [22]	14
3.6	Geometry of a flat-walled diffuser, where b is the width, W is the height, L is the length and θ is the diffuser angle [42]	15
3.7	Stability map for flat-walled diffusers [42]	15
3.8	Steps in flow separation; PI is point of inflection: (A) zero gradient: no separation, PI at the wall, (B) weak adverse gradient: no separation, PI in the flow (C) critical adverse gradient: separation (D) excessive adverse gradient: separation and backflow at the wall [16]	15
4.1	Slice through of the buoyant jet, particles will start to drop out if $\omega_s \sin(\psi_c) > v_e$, where ω_s is the settling velocity, ψ_c is the spread angle and v_e the entrainment velocity [27]	18
5.1	Lagrangian formulation of the motion of a plume element through time [25]	21
5.2	Overview of the physical processes determining the plume element at the next time step	22
5.3	Mixing of fluid in an elemental volume carrying mass \bar{M} and concentration \bar{c} with an ambient fluid volume carrying mass $\delta\bar{M}$ and concentration c_a [25]	23
5.4	Input and output parameters of the MATLAB model	23
5.5	Comparison of the predicted dilution of the explained model, called Model 2020, with the predicted dilution from the JETLAG model and measurements for a horizontal buoyant jet in still fluid, where S_c is the centerline dilution, made dimensionless by Q_0 the initial volume flux, F_0 the initial buoyancy flux and M_0 the initial momentum flux	26
5.6	Centerline trajectory of a horizontal round buoyant jet in stagnant fluid, comparison between the model prediction of the explained model, called Model 2020, and experimental data from Lee and Chu [25] for (a) $Fr=2$ and (b) $Fr=10$	26
6.1	Schematic drawing of the (a) front view and (b) top view of the flume	28
6.2	Location of the five sample points to determine the concentration, the indicated distances are in millimeters	29
6.3	Test set up for the (a) experiments and (b) visualization experiments	29
6.4	Error of the 1-30s, 30-60s, 60-90s average velocities with respect to the average velocity over 90-120s divided by the 90-120s average velocity for one measurement height	30
6.5	The ADV sensor	31
6.6	High speed camera position during testing	31
6.7	Attachment of the transducers to the PVC pipe	31
6.8	The control module of the flow meter	31
6.9	The Aqualitic turbidimeter [41]	32
6.10	Turbidity to concentration conversion	32
6.11	Cumulative particle size distribution for 40-70 μm (black) and 65-105 μm (blue)	33
6.12	Diffuser design	33

6.13	Measurements of the reservoir concentration over the duration of one test	35
7.1	Dimensionless SSC at the sample locations 1, 2, 3 and 4 compared to the background concentration for test 10 ($h=100$ mm, $u_0=0.27$ m/s)	38
7.2	Velocity profile for experiment 10, 11 and 12, where $z/D=0$ is the center of the diffuser exit, the dotted lines indicate the diffuser boundaries, the lower bound of the y-axis is the location of the bottom boundary and the red arrows resemble less reliable measurements	38
7.3	Velocity profile in x-direction at 50D from the impingement point, the red arrows resemble less reliable measurements	38
7.4	Velocity profile for test 10 in (a) x-direction (b) y-direction and (c) z-direction	39
7.5	Image processing steps to determine the bottom deposition pattern, with (a) the base frame, (b) the superposed image, and (c) the final filtered image at $t=420$ s	40
7.6	Bottom deposition pattern through time, experiment 18	40
7.7	Bottom deposition pattern for both particle sizes, 65-105 micron in black and 40-70 micron in blue, and an initial velocity of (a) 0.27m/s and (b) 0.37m/s at $t=420$ s	41
7.8	Filtered average image of bottom deposition for a particle size of (a) 65-105 micron, test 18 and (b) 40-70 micron, test 30 at $t=420$ s	41
7.9	Averaged image of the high speed camera footage for a densimetric Froude number of (a) 0.5 and (b) 3.5	42
7.10	GoPro image of the average image relative to the background, the diffuser can be seen on the right and the slightly darker spots in front of the diffuser is the buoyant jet	43
7.11	Sediment fallout	44
7.12	Velocity profile of the velocity in x-direction at the diffuser outlet for an initial velocity of (a) 0.27m/s and (b) 0.37m/s	45
7.13	Measurement locations of the measured velocity profiles above the diffuser and buoyant jet	45
7.14	Profile of the (a) x velocity and (b) SNR above the buoyant jet	46
7.15	Profile of the (a) x velocity and (b) SNR above the diffuser	46
7.16	Velocity profile at different measurement locations for an offset ratio of (a) OR=7.33, (b) OR=4 and (c) OR=2.33, the dotted lines indicate the diffuser boundaries, the red data points are considered less reliable, $u_0=0.27$ m/s	48
7.17	Velocity profile at different measurement locations for an offset ratio of (a) OR=7.33, (b) OR=4 and (c) OR=2.33, the dotted lines indicate the diffuser boundaries, the red data points are considered less reliable, $u_0=0.37$ m/s	48
7.18	SSC at the bottom boundary with increasing distance x/D for different offset ratios and an initial velocity of (a) 0.27m/s and (b) 0.37m/s	49
7.19	Bottom deposition pattern for different offset ratios at $t=420$ s, (a) $u_0=0.27$ m/s and (b) $u_0=0.37$ m/s	50
7.20	Averaged image of the top view of the bottom deposition pattern with an initial velocity of 0.27m/s at $t=420$ s, (a) test 8 OR=7.33, (b) test 18 OR=4, and (c) test 26 OR=2.33	51
7.21	Comparison of the start of the impingement range for the three tested offset ratios	51
8.1	Model and experiment results of the buoyant jet trajectory for $u_0=0.27$ m/s	53
8.2	Model and experiment results of the average suspended solid concentration for $u_0=0.27$ m/s	54
8.3	Model and experiment results for $u_0=0.27$ m/s, (a) average x-velocity evolution and (b) average z-velocity evolution	55
9.1	Schematic overview of the flow zones in a submerged offset jet [22]	58
A.1	Dimensionless SSC at the sample locations 1, 2, 3, 4 and 5 compared to the background concentration for (a) experiment 1, $h=200$ mm and $u_0 = 0.27$ m/s, (b) experiment 4, $h=200$ mm and $u_0 = 0.37$ m/s, (c) experiment 14, $h=100$ mm and $u_0 = 0.37$ m/s, (d) experiment 20, $h=50$ mm and $u_0 = 0.27$ m/s, and (e) experiment 23 $h=50$ mm and $u_0 = 0.37$ m/s	67
A.2	SNR profile for (a) test 10, (b) test 11 and (c) test 12	68
A.3	Velocity profile at different measurement locations for (a) test 1, 2 and 3, (b) test 4, 5 and 6, (c) 14, 15 and 16, (d) 20, 21 and 22, and (e) 23, 24 and 25; where the dotted lines indicate the diffuser boundaries	69

A.4	Time evolution of the bottom deposition pattern for (a) test 8, $h=200\text{mm}$ and $u_0=0.27\text{m/s}$, (b) test 9, $h=200\text{mm}$ and $u_0=0.37\text{m/s}$, (c) test 19, $h=100\text{mm}$ and $u_0=0.37\text{m/s}$, (d) test 26, $h=50\text{mm}$ and $u_0=0.27\text{m/s}$, and (e) test 27, $h=50\text{mm}$ and $u_0=0.37\text{m/s}$	70
B.1	Model and experiment results of the buoyant jet trajectory for $u_0=0.37\text{m/s}$	73
B.2	Model and experiment results of the average suspended solid concentration for $u_0=0.37\text{m/s}$	73
B.3	Model and experiment results for $u_0=0.37\text{m/s}$, (a) average x-velocity evolution, and (b) average z-velocity evolution	74

List of Tables

3.1	Flow classification based on source type and source duration [25]	9
6.1	Test matrix	34
7.1	Comparison of the impingement point for a particle size of 40-70 micron and 65-105 micron	42
8.1	The start of the impingement range calculated by the model and determined through experiments	56
8.2	Ratio of the deposition width of the experiments over the model prediction of the length of the impingement range	56
A.1	Approximate start of the impingement range (x/D) for different experiments, with in red the experiments for a particle size of 40-70 micron	71

Acronyms

- ADV** Acoustic Doppler Velocimetry. 30, 34, 44, 46, 62
- BBL** Bottom Boundary Layer. 19, 20
- CCZ** Clarion Clipperton Zone. 7
- CFD** Computational Fluid Dynamics. 19, 59
- ISA** International Seabed Authority. 6, 7
- MIDAS** Managing Impacts of Deep-sea resource exploitation. 19
- NTU** Nephelometric Turbidity Units. 31, 32, 37
- OR** Offset Ratio. 47
- PSD** Particle Size Distribution. 31, 32
- SMS** Seafloor Massive Sulphides. 1
- SMT** Seafloor Mining Tool. v, 2, 5, 6, 9, 13, 14, 16, 17, 19, 20, 27, 33, 57–59, 61, 62
- SNR** Signal-to-Noise Ratio. 45, 46
- SSC** Suspended Sediment Concentration. 17, 20, 34, 37, 49, 53, 59, 61
- SWOE** Sediment, Waste, and Other Effluents. 2, 5
- UNCLOS** United Nations Convention on the Law of the Sea. 6
- VTS** Vertical Transport System. 2
- ZEF** Zone of Established Flow. 11, 22
- ZFE** Zone of Flow Establishment. 11, 22

Introduction

1.1. Background

Deep sea mining is the extraction of minerals from the deep ocean and has been a topic of interest since the 1960s. At that time no international regulatory regime governing the seabed outside of the economic exclusive zones existed, creating legal uncertainty. This legal uncertainty together with the discovery of new land-based resources at the time and the subsequent economic uncertainty led to a decline in interest [30]. The last years a renewed interest into deep sea mining can be observed. This interest is created through the rising demand for minerals and metals together with the depletion of land-based resources [31]. No commercial scale deep sea mining has taken place yet, but exploration contracts have been awarded to companies. Many metal-rich deposits can be found in the deep ocean, which can be divided into three types [30]:

- Cobalt-rich ferromanganese crusts
- Seafloor massive sulphides (SMS)
- Poly-metallic or manganese nodules

Cobalt-rich ferromanganese crusts occur on seamounts and rock outcrops in all oceans, but the largest deposit is located in the western Pacific Ocean. SMS deposits are formed at hydrothermal vents along ocean plate boundaries. Poly-metallic nodules can be found on the seafloor on abyssal plains at water depths of 4000 to 6500 m. The largest amounts of nodules can be found in the Pacific and Indian Oceans. A map of the locations where the metal-rich deposits are present is shown in Figure 1.1. This research will focus on the problem of sediment plume generation when collecting poly-metallic nodules, therefore the focus from now on will be on poly-metallic nodules.

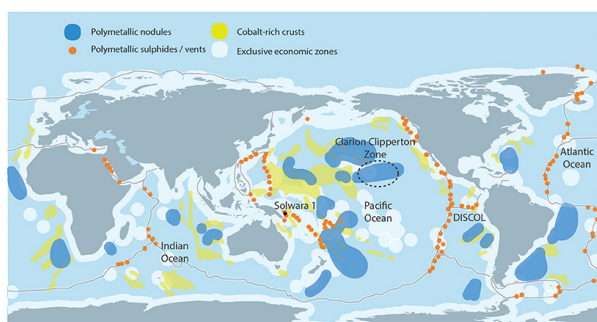


Figure 1.1: World map showing the locations where poly-metallic nodules (blue), poly-metallic sulphides/vents (orange) and cobalt-rich crusts (yellow) can be found [31].



Figure 1.2: Outside and slice through of a manganese nodule [38].

Manganese nodules are located on the seabed or half-buried in it. They are formed in two ways:

- Hydrogenetically, which means that the minerals forming the nodule precipitate from the ambient seawater
- Diagenetically, which means that the minerals precipitate from sediment pore water

The precipitation starts with a small piece of hard substrate, like a piece of shell, forming the nucleus around which the nodule slowly grows its layers. This growth is extremely slow, with growth rates of about 1 to 10 mm per million years for hydrogenetic nodules and several hundred mm per million years for diagenetic nodules. But most nodules are formed by a combination of both processes and grow at intermediate rates. Manganese nodules can become 20 cm in size [14], however the majority are around 5 to 10 cm and are potato-shaped (see Figure 1.2). Poly-metallic nodules mainly contain manganese and iron. However, the greatest economic interest comes from the nickel, copper, cobalt and manganese resources they contain. Also traces of molybdenum, rare-earth elements and lithium can be recovered as a by-product, which are of great importance for technology applications. Manganese nodules are usually the most common type of hard substrate in the areas where they occur, covering about 75% of the seafloor [35].

The concept for collecting manganese nodules comprises a or multiple Seafloor Mining Tool(s) (SMT) picking up the manganese nodules, a Vertical Transport System (VTS) and a production support vessel with possibly an ore carrier (see Figure 1.3). The SMT is self-propelled and uses two tracks to move forward while collecting the nodules. Apart from picking up the nodules a layer of sediment of 5 to 15 cm is collected [11]. This sediment is separated from the nodules by a separation system located in the SMT and discharged through a diffuser at the back, shown as the SMT discharge in Figure 1.3. The reason for this separation is twofold, this minimizes the mass transport and avoids the accumulation of large amounts of sediment in the VTS [19]. The SMT is connected to a flexible hose, through which the separated nodules are transported to the collection base station. The collection base station is in turn connected with the VTS, which transports the nodules to the production support vessel. Once the nodules reach the production support vessel they are separated from the water and remaining sediment. The waste stream, called sediment, waste and other effluents (SWOE), is discharged in the water column, preferably close to the seabed. The nodules will be transported to land and further processed to extract the various resources.

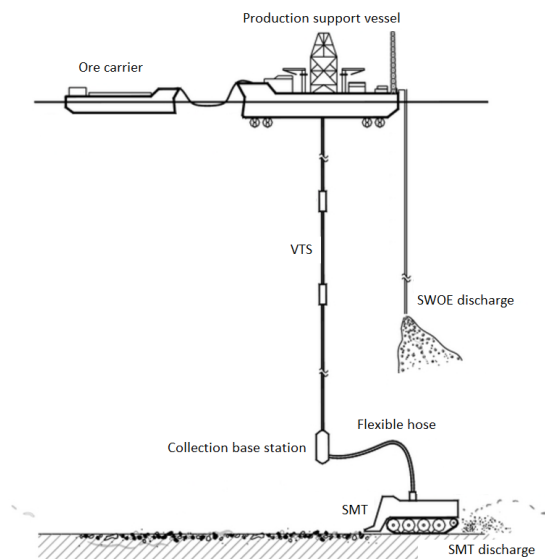


Figure 1.3: A deep sea mining system overview for mining manganese nodules (adapted from [15])

1.2. Problem statement

Not only the nodules are collected but also sediment, about 90% of the sediment is separated and then discharged through a horizontal diffuser at the rear of the SMT [23]. The discharge of sediment will create a sediment plume that needs to be limited for three reasons:

1. Environment
2. Economic
3. Legal

Spreading of the plume over a larger area than the mining area will create a larger environmentally impacted area in which the entire ecosystem is affected. Plumes will spread in areas where natural sedimentation is very low, deposition rates are around one to two mm per thousand years. In contrast, sedimentation caused by plumes will have deposition rates orders of magnitude larger. Increased sedimentation will have a large impact on surface deposit feeding fauna, causing changes in sediment characteristics and clogging of pores of suspension feeding organisms [13]. Moreover, the benthic fauna can be buried through settling of the sediment plume [11]. An increase of 1 cm in sedimentation already shows a reduction in the abundance of biological communities of 21-48% for megafauna, up to 63% for macrofauna and 23% for meiofauna [43]. It has been shown that some species can recover from a disturbance in a couple of years. However, diversity and community composition usually do not recover quickly [30] and few faunal groups have shown to return to the baseline conditions after twenty years [20].

For economic reasons spreading of the plume sideways makes the process of collecting nodules inefficient. The still to be collected nodules are buried under discharged sediment which has to be collected, separated and discharged again. Moreover, this possibly reduces the pick-up efficiency of the manganese nodules, thereby lowering the production.

Legal issues will arise when the discharged sediment plume spreads to other exploration areas owned by other parties or to environmentally protected areas.

1.3. Research questions

Minimizing the discharged sediment plume is of importance for the whole operation. This leads to the following main question:

'Can the spreading of the sediment plume, created by a horizontal discharge diffuser, be reduced by the choice of diffuser height above the seafloor?'

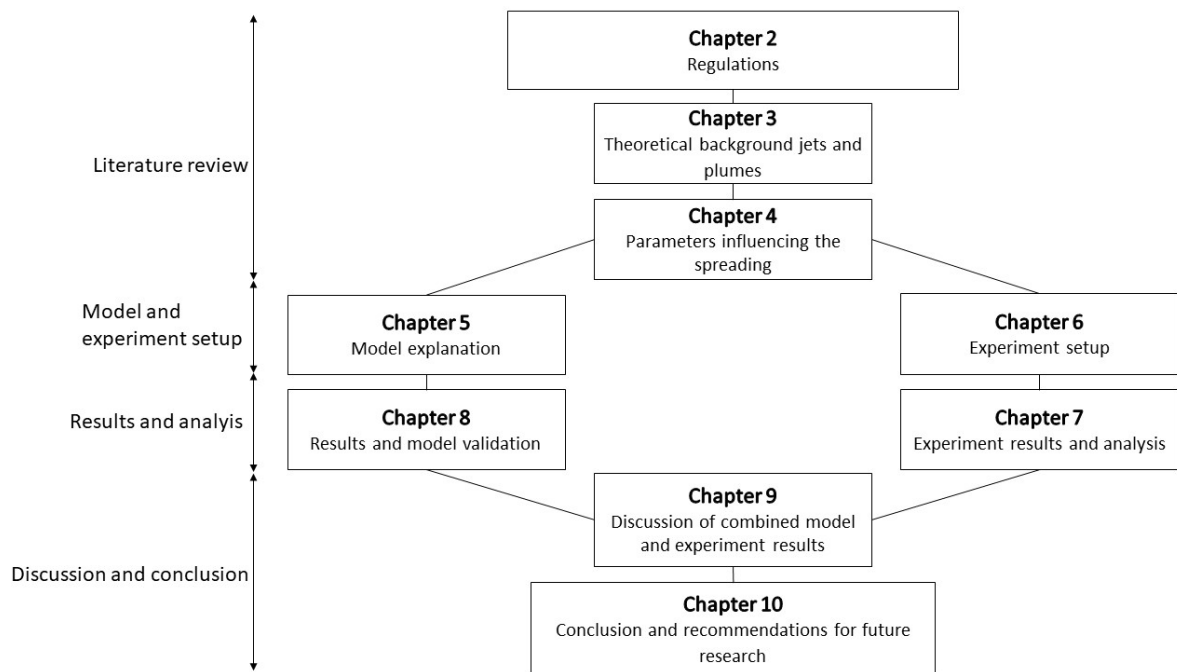
And the following sub-questions:

1. What regulations are already in place to reduce the environmental impact of the deep sea mining sediment plume on the local flora and fauna?
2. How does a plume develop and spread?
3. What parameters have an influence on the spreading of the horizontal discharge plume?
4. What is the influence of the diffuser height on the spreading of the buoyant jet?

1.4. Research methodology

The main question will be answered through literature research, an analytical model and small-scale experiments. The literature research will answer the first three sub-questions and is necessary to gather knowledge about existing regulations, the physics behind plumes and the parameters that have an influence on plume spreading. With the gathered background knowledge, a numerical model is made, based on the JETLAG model by Lee and Chu [25]. The model uses a Lagrangian approach which follows the plume while it travels through space and time. It predicts the 2D trajectory of the plume, calculating the velocity and concentration at each time step. In order to validate the model and gain insight into the behaviour of the plume, small-scale experiments are done. The experiments are done at the laboratory of Dredging Engineering at Delft University of Technology. The small-scale diffuser used during the experiments will be tested at three heights and two mixture velocities. During the experiments the velocity and concentration of the plume are measured and visualization experiments are done to show the spreading of the plume.

1.5. Thesis outline



2

Environmental impact

This chapter deals with the first sub-question: What regulations are already in place to reduce the environmental impact of the deep sea mining sediment plume on the local flora and fauna? First, the cause of the sediment plume is explained. Second, the environmental impact of the sediment plume and last the existing regulations.

2.1. Deep sea mining sediment plume

At the exploration area where the nodules will be collected the surface layer of sediment consists for about 85% of water [29]. The top layer of the seabed of the exploration area mainly consists of clay and silt, with particle sizes less than 90 micron [23]. These particles can reach a settling velocity of about 0.2 cm/s when aggregated, however, the finest fraction will not aggregate and will stay in suspension [11]. Due to the low settling velocities of the particles, the particles can stay in suspension for days and spread over distances of 3.5 to 8 km with a cut-off value for the concentration of 10 mg/L [11]. Note that these values are the result of numerical model simulations and are dependent on the local current conditions and initial concentration (in this case 500 mg/L).

The deep sea mining sediment plume is caused by multiple parts of the process:

- Horizontal sediment discharge of the SMT
- Movement of the SMT
- Vertical discharge of Sediment, Waste, and Other Effluents from the vessel

The focus of this research is on the plume created by the horizontal sediment discharge of the SMT, therefore the other causes for plumes will not be discussed. However, note that the movement of the SMT and the plume created by this will have an impact on the horizontal sediment discharge plume and will be briefly discussed in chapter 4.

2.2. Discharge plume impact

There are a number of impacts resulting from the horizontal discharge plume. In short they are:

- Burial of organisms [11, 31]
- Interference with surface-deposit feeding and suspension feeding organisms [11, 31]
- Alteration of the makeup of the seabed [31]
- The release and deposition of potentially toxic or oxygen-consuming substances [11, 31]
- Alteration of the nutrient dispersal pattern [11]

Burial of organisms

Large quantities of sediment will be redeposited by the sediment plume, thereby burying the organisms living on the seafloor.

Interference with organisms

With interference it is meant that the feeding mechanisms, like pores, through which these organisms feed could become clogged due to the high rates of suspended particles.

Seabed makeup alteration

Alterations of the makeup of the seabed are caused by the different deposition rates inside the plume. Close to the source the large particles with high settling velocities will settle first. Whereas the fine particles with low settling velocities will settle further away from the source or even stay in suspension. The alteration of the seabed makeup might have an influence on the recovery of the fauna [11].

Potentially toxic or oxygen-consuming substances

The release and deposition of potentially toxic substances can lead to bioaccumulation of contaminants. The toxic metals are released from the potentially metal-rich pore waters when the SMT collects the nodules. Also, toxic metals can be present in the sediment plume as suspended particulate material. However, it is difficult to assess the occurrence and impact since no large scale mining operation have taken place yet and the knowledge of the abyssal marine organisms is still limited. Research by MIDAS has shown that the effect of long term exposure to toxic substances may vary widely between organisms [30]. The release of oxygen-consuming substances can lead to oxygen depletion [11].

Alteration of the nutrient dispersal pattern

The redeposited sediment will have a very low average organic carbon content and the grain-size distribution will be altered. This leads to a change in organic matter remineralisation processes. The phytoplankton and detritus that naturally arrive at the seafloor will aggregate during plume dispersion and thereby alter the dispersal pattern of the nutrients. All faunal classes from micro-organisms to the megafauna will be affected by this [11].

To investigate the long term environmental impact of deep sea mining on the fauna multiple surveys over a period of up to 26 years were done at seven sites in the Pacific. These surveys specifically assessed the recovery of the fauna. Almost all of them show some recovery in faunal density and diversity for meiofauna and mobile megafauna. However, few faunal groups return to the baseline conditions after twenty years [20]. A high variability was observed between and within ecosystems, taxa and size classes. The densities and diversities for some taxa can recover to predisturbance conditions but the community composition cannot, even after decades. This may be caused by the removal of the hard substrate, the nodules, which are essential for the survival of some organisms [30].

Many researchers are working on understanding the complexity of the deep sea ecosystem and the impacts of disturbances caused by deep sea mining. However, the exact environmental impact of deep sea mining in general and the discharge plume in specific is not clear yet.

2.3. Regulation

The Clarion Clipperton Zone and other manganese nodule rich areas are mainly located outside the national jurisdiction of countries. This means that no regulations exist for these areas. To ensure that mankind as a whole will benefit from these resources the International Seabed Authority (ISA) was established in 1994. It is an autonomous organisation and currently it has 168 members, all of them are party to the United Nations Convention on the Law of the Sea (UNCLOS). The ISA has established a "Mining Code", which is a set of rules, regulations and procedures to regulate prospecting, exploration and exploitation of marine minerals in the international seabed area. With the international seabed area the seabed and subsoil beyond the limits of national jurisdiction is meant. The mining code is not complete yet, but recommendations and regulations as part of the mining code are already adopted [5].

Prior to operation a contractor needs to deliver a proposed mining plan together with an environmental management plan. Included in the environmental management plan a contractor has to point out the chosen locations for the impact and preservation reference zones. These zones are used as a reference for the environmental disturbances due to mining. Furthermore, contractors need to include their plans for maximizing the recovery of the mined area in their environmental management plan. During operation contractors are obliged to provide environmental data to the ISA which will be used to create a database to broaden the knowledge of the environment. Besides this, contractors are required to minimize potential impacts on the reference zones [3], in their mining code they state the following:

"The Contractor shall take necessary measures to prevent, reduce and control pollution and other hazards to the marine environment arising from its activities in the Area as far as reasonably possible applying a precautionary approach and best environmental practices." [4]

Apart from the regulations for the contractors, the ISA has made an environmental management plan for the Clarion Clipperton Zone (CCZ) in which it explains the implementation of protected environmental areas as one of the measures to protect the environment of the CCZ. The ISA states that the protected environmental areas should not be directly affected by physical activity or indirectly by mining effects such as plumes. The core area of each environmental area should be at least 200km in length and width, this was determined by the ISA by considering environmental data, faunal distribution, faunal dispersal capabilities and distances, and ecological proxy variables. This area is said to be large enough to maintain minimum viable population sizes for species and to capture the full range of habitat variability and biodiversity within a sub region. The core area will be surrounded by a buffer zone of 100km to ensure that it is not affected by mining plumes from nearby exploration areas. Thus, the total area of an environmental area will be at least 400x400km. In total there are nine of these protected environmental areas which are evenly distributed over the CCZ [3].

To conclude, based on these regulations it is clear that the ISA has the aim of minimizing the environmental impact of deep sea mining. However, the precise measures of what will be rendered harmful and what not are determined according internationally recognized standards and practices. These do not include clear boundaries as to what is harmful and what not. Currently there is an ongoing discussion amongst scientist, specialists in marine law and interested parties about how to define the measurement or threshold of harmful effects and what will be considered "acceptable harm" to the deep sea ecosystem from seabed mining [31]. The intention for protecting the environment is there, but in practice it will be difficult to assess whether the impact is truly prevented, reduced and controlled as far as reasonably possible.

3

Jets and Plumes

This chapter explains the theory of jets and plumes to be able to answer the second sub-question: how does a plume develop and spread? First the turbulent buoyant jet is explained by its classification and flow regions. After which the behaviour of the turbulent buoyant jet is explained by describing the concept of turbulent entrainment, terminology, velocity and concentration profiles and Froude number. Then two special cases of a jet are discussed, the sediment-laden jet and the submerged offset jet. Lastly the design principles of a diffuser are explained together with the influence of the diffuser design on the flow.

3.1. What are jets and plumes?

Jets and plumes are turbulent flows produced by momentum and buoyancy sources. Both appear to be the same, but the turbulent motions are caused by different mechanisms. This will be further explained in this section, starting with the classification of jets and plumes, after which the different flow regions of a turbulent buoyant jet are explained.

3.1.1. Classification

A distinction between jets and plumes can be made based on the way the fluid is set in motion. In the case of a jet, the turbulent flow is generated by a continuous source of momentum, whereas for plumes the turbulent flow is produced by a continuous source of buoyancy. The classification of jets and plumes can be seen in Table 3.1. The case of the discharge of a sediment-water mixture from the SMT can be classified as a buoyant jet. Buoyant jets occur when a fluid is discharged with an excess of or deficit in momentum and/or buoyancy through a diffuser into a fluid [9]. The buoyant jet will develop into a plume when the initial source of momentum is dissipated and the buoyancy source remains. Another distinction can be made between a positively buoyant and negatively buoyant effluent. Positively buoyant means that the density of the effluent is smaller than the density of the ambient fluid. Negatively buoyant is the opposite, the effluent density is larger than the ambient fluid density. The buoyant jet created by the SMT is negative, the higher density is caused by the suspended particles.

Table 3.1: Flow classification based on source type and source duration [25]

Source	Source duration	
	Continuous	Instantaneous
Momentum	Jet	Puff
Buoyancy	Plume	Thermal
Momentum and Buoyancy	Buoyant Jet	Buoyant Puff

3.1.2. Flow regions

Slurry, the mixture of sediment and water, will be discharged through the diffuser, after which it develops in three jet regions: near-field, intermediate field and far-field. The near-field region is the region closest to the

source. In this region the velocity and concentration profiles of the buoyant jet over the distance have the same shape and jet entrainment is present, jet entrainment is explained in Section 3.2.1. The intermediate region starts when the jet encounters a boundary (sidewalls, free surface, or seafloor) or is arrested by stratification, for example a water-air boundary. This causes the buoyant-jet to spread rapidly and the boundary layer assumption that is critical to turbulent jet analysis to become invalid. The flow is no longer classified as a buoyant-jet. After the spreading region the discharged buoyant jet enters the far-field region. The behaviour in this region will be dominated by ambient currents, turbulent diffusion and large, basin-scale motions. Figure 3.1 shows the flow regions and their characteristic length and time scale. The near field mixing determines the amount and distribution of suspended sediment available in the far-field, models of the near-field behaviour are thus very important for the accuracy of the far-field model [9].

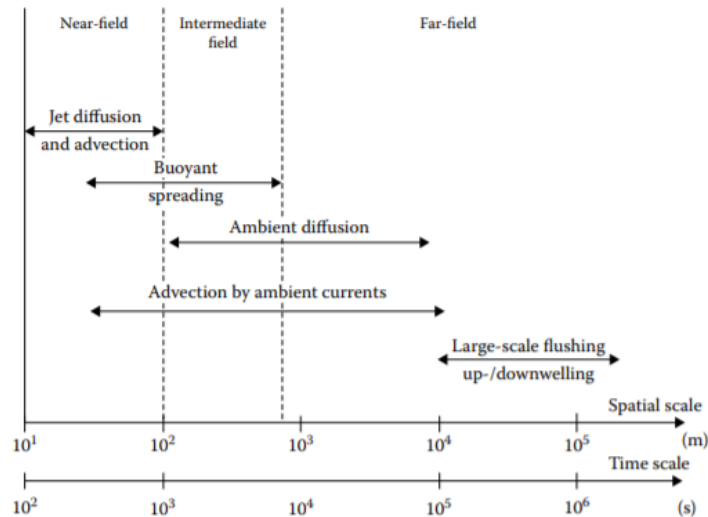


Figure 3.1: Flow regions and the characteristic length and time scales of these regions [9]

3.2. Behaviour

The behaviour of a turbulent buoyant jet is explained by describing the concept of turbulent entrainment. Furthermore the terminology of jets and plumes is explained together with the description of the velocity and concentration profiles. Lastly the influence of the densimetric Froude number on the behaviour of the turbulent buoyant jet will be explained.

3.2.1. Turbulent entrainment

In the turbulent flow of the near-field regime jet entrainment occurs, meaning that at the boundary of the jet ambient fluid is mixed with the discharged fluid, see Figure 3.2. The mixing is caused by eddies. An eddy is the swirling of fluid and the reverse current created by this. The dominant eddies are the larger swirls which cause mass transfer between the centre region of the jet and the boundary of the jet. The small eddies, the smaller swirls of fluid, smoothen the sharp concentration gradients created by the dominant eddies. The velocity with which the eddies cause the entrainment of ambient fluid is called the entrainment velocity v_e . The entrainment velocity is given by the local jet centerline velocity times an entrainment coefficient, α [32].

The turbulent zone or boundary layer in which fluid is entrained by the turbulent eddies, increases with increasing distance from the source. At the same time the concentration of the discharged flow decreases with increasing distance from the source. This decrease is caused by the dilution of the discharged flow by the entrained ambient fluid. At some point the discharged flow and ambient fluid are completely mixed causing the buoyancy in the plume to approach ambient values [25].

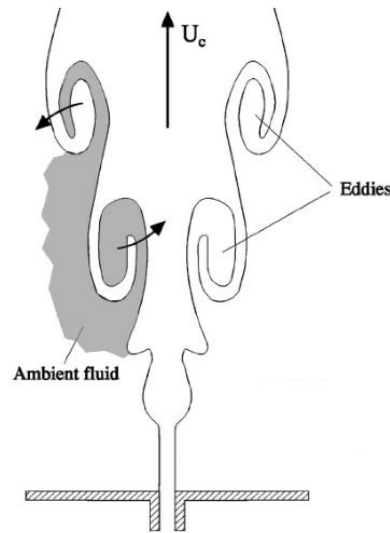


Figure 3.2: Schematic drawing of the turbulent entrainment of ambient fluid by eddies [21]

3.2.2. Terminology

Directly after leaving the diffuser exit during the experiment the discharged flow can be seen as a turbulent jet, since the initial velocity is dominant over the buoyancy. The development of the discharged turbulent jet flow can be divided into two zones: the Zone of Flow Establishment (ZFE) and the Zone of Established Flow (ZEF) [1], as shown in Figure 3.3. Inside the ZFE the mixing layer associated with turbulent entrainment is located at the edge of the jet. There exists a so called potential core in which the fluid can be considered irrotational. This potential core has a length of about $6D$, where D is the diameter of the diffuser. In the case of a rectangular diffuser, D is the height of the diffuser. The time-averaged velocity and concentration in the potential core are constant and can be given by:

$$u(x, y) = u_0 \quad (3.1)$$

$$c(x, y) = c_0 \quad (3.2)$$

Where u_0 and c_0 are the initial velocity and initial concentration, respectively. Furthermore, x is the distance from the source and y is the lateral distance from the centerline. The potential core is the region indicated by the dashed line in Figure 3.3 and has a width of $2r$.

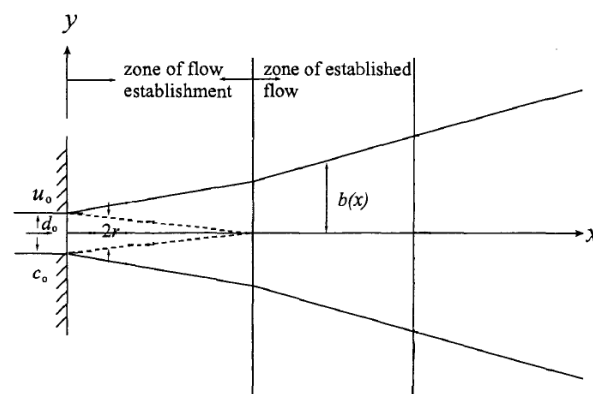


Figure 3.3: Schematic overview of the development of a jet, with u_0 , c_0 and d_0 respectively the initial velocity, concentration and slot height, $2r$ the width of the potential core and $b(x)$ the plume half width [25]

In the ZEF, $x > 6D$, the mixing of the discharged fluid with the ambient fluid is up to the centerline of the discharged flow. The velocity and concentration are self-similar, meaning that the profiles at different x look

similar in shape. These profiles can be approximated by Gaussian distributions [25]. An example of a Gaussian distribution can be seen in Figure 3.4.

The width of the mixing layer is given by the function $b(x)$ and increases linearly with the distance from the source, in equation:

$$b(x) = \beta x \quad (3.3)$$

Where β is a constant called the spreading rate. The width of the velocity profile is smaller than the width of the concentration profile. The difference is a factor λ , which is the ratio between the concentration and the velocity width. This difference is caused by the difference in diffusion of mass and the diffusion of momentum.

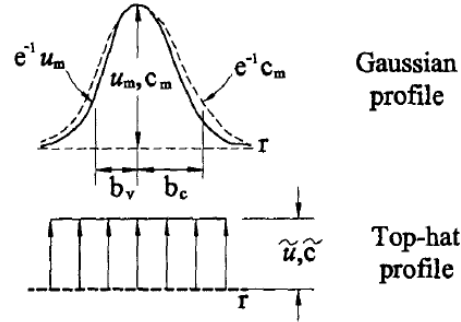


Figure 3.4: Example of a Gaussian and top-hat profile [25]

3.2.3. Velocity and Concentration Profiles

There are two types of profiles that can be used to describe the velocity and concentration profiles of a turbulent buoyant jet: the top-hat profile and the Gaussian profile. A top-hat profile means that the average velocity and concentration are assumed over the width of the mixing layer, an example of the top-hat profile can be seen in Figure 3.4. The choice between the two depends on the type of analytical framework used to describe the near-field behaviour of a turbulent buoyant jet: Eulerian or Lagrangian. The Eulerian approach describes the plume in terms of the centerline variables and the velocity and concentration profiles are defined by the Gaussian profile. Whereas the top-hat profile is convenient for Lagrangian approach to describe the velocity and concentration profiles. This is because in the Lagrangian approach the average properties of the buoyant jet are calculated, therefore the top-hat profile is immediately determined. The Lagrangian approach is simple and easy to implement because the velocity and concentration profiles do not have to be specified. This is useful because these profiles are not always known for more complex turbulent flows. The model described in Chapter 5 uses the Lagrangian approach since this approach has a lower computational expense.

The definition of the width of the mixing layer, b , depends on the choice between Gaussian and top-hat profile. The width of the velocity profile when using a top-hat profile is defined as the location where the velocity is equal to the average velocity over the cross-section. The width of the concentration profile when using a top-hat profile is defined as the location where the concentration is 25% of the maximum concentration. The top-hat velocity and concentration profiles are related to the Gaussian equivalents by [25]:

$$u = \frac{u_m}{\sqrt{2}} \quad (3.4)$$

$$b = \sqrt{\pi/2} b_g \quad (3.5)$$

Where u is the average velocity in the top-hat velocity profile, u_m is the maximum velocity in the Gaussian velocity profile, b is the half-width of the mixing layer for the top-hat profile, b_g is the mixing layer half-width for the Gaussian profile.

3.2.4. Densimetric Froude number

The near-field plume is characterized by the densimetric Froude number. The densimetric Froude number at the source can be determined by the following equation:

$$Fr_0 = \frac{U_0}{\sqrt{g'_0 D}} \quad (3.6)$$

Where D is the size of the source and g'_0 is the reduced gravity determined by:

$$g'_0 = g \frac{|\rho_a - \rho_0|}{\rho_a} \quad (3.7)$$

Where g is the gravitational constant, ρ_a is the ambient fluid density and ρ_0 is the density of the effluent. The densimetric Froude number can be interpreted as a ratio of energy dissipation to production [25]. For a simple jet $Fr_0 \rightarrow \infty$, for a pure plume $Fr_0 \rightarrow 0$ and for a buoyant jet $0 < Fr_0 < \infty$ [7]. $Fr_0 \rightarrow \infty$ means that $\rho_a = \rho_0$. If the densimetric Froude number is smaller than one the flow is termed subcritical and if the densimetric Froude number is larger than one it is termed supercritical. In subcritical flows the entrainment from the ambient fluid is negligible. This is because the maximum velocity is encountered near the boundary of the flow, preventing entrainment of the ambient fluid. Whereas in supercritical the maximum velocity is encountered at the centre of the flow and therefore high entrainment at the boundary is present [39].

3.3. Sediment-laden jet

Apart from the characterisation as a negatively turbulent buoyant jet in Section 3.1.1, the horizontal discharge plume can also be thought about as a particle-laden jet or, more specific, a sediment-laden jet. A particle-laden jet is a two-phase flow, in this case a mixture of water and sediment hence the name sediment-laden jet, that is given an initial momentum flux. A particle-laden jet can be characterised by a sedimentation length scale l_m defined by the jet momentum flux and particle settling velocity [27].

$$l_m = \frac{M_0^{1/2}}{\omega_s} \quad (3.8)$$

Where M_0 is the momentum flux and ω_s is the particle settling velocity. For spherical particles the settling velocity can be determined from a standard settling velocity formula [27].

$$\omega_s = \sqrt{(4/3)C_D(s-1)gd_{50}} \quad (3.9)$$

Where s is the specific gravity of the particle given by ρ_s/ρ with ρ_s the sediment density and ρ the fluid density; d_{50} is the particle diameter. The drag coefficient is given by $C_D = 24[1 + (Re_d^{2/3}/6)]/Re_d$, Re_d is the particle Reynolds number given by $Re_d = \omega_s d_{50}/\nu$ with ν the kinematic viscosity.

The length scale l_m gives the relative importance of jet momentum-induced velocity to settling velocity and is a measure of the distance from the source where particles start to fall out from the jet. A larger value of l_m indicates that the sediment will settle further away from the source. Based on l_m three regions with different behaviour of the sediment inside the sediment-laden jet can be observed. For $x < 0.5l_m$ the upper half of the jet behaves like a pure jet. For $0.5l_m < x < l_m$ the particles start to fallout of the jet and for $x \geq l_m$ the suspended particles separate significantly from the jet. The decay of the maximum particle concentration c_m/c_0 can also be expressed by l_m . It can be observed that for $x < 0.5l_m$ the maximum particle concentration is inside the jet region and the decay of c_m behaves like a free jet [10, 25, 27]. For $x \geq l_m$, c_m is significantly less than that given by jet theory. Furthermore Liu and Lam (2013) observed that for initial sediment concentration with a volume fraction below 0.1% the characteristics of the jet flow did not change significantly. However, for a jet with higher initial sediment concentrations, like the case of the SMT horizontal sediment discharge, the presence of the sediment bends the trajectory of the jet downward. The degree of this bending is smaller than that of an equivalent one-phase negatively buoyant jet with effluent of the same density as the fluid-particle discharge combined density [28].

3.4. Submerged offset jet

A submerged offset jet or submerged wall jet is formed when a fluid is discharged from an elevated opening above a solid boundary that is parallel to the axis of the jet. Figure 3.5 shows a schematic overview of the flow zones encountered in submerged offset jets. Once the fluid is discharged from the opening it is deflected towards the solid boundary due to the reduced pressure at the bottom of the jet, this is called the Coanda effect [37]. This is the recirculation zone in Figure 3.5. The flow velocity in the jet reduces as the jet approaches the boundary, as a consequence, the pressure inside the jet increases. In the impingement region the flow reattaches to the boundary and the jet starts to behave as an impinging jet. This causes the pressure to become greater than the hydrostatic pressure, creating a pressure gradient that accelerates the flow. At the end of the impingement region the acceleration stops and a turbulent wall jet condition is established. Due to turbulent diffusion and the presence of the solid boundary, the thickness of the wall jet region increases [22].

The submerged offset jet seems quite similar to the sediment discharge of the SMT. However there are some differences that may cause different behaviour. The experiments done by Kishore (2016) showing the behaviour of a submerged offset jet are done in a flume that was 0.6m wide, 0.71m deep, and 12m long, and a slot width equal to the flume width. Therefore these experiments show the 2D behaviour of an offset jet, however the buoyant jet discharged by the SMT will spread in three directions. Eliminating one direction might influence the measured velocities and the observed behaviour of the jet. Moreover the initial velocity of the experiments is between 1.1 and 1.8 m/s, which is about five times larger than discharge velocities expected for the SMT. Since the occurrence of the Coanda effect is related to the initial jet velocity, it cannot be safely said that this will also occur at these lower initial jet velocities. Also, these experiments are done with a single phase fluid, meaning no particles are present in the discharged fluid. This will not be the case in deep sea mining, where particles will be present in the fluid and the presence of these particles will influence the behaviour of the jet (Section 3.3).

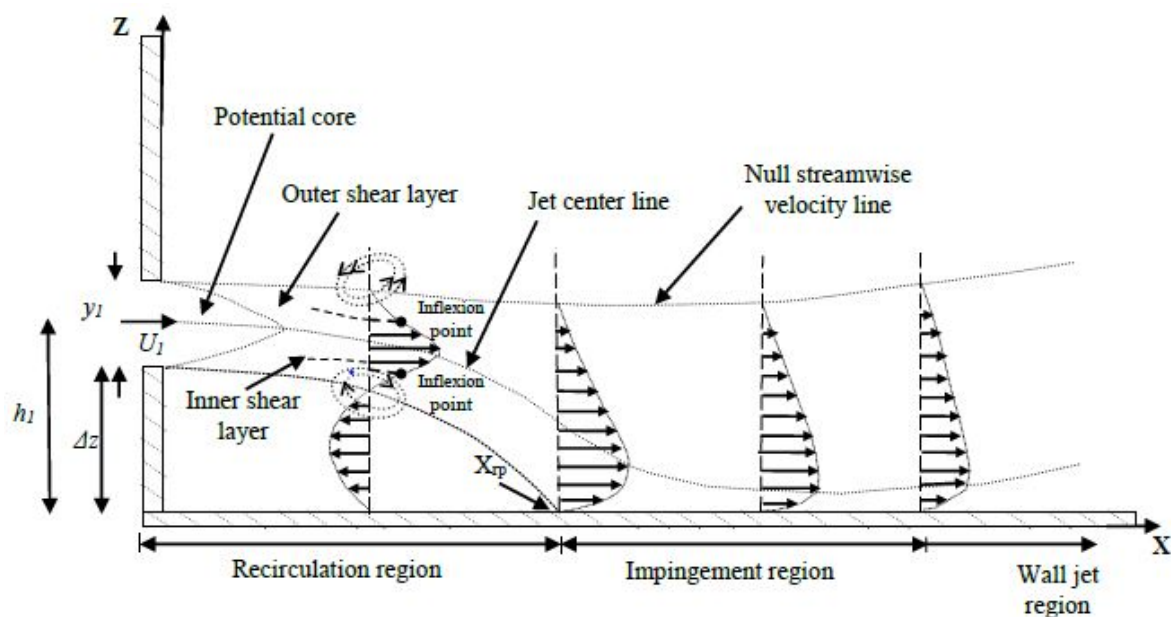


Figure 3.5: Schematic overview of the flow zones in a submerged offset jet [22]

3.5. Diffuser

A diffuser will be part of the SMT disposing of the separated water sediment mixture. The purpose of the diffuser is to lower the flow velocity of the discharge. This is done by increasing the discharge opening of the diffuser, as a result the pressure is also increased. An example of a flat-walled diffuser as possibly used for the SMT is given in Figure 3.6.

When a fluid flows through a duct a viscous boundary layer is present at the wall of the duct. This viscous

boundary layer is due to friction between the fluid and the wall. Due to the pressure increase in the widening cross-section of the diffuser an adverse gradient is created causing a point of inflection in the flow profile, see Figure 3.8. The adverse gradient is influenced by the angle of the diffuser and the ratio of length over width. A large angle over a short length, meaning a fast expansion of the area, will cause a large pressure increase. Resulting in a large adverse gradient and a high point of inflection when looking at the flow profiles in Figure 3.8. Once a critical adverse gradient is reached, the flow alongside the wall separates. Increasing the adverse gradient even further will result in a backflow at the wall, in diffuser literature this condition is called diffuser stall [42].

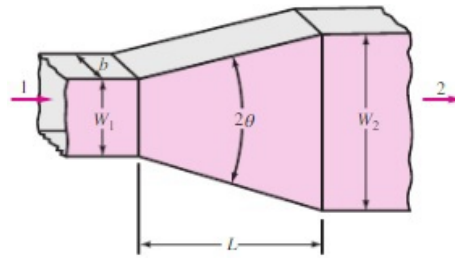


Figure 3.6: Geometry of a flat-walled diffuser, where b is the width, W is the height, L is the length and θ is the diffuser angle [42]

The flow patterns of a diffuser can be divided into four regions as shown in the stability map in Figure 3.7. The first one is the no stall region, in which there is steady flow, no separation and moderately good performance. The second region, between line a-a and b-b, is the transitory stall region with strongly unsteady flow and the highest performance coefficient C_p , thus best performance. The third region, between line b-b and c-c, is the bistable steady stall region in which for a flat-walled diffuser the flow will stick to one of the diverging walls. The flow can change from one wall to the other and performance in this region is poor. Lastly, the fourth region above line c-c, is the jet flow region where wall separation is so large that the main flow will ignore both diverging walls in a flat-walled diffuser and simply pass through at nearly constant area. The performance is extremely poor in this region. If the diffuser is well designed, no flow separation will be present and the outflow pattern will be uniform with a low exit velocity [42].

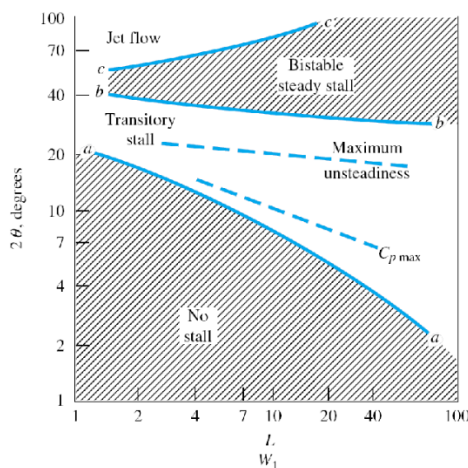


Figure 3.7: Stability map for flat-walled diffusers [42]

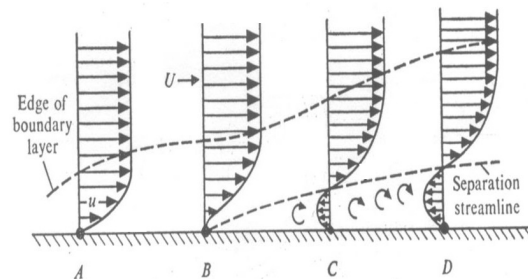


Figure 3.8: Steps in flow separation; PI is point of inflection: (A) zero gradient: no separation, PI at the wall, (B) weak adverse gradient: no separation, PI in the flow (C) critical adverse gradient: separation (D) excessive adverse gradient: separation and backflow at the wall [16]

3.6. Conclusion

Jets and plumes are turbulent flows produced by momentum and buoyancy sources. The turbulent flow of a jet is generated by a continuous source of momentum and the turbulent flow of a plume is generated by a continuous source of buoyancy. The horizontal sediment discharge from the SMT can be classified as a combination of the two, named a buoyant jet. In this case the buoyant jet is negatively buoyant, meaning that the discharged effluent has a larger density than the ambient fluid. After leaving the diffuser outlet of the SMT, turbulent entrainment occurs at the boundary of the buoyant jet. Ambient fluid is mixed with the discharged mixture, thereby diluting the buoyant jet and increasing the width. The boundary layer in which entrainment occurs increases with increasing distance from the source. Entrainment occurs until the discharged mixture and the ambient fluid are completely mixed. The horizontal sediment discharge from the SMT can also be seen as a sediment-laden jet, characterised by a sedimentation length scale l_m . This length scale gives the relative importance of the jet momentum-induced velocity to the settling velocity and is a measure of the distance from the source where particles start to fall out from the jet. Another way of looking at the horizontal sediment discharge from the SMT is to see it as a submerged offset jet. A submerged offset jet is formed when a fluid is discharged from an elevated opening, due to the Coanda effect the jet bends towards the bottom boundary and attaches to it.

4

Influencing parameters

This chapter treats the parameters that influence the spreading of the plume to be able to answer the third sub-question: What parameters have an influence on the spreading of the horizontal discharge plume? A distinction is made between parameters that can be influenced and parameters that cannot be influenced.

4.1. SMT variables

This section explains the variables related to the SMT that can be influenced either during the design phase or during operation. The concentration, discharge velocity and SMT velocity can be adapted during the operation while the diffuser geometry and height are determined during the design phase of the project.

4.1.1. Suspended Sediment Concentration

The initial suspended sediment concentration (SSC) and density of the discharged mixture deviate from the surrounding fluid and are important for the occurrence of density effects [18]. The suspended particles change the local fluid density, causing stratification and buoyancy effects as density currents. The intensity of these effects depends on the density difference between the discharge fluid and the surrounding fluid [17]. The discharge mixture's salinity and temperature, which also deviate from the ambient fluid conditions, create density effects as well. The mixing rate between the discharged mixture and the ambient fluid influences the duration of the buoyancy effects. Mixing causes the density difference to diminish until at some point the ambient and local density are equal. Density currents are characterised by a high sediment concentration within, and a sharp vertical gradient of the sediment concentration at the upper edge. This is the stratification caused by the suspended sediment and limits vertical mixing [34].

The SSC also has an effect on the formation of flocs. Most particles in the plume will have diameters smaller than $60 \mu\text{m}$ [18], when particles are this fine the inter-particle forces become in the order of the inertia and drag forces acting upon them. Due to these cohesive forces between the particles large flocs containing a large number of single grains can be formed. Flocs have different densities, sizes and shapes than single particles. Therefore the settling behaviour of the flocs is very different from that of single particles and settling velocities are higher. Flocculation effects in the plume become significant when concentrations are above 100 mg/l , these high concentrations can be found near the source [18]. Collision mechanisms bring particles together so aggregates can be formed. Collision mechanisms are Brownian motion, turbulent velocity fluctuations and differential settling. Brownian motion is the random motion of suspended particles resulting from the collision with fast-moving molecules in the fluid. Only Brownian motion has a significant influence on the flocculation behaviour of the smallest particles, assuming each collision forms an aggregate. The flocculation of larger particles is mainly influenced by differential settling and high turbulence intensities [19]. High turbulence intensities result in high shear rates, these are induced by the moving SMT and the effect of the momentum flux caused by the discharge of sediment by the diffuser. The shear rate has an effect on the mixing, by increasing the chance for collisions, and entrainment, by increasing the dilution and thereby decreasing the chance for collisions. Gillard (2019) analysed the aggregation under differential settling and turbulent shear. This showed that the sediment concentration in the plume and the shear rate dictate the behaviour of the suspended particles. It was found that increasing the suspended particle concentration or the

shear rate increased the aggregate growth, thereby showing that aggregation dominated over breakup [12].

Large particles suspended in the water column are settling towards the seafloor, thereby collecting finer particles and transporting them downwards, this process is called scavenging. Scavenging of plume particles by aggregates formed by flocculation is a function of particle concentration in the plume and shear rate. Increasing either the particle concentration or the shear rate results in faster scavenging of particles by flocs [12].

4.1.2. Discharge Velocity

The discharge velocity is related to the volume flux and area by:

$$u_0 = Q_0 / A \quad (4.1)$$

Where u_0 is the discharge velocity or initial velocity, Q_0 is the initial volume flux and A is the diffuser exit area. A larger initial velocity means that the initial momentum flux is larger as well. Suspended particles will fall out of the plume when their settling velocity ω_s is higher than the entrainment velocity v_e . The entrainment velocity is proportional to the local jet velocity u , $v_e = \sqrt{2}\alpha u$. A higher local jet velocity results in a higher entrainment velocity. Since it takes longer to dissipate the energy with a higher initial velocity, the entrainment velocity will also be higher for a longer time. This means that the particles will start to settle further away from the source in the case of a larger initial velocity.

The spread angle of the sediment is also related to the initial velocity of the mixture. The spread angle is the lateral extent of the sediment fallout region (see Figure 4.1), and is given by [27]:

$$\psi_c = \sin^{-1}\left(\frac{v_e}{\omega_s}\right) \quad (4.2)$$

Sedimentation will start when ω_s becomes larger than v_e , at this moment spreading of the sediment starts. As can be seen from the spread angle equation the entrainment velocity and particle settling velocity influence the spread angle. A higher entrainment velocity will create a larger spread angle of the plume, thus a narrower sediment fallout region and a decrease in width of the particle bottom deposition.

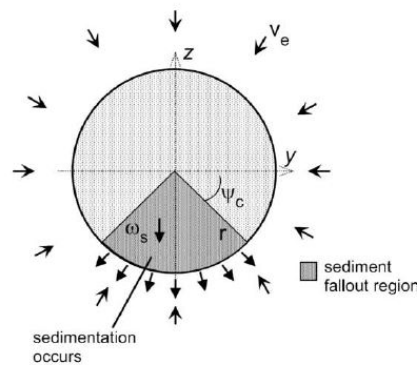


Figure 4.1: Slice through of the buoyant jet, particles will start to drop out if $\omega_s \sin(\psi_c) > v_e$, where ω_s is the settling velocity, ψ_c is the spread angle and v_e the entrainment velocity [27]

4.1.3. Diffuser Geometry

The dimensions of the diffuser and thereby the diffuser cross-sectional area at the exit will influence the spreading of the plume. A larger diameter diffuser means a larger outflow area. The momentum will become lower and thus less energy needs to be dissipated. Therefore a larger diameter diffuser will cause the impingement point to be closer to the source when the other parameters are the same.

The angle of the diffuser with respect to the seabed will influence the behaviour of the discharged mixture once it leaves the diffuser. Experiments done by Papakonstantis [36] showed that for inclined turbulent dense

jets discharged upwards for angles up to 45deg to the horizontal there is an increase in horizontal distance of the impingement point. For larger angles the impingement point decreases with increasing discharge angle up to 80deg. Also, the final terminal height of the jet increases with increasing discharge inclination.

The location of the diffuser on the harvester, especially the height of the diffuser above the seabed, will influence the spreading of the plume. A lower height above the seabed of the diffuser will lower the potential energy in the particles of the plume, which would be beneficial for the settling time. However, it is unknown how much erosion a lower diffuser will result into. Since a buoyant jet discharged close the seafloor has less time to bend, the forward velocity at impingement will be larger. Depending on the magnitude of the forward velocity this might result into erosion. Discharging at a velocity equal to the SMT velocity, a neutral velocity, could be helpful. This would cause the discharged mixture velocity to be completely dependent on the buoyancy flux, resulting in a lower forward velocity. Research into this topic still has to be done.

4.1.4. SMT velocity

The velocity of the SMT moving over the seabed will influence the amount of sediment being swept up by the tracks. Also, the SMT will create a wake which will grow when its velocity is increased. Computational Fluid Dynamic (CFD) simulations show that the velocity of the SMT influences the vertical height of the plume. A lower velocity will result in a larger height of the plume. The sediment flux caused by the SMT will be the highest within the first 2 m above the seabed, where the value of the sediment flux is lower for lower SMT velocities [34].

4.2. Local conditions

This section explains the influence of the local conditions on the spreading of the plume. The local conditions treated in this section are: the current, temperature, salinity, turbidity, bottom topography and sediment.

4.2.1. Current

Deep ocean currents are relatively slow, in the order of a few cm/s, but can create turbulent disturbances due to the typically weak stratification. These turbulent disturbances originate from the bottom boundary and can penetrate a hundred meters or more vertically [2]. Currents will start to have an influence on the plume transport after the dispersion of the plume by eddies in the wake of the SMT and after the subsequent gravity current in the direct vicinity of the source [17]. Through experiments it was found that with a current flow velocity of 3 to 4 cm/s bedload transport of the settled aggregates starts. Bedload transport means that the particles are transported along the bed. It was also found that flow velocities larger than 7 cm/s will possibly resuspend the settled aggregates and create a new plume [12]. In the event of passing ocean eddies, model experiments based on eddy data of a real event showed that the direction of plume spreading is influenced by the passing of the ocean eddies. The plume will be elongated in the direction of the eddy and disperse more rapidly. Model experiments also showed that the direction of mean flows has a large influence on the direction of plume spreading but not on the spreading rate [2].

4.2.2. Temperature, salinity and turbidity profiles

Temperature, salinity and turbidity profiles provide local particle concentrations and density field of the undisturbed seawater. This information is especially important for modelling surface discharges. The surface discharge will be influenced by the thermocline, which is a boundary between two areas with different hydro-dynamical characteristics [18]. In the Bottom Boundary Layer (BBL), the influence of temperature and salinity stratification is assumed to be negligible [19].

4.2.3. Bottom topography

The bottom topography of the Clarion Clipperton Zone is dominated by flats, ridges and troughs [40]. Model experiments done by MIDAS (Managing Impacts of Deep-sea resource exploitation, a multidisciplinary research programme) showed that topographic 'bumps' in the order of 100 m high by a few kilometres wide have several effects on the near bed flows. They enhance vertical mixing downstream as a result of internal hydraulics. Mixing levels downstream of a 'bump' are large enough to disperse material through a 100 m thick bottom layer within a day. They influence the spatial variations of the bottom currents, which will vary at the same spatial scale as the topographic variations [2]. Changing the direction of the bottom currents will influence the spreading of the plume, making it harder to predict its behaviour.

4.2.4. Sediment

The sediment that can be found in the Clarion Clipperton zone has particle sizes ranging from a few microns to a hundred microns in size [11]. It differs per location what the exact particle size distribution is. Large particles settle quicker than fine particles. Thus a plume consisting of mainly large particles will spread less than a plume consisting of fine particles. Settling velocities range from 10^{-3} to 10^{-7} m/s [18]. The settling velocity is the main parameter affecting the plume concentration and resedimentation [19].

Scavenging may have an effect on the fine particles in the diluted plume which have low settling velocities [18]. The influence of scavenging by external particles originating from the upper ocean layers, also called marine snow, is only important in areas with high biological productivity and when they are not dissolved or destroyed before reaching the BBL [19].

4.3. Conclusion

The parameters that influence the spreading of the horizontal discharge plume can be divided into parameters that can be influenced and parameters that cannot be influenced. Parameters that can be influenced are the parameters related to the SMT, these can be influenced either during the design phase or during operation. These are the SSC, discharge velocity (u_0), diffuser geometry and SMT velocity. The density difference between the ambient fluid and the plume influences the intensity of the stratification and buoyancy effects caused by the suspended particles. Moreover, the formation of flocs is influenced by the SSC and shear rate. Increasing the SSC or the shear rate increases the aggregate growth. Increasing the discharge velocity causes particles to settle further away from the source and decreases the width of the bottom deposition. The diffuser outlet area influences the outflow area, and thereby the velocity decrease of the effluent. Moreover, the angle of the diffuser with respect to the seabed causes the impingement range to increase for angles up to 45deg, increasing the angle further will decrease the distance to the impingement range. However, this increases the terminal height of the jet. The SMT velocity causes a sediment flux that is highest within the first 2m above the seabed, where, for lower SMT velocities the sediment flux is lower. Parameters that cannot be influenced are the local conditions. These are the current, temperature, salinity and turbidity profiles, bottom topography and sediment. The local currents have low velocities, however currents caused by the mining operation may cause erosion of the settled particles if they are larger than 7cm/s. The influence of the temperature, salinity and turbidity profiles is important for the surface discharge, but is assumed negligible in the BBL. Topographic 'bumps' in the order of 100m high by a few kilometres wide enhance the vertical mixing downstream, causing dispersal of the particles through a 100m thick bottom layer within a day. The 'bumps' also influence the spatial variations of the bottom currents, this change of directions makes it harder to predict the spreading behaviour of the plume. The sediment found in the Clarion Clipperton zone has very low settling velocity, that range from 10^{-3} to 10^{-7} m/s, causing particles to stay suspended for long times and spread further away from the source.

5

Lagrangian numerical model

This chapter explains the Lagrangian numerical model that was made to extrapolate the results from the small-scale experiments, explained in the next chapter, to the expected dimensions in full scale deep sea mining. The chapter begins with an explanation of the model existing of the description, input and output and adaptations and assumptions. This is followed by the model formulation and model verification with literature.

5.1. Model explanation

This section will give a description of the model, clarify the input and output parameters and explain the adaptations and assumptions.

5.1.1. Description

The model is based on the validated JETLAG model [24, 26] as explained in chapter ten of 'Turbulent Jets and Plumes' by Lee and Chu [25] and was made in MATLAB. The JETLAG model predicts the 3D trajectory of a turbulent buoyant jet, but is adapted to predict the 2D trajectory for this research. The model uses a Lagrangian approach with a moving reference frame, in the case of a buoyant jet, the reference frame follows the motion of the dominant eddies. Instead of solving the Eulerian differential equations of fluid motion and mass transport, the key physical processes expressed by the governing equations are modelled. The jet trajectory is determined based on the division of the trajectory into a sequence of 'plume elements'. The assumption underlying this division is that there is negligible streamwise mixing between the consecutive plume elements. A plume element is a certain material volume with a velocity U followed over a time interval δt , and has a streamwise length of $U\delta t$, as shown in Figure 5.1.

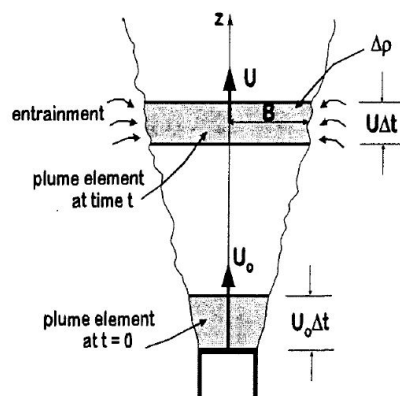


Figure 5.1: Lagrangian formulation of the motion of a plume element through time [25]

The plume elements are described by their location, average velocity, sediment concentration, width and thickness. Since the average properties of the element are calculated with this method, the velocity and con-

centration profiles are given by a top-hat profile over the width of a plume element. The choice of calculating the average properties is justified by the dominant-eddy hypothesis, which can be explained as the entrainment of ambient fluid due to the largest (dominant) eddies which are formed in turbulent shear flow. These dominant eddies are filling up the complete width of the turbulent region and move along with the path of the buoyant jet. Once ambient fluid is entrained by these dominant eddies it stays entrained, thereby causing the mass and volume of a plume element to increase. Because the model determines the average properties in the jet cross section, there is no distinction between the ZFE (the potential core) and ZEF.

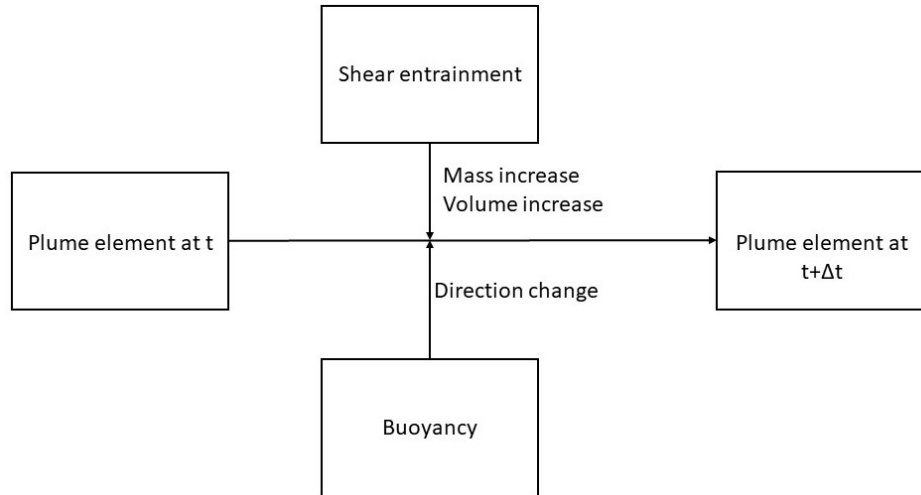


Figure 5.2: Overview of the physical processes determining the plume element at the next time step

The increase in mass and volume is caused by shear entrainment due to the jet discharge. The plume elements change in direction due to buoyancy. An overview of these physical processes that are calculated to determine the plume element at the next time step is given in Figure 5.2. The model gives the average properties of a plume element at each time step while at the same moment the conservation of horizontal and vertical momentum, conservation of mass accounting for entrainment, and conservation of tracer mass is ensured. Each time step the turbulent entrainment of ambient fluid, due to shear entrainment into the plume is calculated. The increase in mass and volume due to shear entrainment is due to the relative velocity between the plume element and the ambient velocity in the direction of the jet axis.

Method of Excess

The method of excess is used to deal with the continuous increase in mass and volume of a plume element due to entrainment. The concentration excess can be defined as the concentration relative to the ambient concentration ($\tilde{c} - c_a$). To determine the mass balance equation for the excess the mixing between the fluid in the elemental volume and the entrained ambient fluid is considered. The mass balance can be seen in Figure 5.3. When fluid is entrained by the dominant eddies of the elemental volume, tracer 'mass' is exchanged between the eddies and their environment. In this formulation the concentration \tilde{c} and c_a are considered as intensive variables, meaning they do not depend on the size and the amount of material of the volume, and are defined as the tracer 'mass' per unit mass of carrying fluid. This results into a tracer 'mass' of $\tilde{c}\tilde{M}$ inside the elemental volume and a tracer 'mass' entering the elemental volume of $c_a\delta\tilde{M}$. After the mixing of the fluid the increased elemental volume will have a mass concentration of $\tilde{c} + \delta\tilde{c}$ and carrying mass $\tilde{M} + \delta\tilde{M}$. In equation this gives the mass-balance

$$\delta[(\tilde{c} - c_a)\tilde{M}] = -\tilde{M}(\delta c_a) \quad (5.1)$$

This equation can give the mass-balance of different properties depending on the choice of considered tracer 'mass' concentration. The tracer 'mass' concentration can both represent scalars, like salinity and heat, or vectors such as linear and angular momentum. The above equation can only be used for properties that are conserved, however in the case of a buoyant jet the momentum of the system may change due to the buoyancy force. Therefore a general form of the equation for the excess is obtained, Equation 5.2, which can be adapted to use for any tracer mass in the flow (e.g. suspended sediment, momentum, buoyancy).

$$\delta[(\bar{c} - c_a)\bar{\rho}\bar{V}] = -\bar{\rho}\bar{V}\delta(c_a) - \kappa\delta t \tag{5.2}$$

Where $\delta[(\bar{c} - c_a)\bar{\rho}\bar{V}]$ is the concentration excess of the tracer mass, $\bar{\rho}\bar{V}$ is the mass of the carrying fluid, \bar{c} is the tracer concentration (tracer mass per unit mass of the eddies), c_a the tracer concentration of the ambient fluid, and κ the 'mass' dissipation rate. The dissipation term, $\kappa\delta t$, resembles for example the buoyancy in the momentum equation. The momentum changes due to the buoyancy force, in this case κ is the buoyancy force. Thus, $\kappa\delta t$ accounts for a positive or negative change to the system.

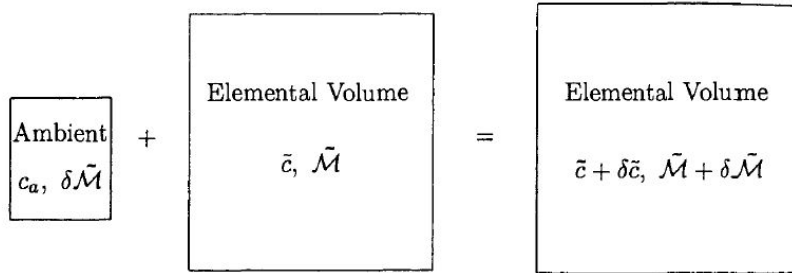


Figure 5.3: Mixing of fluid in an elemental volume carrying mass \bar{M} and concentration \bar{c} with an ambient fluid volume carrying mass $\delta\bar{M}$ and concentration c_a [25]

5.1.2. Input and output

The input and output parameters are shown in the block scheme of Figure 5.4. The diffuser outlet diameter, or hydraulic diameter in the case of a rectangular diffuser exit, is used to determine the initial width of the plume. Moreover, it is used to determine the initial volume, momentum and buoyancy flux. The mixture density is determined by the fluid density, sediment density and the volume concentration of sediment. The difference in mixture density and ambient fluid density determines the magnitude of the buoyancy flux. The initial jet velocity influence the momentum flux, a higher initial velocity means a higher initial momentum flux, thus more energy needs to be dissipated. The initial concentration is used to determine the effluent density and influences the buoyancy flux. With total duration, the duration of the simulation is meant. Since no bottom boundary is present in the current model, the total duration determines the length of the trajectory.

The trajectory and width of the trajectory (b), show the development of the turbulent buoyant jet. The average velocity and concentration are given as a top-hat profile over the width of every plume element. The impingement range is given as the horizontal distance where the horizontal buoyant jet reaches the bottom. Since no bottom boundary is present in the current model, the impingement range is determined by determining the horizontal distance at a chosen vertical distance from the center of the diffuser.

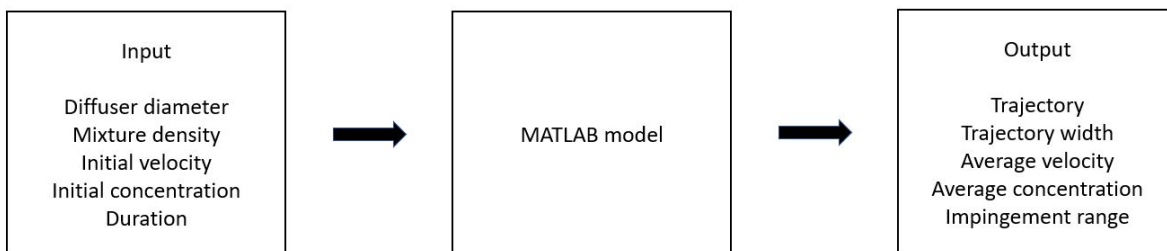


Figure 5.4: Input and output parameters of the MATLAB model

5.1.3. Adaptations and assumptions

Some adaptations to the JETLAG model are made to allow for a simple model that can predict the near field behaviour of the plume. The JETLAG model takes ambient density stratification into account, while

the model used for this research assumes a constant ambient density. Meaning that changes in salinity and temperature are not considered in the model. Furthermore, the JETLAG model is capable of modelling a uniform current influencing the behaviour of the buoyant jet. The model made for this research does not model a current, since this was not considered necessary for model validation and a first full scale prediction of the near field behaviour of the plume.

In addition to the adaptations made to the JETLAG model, simplifications to reality are made. The model assumes a circular exit which results into a turbulent round plume, since this is less time consuming to model. Although the diffuser used in the flume experiments is rectangular it is assumed that the difference between a circular exit and rectangular exit will not severely impact the outcome of the model. This can be assumed because the plume resulting from a slot will become circular in a sufficiently short time. Furthermore, the model source is instantaneous, this implies that the behaviour of the plume element is determined by the conditions at the first time step. In reality, the buoyant jet has a continuous source of effluent meaning that the behaviour of the plume element is not only influenced by the conditions at the first time step but also by the input at later time steps. Moreover, the model does not take the individual sediment particles into account, instead it models the presence of sediment by the increased effluent density it causes. By ignoring the individual particles the model predicts a larger bending and therefore earlier impingement than observed during experiments [28]. Thus ignoring the physical interaction between the fluid phase and the solid particles causes an overestimation of the bending of the buoyant jet.

5.2. Model formulation

The initial location of the plume element is at the diffuser outlet, but for now consider a plume element located at (x_i, z_i) and with a velocity (u_i, w_i) , where i is the step. The number of steps is determined by the total duration of the model simulation and the size of the time step, $i = \frac{t}{\Delta t}$. The horizontal velocity is given by u and the vertical velocity is given by w and the magnitude of the velocity is $V_i = \sqrt{u_i^2 + w_i^2}$. The density is given by ρ_i and the angle of the jet axis with respect to the horizontal plane is ϕ_i . The radius and thickness of the plume element are given by b_i and h_i , respectively. The mass of the plume element is $M_i = \rho_i \pi b_i^2 h_i$. For every time step the results of the following equations are calculated. Starting with the mass of the next time step, which is determined by the mass at the current step plus an increase in mass due to shear entrainment. Thereafter the concentration, x- and z-velocity, combined velocity, plume element thickness and radius, jet orientation and jet location are determined. Where the jet location is given by an x and z coordinate, and the length of the jet trajectory s .

Mass:

$$M_{i+1} = M_i + \Delta M_i \quad (5.3)$$

Concentration:

$$c_{i+1} = \frac{M_i c_i}{M_{i+1}} \quad (5.4)$$

Velocity:

$$u_{i+1} = \frac{M_i u_i}{M_{i+1}} \quad (5.5)$$

$$w_{i+1} = \frac{M_i u_i + M_{i+1} \left(\frac{\Delta \rho}{\rho}\right)_{i+1} g \Delta t}{M_{i+1}} \quad (5.6)$$

$$V_{i+1} = \sqrt{u_{i+1}^2 + w_{i+1}^2} \quad (5.7)$$

Thickness and radius:

$$h_{i+1} = \frac{V_{i+1}}{V_i} h_i \quad (5.8)$$

$$b_{i+1} = \sqrt{\frac{M_{i+1}}{\rho_{i+1}\pi h_{i+1}}} \quad (5.9)$$

Orientation:

$$\phi_{i+1} = \arcsin \frac{w_{i+1}}{V_{i+1}} \quad (5.10)$$

Location:

$$x_{i+1} = x_i + u_{i+1}\Delta t \quad (5.11)$$

$$z_{i+1} = z_i + w_{i+1}\Delta t \quad (5.12)$$

$$\Delta s_{i+1} = V_{i+1}\Delta t \quad (5.13)$$

The initial plume element thickness and radius are $D/2$ and the time step Δt is determined by the initial plume element thickness and velocity, $\Delta t = 0.1 \frac{h_0}{V_0}$. The increase in mass is determined by the shear entrainment ($\Delta M_i = E_s$).

$$E_s = 2\pi\alpha_{s_i}b_i h_i V_i \Delta t \quad (5.14)$$

$$\alpha_{s_i} = \sqrt{2} \frac{0.057 + 0.554 \sin \phi_i}{Fr_{l_i}^2} \quad (5.15)$$

$$Fr_{l_i} = \frac{V_i}{\sqrt{g_{red_i} b_i}} \quad (5.16)$$

Where α_s is the entrainment coefficient, Fr_l is the local jet densimetric Froude number and g_{red_i} is the reduced gravity as in Equation 3.7 [25].

5.3. Verification

A first verification step can be done by using data from literature. The second step will be validating the model with small-scale experiments, these results will be shown in Chapter 8. Figure 5.5, shows the dilution with respect to the dimensionless height of a horizontal buoyant jet in still fluid. The model prediction of the current model, called Model 2020, is compared to the JETLAG model prediction and data from experiments done by Cederwall [6, 25]. Based on Figure 5.5, the predicted dilution by the model is acceptable. A slight underestimation is present for lower heights, but the dilution is still in the same order of magnitude.

The centerline trajectory of a horizontal positively buoyant jet in stagnant fluid is given in Figure 5.6 for a Froude number of 2 and 10. This upward bending centerline represents for example the case of a plume exiting a chimney, where the plume has a higher temperature than the ambient temperature, causing the plume to be positively buoyant. Figure 5.6 (a) shows the trajectory for a Froude number of 2, the predicted trajectory by the model is compared to experimental data from Lee and Chu [25]. According to this data the model predicts the trajectory quite accurately. Figure 5.6 (b) also shows a comparison between the predicted trajectory by the model and the experimental data from Lee and Chu, but in this case for a Froude number of 10. Also for this case the model prediction is supported by the data.

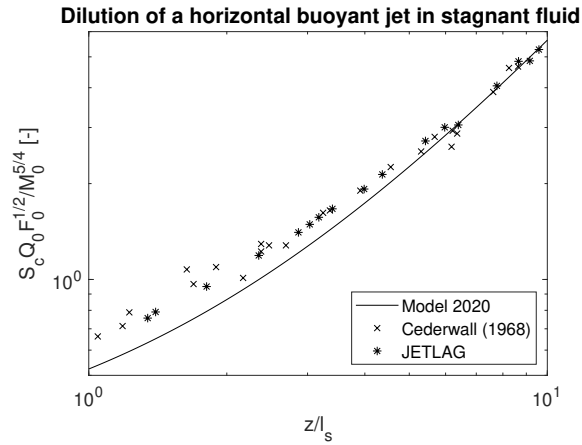


Figure 5.5: Comparison of the predicted dilution of the explained model, called Model 2020, with the predicted dilution from the JETLAG model and measurements for a horizontal buoyant jet in still fluid, where S_c is the centerline dilution, made dimensionless by Q_0 the initial volume flux, F_0 the initial buoyancy flux and M_0 the initial momentum flux

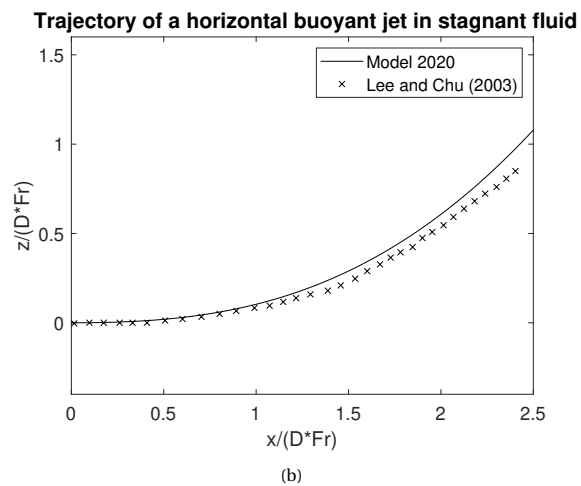
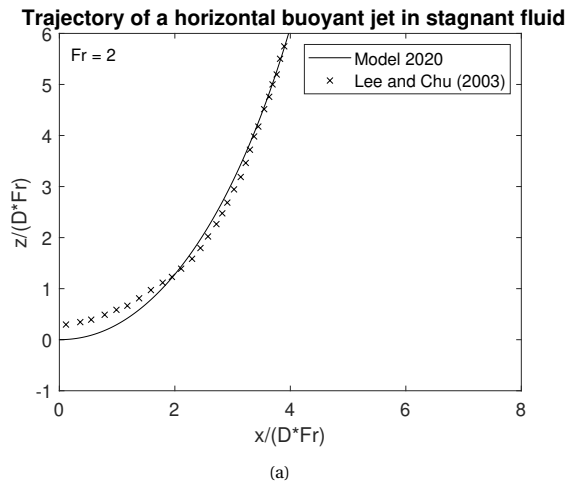


Figure 5.6: Centerline trajectory of a horizontal round buoyant jet in stagnant fluid, comparison between the model prediction of the explained model, called Model 2020, and experimental data from Lee and Chu [25] for (a) $Fr=2$ and (b) $Fr=10$

6

Experiment

This chapter starts by explaining the purpose, setup and execution of the experiments. Then the used measurement instruments and their settings are treated followed by the particle choice, diffuser design and test matrix. Furthermore, the suspended sediment concentration inside the reservoir is discussed.

6.1. Experiment purpose

The main purpose of the tests explained in this chapter is to be able to validate the Matlab model explained in chapter 5, and additionally to gain more insight in the turbulent buoyant jet behaviour. Three types of data are used to validate the model: video images from visualization experiments, concentration measurement data and velocity data.

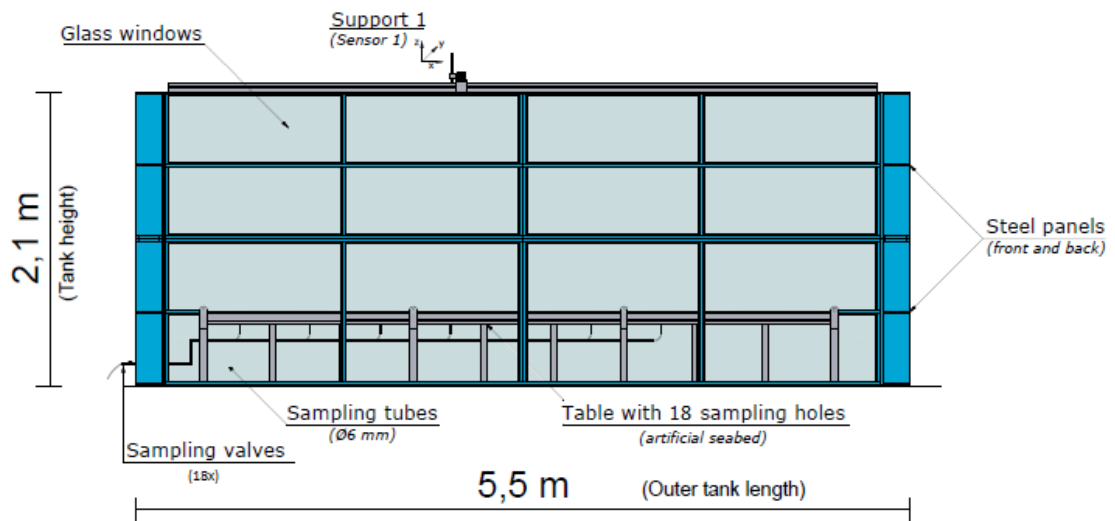
6.2. Experiment setup

The experiment set up is located in the laboratory of Dredging Engineering of Delft University of Technology. It consists of a reservoir, a pump, a flume, a diffuser and connecting hoses and pipes. A front view and top view of the flume are given in Figure 6.1. The flume measures 5.1 m in length, 2.55 m in width and 2.1 m in height. The volume behind the SMT represented by the flume is 76.5x38.25x31.5 m, with a geometric scaling factor of 1:15. A table measuring 4.5 m in length and 1.95 m in width is located at the bottom of the flume representing the seafloor.

A mixture of water and particles is prepared in the reservoir by mixing a predetermined amount of water and particles with two submersible pumps. The reservoir has two compartments, each compartment has a ball valve at the outlet. These are connected to two flexible hoses which connect to a T-piece allowing the pump to be connected to a single flexible hose. The pump pumps the mixture through a pipe connected to the diffuser which exits in the flume. A flow meter is attached to the pipe and the flow is controlled by a ball valve connected to the outlet of the pump.

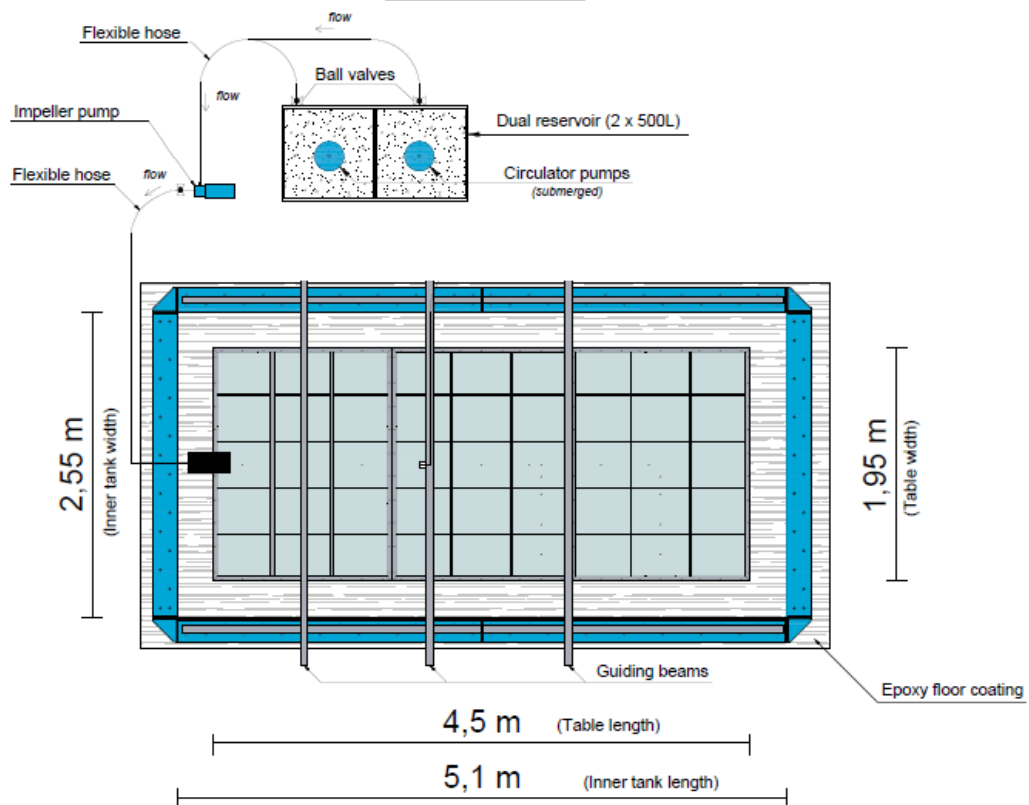
The table located in the flume has build in LED's to be able to illuminate the plume from below. This is necessary for the visualization experiments. On top of the LED's there are perspex plates with photo paper to diffuse the light. This enhances the quality of the images recorded during the visualization experiments. The perspex plates have multiple small diameter holes at predetermined locations that are used to take concentration samples. These holes are connected to tubes which are connected to valves at the outside of the flume to be able to tap water from the flume. The table has a total of 18 sample locations, however during the experiments not all of them will be used. Figure 6.2 shows the five sample points that will be used. These five points are chosen based on the model and the first experiments, indicating that the plume will reach the table between point one and four. Point five is chosen to see if the concentration has returned to the background concentration, indicating that the particles have settled.

Front view



(a) Front view

Top view



(b) Top view

Figure 6.1: Schematic drawing of the (a) front view and (b) top view of the flume

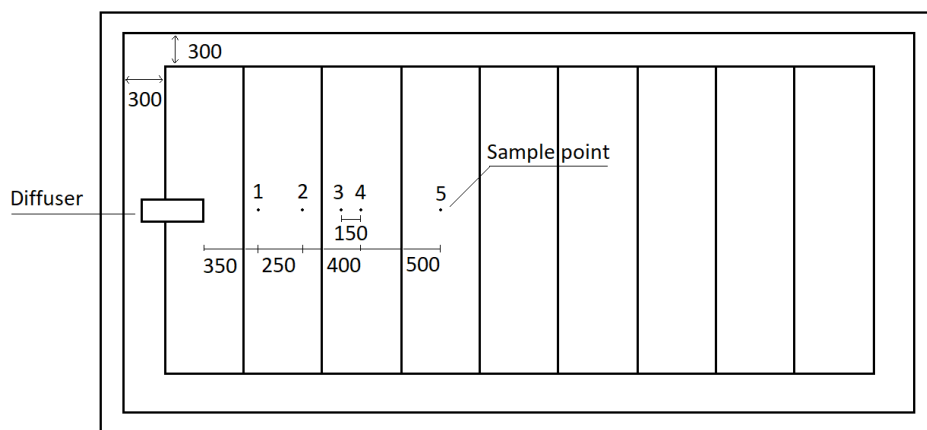
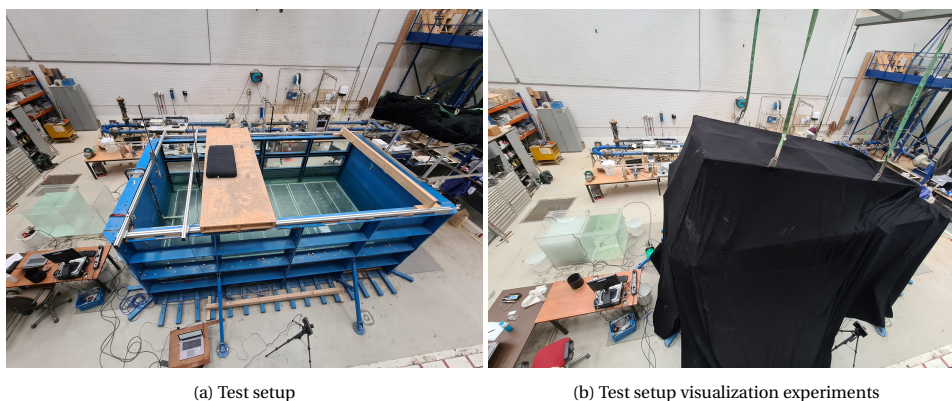


Figure 6.2: Location of the five sample points to determine the concentration, the indicated distances are in millimeters

Figure 6.3 shows the test setup during the experiments. During visualization experiments a large black curtain covers the flume to block the surrounding light, this is necessary to be able to make high quality video recordings of the plume.



(a) Test setup

(b) Test setup visualization experiments

Figure 6.3: Test set up for the (a) experiments and (b) visualization experiments

6.3. Experiment execution

The preparation for one experiment starts with cleaning the table inside the flume by using a water vacuum cleaner to remove the particles from a previous experiment. After this, the velocimetry sensor has to be moved to the correct measurement location and the mixture can be prepared inside the reservoir. The water volume inside the reservoir is calculated to determine the amount of particles that need to be added. After adding the particles, the submersible pumps are turned on a few minutes before the start of the experiment to make sure the mixture is properly mixed. During this time the sensors set up is executed. At the start of the experiment the valves of the reservoir and pump are opened and the flow meter measurements start. The pump valve is tweaked until the correct flow velocity is reached. After two minutes of running at the correct flow velocity the flow is developed and the sensor measuring the velocity profile is turned on. The duration of one test is about 20 minutes. After this all equipment is turned off, and the particles inside the flume are given about an hour and a half to settle. Then the whole sequence starts again. During one day of testing about two to three experiments can be done.

6.4. Measurement instruments

This section explains the working principle of the used measurement instruments and their settings. The used instruments are the Acoustic Doppler Velocimetry sensor, the FASTEC high speed camera and the GoPro Hero7, the KATflow 200 flow meter and the Aquatic turbidity meter.

6.4.1. Acoustic Doppler Velocimetry sensor

The velocity measurements are done with an Acoustic Doppler Velocimetry (ADV) sensor from NORTEK, of the type vectrino profiler, as shown in Figure 6.5. The probe, the bottom part of the sensor, consists of a transmitter and four receiver arms. The sampling volume spans 4-7 cm below the transmitter and gives the velocity in x-, y- and z-direction at every millimeter with a sampling rate of 30 Hz. The sensor uses the Doppler Effect to measure the velocity, a pair of sound pulses is transmitted by the transmitter and partly reflected by the particles in the water. The shifted reflected signal is received by the receiver arms and processed internally by the ADV to give the velocity as an output.

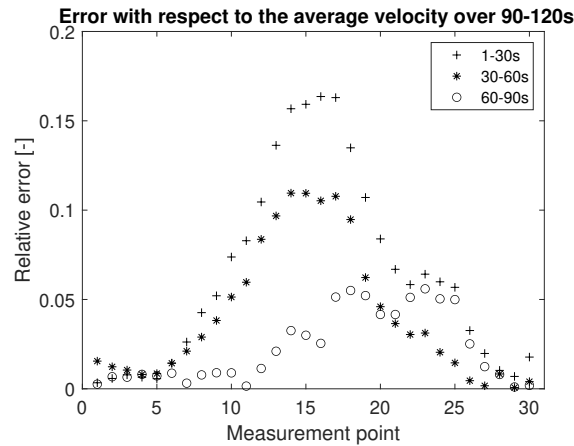


Figure 6.4: Error of the 1-30s, 30-60s, 60-90s average velocities with respect to the average velocity over 90-120s divided by the 90-120s average velocity for one measurement height

During an experiment the ADV measures the velocity for 60s after which it is raised 15mm. By raising the ADV 15mm instead of 30mm, overlap is created between the different measurement locations. This enhances the accuracy of the results because the sensor has the highest accuracy at the center of its measuring range. The choice of measuring a minute at each location is based on a test where the ADV was kept in place for two minutes. Subsequently the difference between the average velocity over 90-120s and the 1-30s, 30-60s and 60-90s average velocities were determined. This difference was then divided by the previously determined average velocity over 90-120s to get the relative error shown in Figure 6.4. The graph shows the relative error at one of the measuring heights that was used to choose the measuring time. As can be seen the relative error gets smaller by increasing the measuring time. The measurement of the shown graph was in the center of the diffuser. For the determination of the needed measurement time multiple graphs at different measurement heights were used. By comparing these graphs the choice was made that measuring for 60s would be sufficient to reduce the error due to the displacement of the ADV to another measurement height. Increasing the measuring time to 90s was considered not beneficial because this would increase the the measurement time by 50% and due to the limited amount of time available this implies a reduction in amount of measurement locations during a test. Since the achieved relative error with a measurement time of 60s is maximum 10 percent, this was considered as a good compromise between accuracy and amount of measurement locations.

6.4.2. High speed camera and GoPro

During visualization experiments the FASTEC-IL5 high speed camera is used to make high speed side view recordings of the plume. These recordings, together with top view recordings from a GoPro HERO 7, give information about the behaviour of the plume. The FASTEC high speed camera is set to have a resolution of 1600x600, frame rate of 130 fps and a shutter speed of 0.350 ms. The GoPro has a frame rate of 60 fps. Figure 6.6 shows the location of the high speed camera during the visualization experiments. The GoPro is connected to the frame carrying the black curtain.

6.4.3. KATflow 200

The KATflow 200 flow meter from Katsonic gives the flow through the PVC pipe connected to the diffuser. The sensor measures the flow velocity every second by emitting ultrasonic signals from two transducers located on the PVC pipe, as shown in Figure 6.7. These signals are emitted alternately in the direction of the flow and

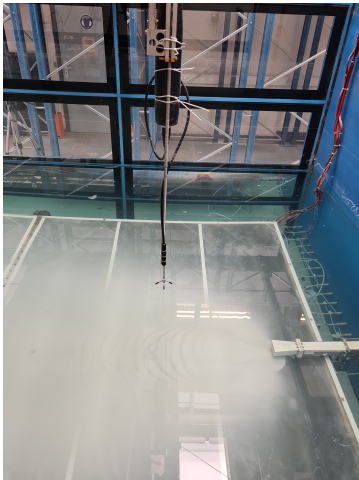


Figure 6.5: The ADV sensor



Figure 6.6: High speed camera position during testing

opposite to the flow direction. The transit time of the signal in the direction of the flow will be shorter than the transit time of the signal against the flow direction. The difference between these two signals is measured and used to determine the average flow velocity. Figure 6.8 shows the control module of the flow meter. Before every test the temperature of the mixture, needed to ensure the density for the flow calculation is correct, is changed to the measured temperature in the reservoir.



Figure 6.7: Attachment of the transducers to the PVC pipe



Figure 6.8: The control module of the flow meter

6.4.4. Aquatic turbidimeter

The turbidimeter is used to determine the turbidity in Nephelometric Turbidity Units (NTU) of the samples taken from the 'tab points' in the flume. These values are converted to a concentration in gram per liter by the graph given in Figure 6.10. This graph is determined by measuring samples with a known concentration in the turbidity meter. An image of the used turbidimeter is shown in Figure 6.9.

6.5. Particle choice

The choice of particles for these tests was based on the limitations of the flume while still wanting particles that are representative for the expected plume in deep sea mining. Testing with sediment that has a Particle Size Distribution (PSD) similar to that found in the deep sea is not achievable in this flume. The amount of particles that would have settled at the end of the flume would not have been sufficient before the plume hits the back of the flume and reflects [27]. Therefore the choice was made to look at larger particles like glass beads used for surface cleaning and shot peening. These particles have a density similar to the deep sea sediment and are available in multiple particle size distributions. Since there already is experience with these particles, which showed that these particles are representative for the behaviour of a plume, these particles were chosen.

Two particle size distributions of these glass beads were investigated, 40-70 micron and 65-105 micron. The



Figure 6.9: The Aqualitic turbidimeter [41]

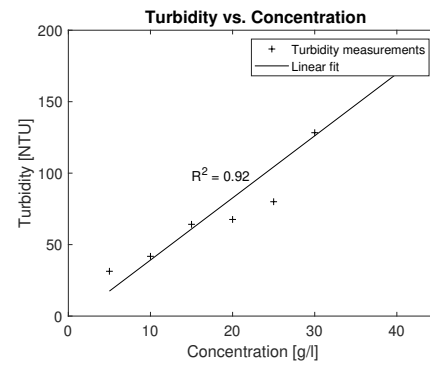


Figure 6.10: Turbidity to concentration conversion

choice between the two is made by comparing the advantages and disadvantages while keeping in mind the goal of these tests, which is to be able to validate the previously explained Matlab model. The two particle sizes are compared based on five points:

- Representative: how close are the particle sizes to the deep sea sediment particle sizes?
- Mixing: how well do the particles mix in the reservoir?
- Number of tests: the amount of tests that can be executed in the three months available for testing
- NTU measurements: the accuracy of the NTU measurements with the turbidity sensor
- Duration of test: the possible length of a test, this can be shortened due to contamination of the flume, reducing visibility

Figure 6.11 shows the PSD of both particle sizes, a sample of both particle sizes was analysed by Ahmad Sha-keel in a Malvern Mastersize 2000 from Deltares. The Malvern Mastersize 2000 analyses the sample based on laser diffraction. The d_{50} for the particle size 40-70 μm is 66 μm and for the particle size 65-105 μm , 89 μm . The sediment discharged during the mining operation has particle sizes smaller than 90 μm , with a d_{50} of around 8 μm [23]. Compared to the d_{50} of the sediment during the mining operation, both considered particle sizes for testing are significantly coarser. Therefore the difference in representation of the sediment discharged during the mining between the two particle sizes is considered minor for these experiments.

The coarser particles have higher settling velocities and are therefore more difficult to keep in suspension. The problem of mixing the coarser particles was solved by using two submersible pumps in one compartment of the reservoir, creating more turbulence to keep the particles in suspension.

The number of tests was considered most important because of the limited time available for testing. Testing had to be done in three months of testing three days a week, of which the first month was needed for sensor calibration and getting familiar with the test setup. With the coarser particles about two to three tests a day can be done. With the finer particles this is about one or two tests, due to the longer time needed for particles to settle between tests because of the lower settling velocities.

The NTU measurements will give less accurate results due to the larger settling velocity of the particles, this was observed during the calibration of the turbidimeter. The particles of 40-70 μm have a σ/μ (standard deviation/average) value of 10% and the particles of 65-105 μm have a σ/μ value of 15%. Although the accuracy of the measurement for the finer particles was better, the lower accuracy of the coarser particles was accepted due to the advantage of the number of tests that can be executed with these particles.

The test duration between both particle sizes is limited by the amount of mixture in the reservoir. However, while testing with the finer particles it was observed that these particles contaminate the flume in a few minutes. Due to the fast contamination it was assumed that these particles would possibly reflect from the sidewalls and back wall of the flume. This would cause interference with the measurements, especially because the test duration will be around 20 minutes.

Thus, the particle size of 65-105 micron was chosen. The particles of 40-70 micron will still be used for a single visualization test to be able to compare the behaviour of the finer particle size with the 65-105 micron particles.

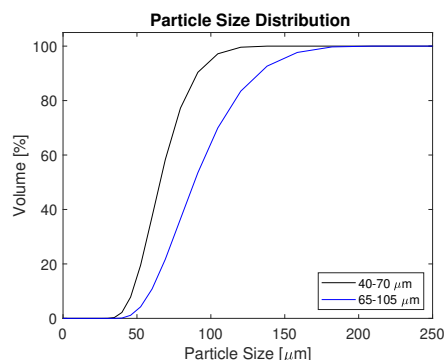


Figure 6.11: Cumulative particle size distribution for 40-70 μm (black) and 65-105 μm (blue)

6.6. Diffuser design

The diffuser is designed based on the explanation given in Section 3.5 and Figure 3.7. The diffuser is designed to operate in the no stall region, where no flow separation is present. The length over width ratio, L/W , is 3.3 and the angle 2θ is 11 degrees. Figure 6.12 shows the final design of the connection piece and the diffuser which are bolted together with a flange. Since a 90 degree bend is necessary because of length limitations of the flume, the length of the connection piece needs to ensure a developed flow profile at the inlet of the diffuser. According to Cimbala (2006) a straight connection piece length of $10D$ is necessary for the flow profile to recover from the bend [8]. Where, in this case, D is the hydraulic diameter for a rectangular cross section.

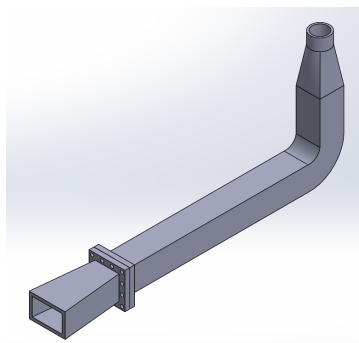


Figure 6.12: Diffuser design

6.7. Test matrix

The test matrix is shown in Table 6.1. The experiments were done at three diffuser heights, 200 mm, 100 mm and 50 mm, and two diffuser outlet velocities, 0.27 m/s and 0.37 m/s. The initial concentration is equal for all experiments and has a value of 25g/L. The diffuser height is the height of the bottom of the diffuser above the table. The choice of the heights is based on common heights of the full scale SMT. With a geometric scaling factor of 1:15 the tested heights of the diffuser are 3 m, 1.5 m and 0.5 m above the seafloor, respectively. The velocities correspond to a full scale diffuser outlet velocity of 0.77 m/s and 1.55 m/s, respectively. The test numbers without an ADV location are the visualization experiments which are done at each diffuser height for both velocities.

The initial choice of diffuser outlet velocity was different from the presented diffuser outlet velocities and was based on the Froude number, Reynolds number and common discharge velocities for the SMT. However,

during the first experiments a problem with the flow at the diffuser outlet was encountered (further explained in Section 7.2.1). Therefore the velocities were adapted to a velocity which is more relevant for the actual discharge velocity encountered in the mining operation, 0.27 m/s, and a velocity where the problem does not occur, 0.37 m/s. The two diffuser outlet velocities correspond to a flow rate of 0.3 l/s and 0.6 l/s through the pipeline where the flow meter is attached.

The ADV measurements are done at three locations, 5D, 10D and 15D, in which D is the inner height of the diffuser outlet and the distance is measured with respect to the diffuser outlet. At a height of 100 mm a fourth measurement location at 50D from the impingement point (the point where the center of the plume reaches the table) was chosen as well. These extra measurements were done to gather knowledge about the density current.

Test number	Height (mm)	Velocity (m/s)	ADV location
1	200	0.27	5D
2			10D
3			15D
4	200	0.37	5D
5			10D
6			15D
7			50D
8	200	0.27	-
9	200	0.37	-
10	100	0.27	5D
11			10D
12			15D
13			50D
14	100	0.37	5D
15			10D
16			15D
17			50D
18	100	0.27	-
19	100	0.37	-
20	50	0.27	5D
21			10D
22			15D
23	50	0.37	5D
24			10D
25			15D
26	50	0.27	-
27	50	0.37	-

Table 6.1: Test matrix

6.8. Suspended sediment concentration

Measurements of the SSC in the reservoir for the duration of one test are shown in Figure 6.13, mixture samples were taken in the bottom part of the reservoir. It can be seen that the measurements have a large error and that the measured concentration in general is higher than expected. This can be explained by uneven mixing in the reservoir. The mixing in the reservoir is done by two submersible pumps which are placed on the bottom of the reservoir. They are placed in opposite corners to create a flow through the whole reservoir, keeping the particles in suspension. Because the pumps are placed on the bottom of the reservoir and the intake and output of these pumps are also located on the bottom of the reservoir the pumps cannot generate enough turbulence to create an even distribution of particles over the reservoir. The generated turbulence is assumed to be the largest at the bottom of the reservoir and lower in the upper region of the reservoir. This could explain the high measured concentrations at the bottom of the reservoir, since less particles are suspended in the upper region more particles are located in the lower region of the reservoir. The concentration

at the bottom of the reservoir during the experiments is approximately 30% higher than the predetermined concentration of $c_0=25\text{g/l}$. This means that the concentration at the diffuser outlet will be higher than expected.

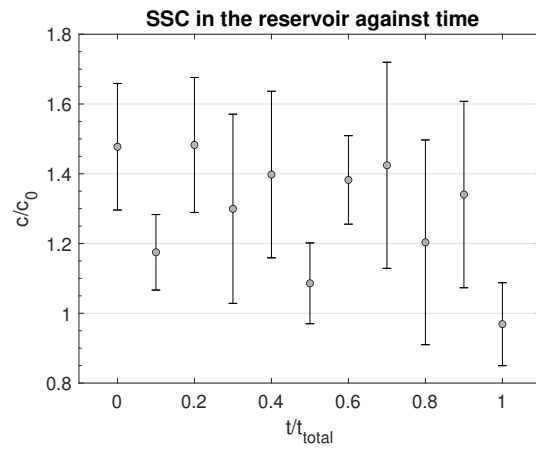


Figure 6.13: Measurements of the reservoir concentration over the duration of one test

7

Results experiment

This chapter discusses the results of the experiments, starting with the results of one set of experiments with the same initial conditions. After this, the troubleshooting for two problems encountered during the experiments is discussed. Lastly, the analysis of the experimental results is treated.

7.1. Results

This section displays the results of multiple experiments with the same initial conditions, namely a diffuser height of 100mm and an initial velocity of 0.27m/s. The results for the other experiments are shown in Appendix A. The measured SSC is discussed first, followed by the velocity profile, bottom deposition pattern and impingement range. Furthermore a comparison with finer particles is given and the behaviour of the buoyant jet for a densimetric Froude number smaller than one is discussed.

7.1.1. Concentration

The concentration is determined by measuring the turbidity in NTU with the turbidimeter and calculating the average concentration and the standard deviation for each sample location. Subsequently the NTU value is converted into gram per liter with the calibration graph shown in Figure 6.10. The results for experiment 10 are shown in Figure 7.1, displaying the dimensionless concentration c/c_0 against the dimensionless horizontal distance x/D compared to the background concentration. The value for c_0 is not adjusted to the measured higher reservoir concentrations and has a value of 25g/L. For this particular experiment samples were taken from the first 4 sample points because sample point 5 was clogged during the experiment. Fortunately, this did not cause a lack of data because the measured concentration at location 3 and 4 are already close to the background concentration, indicating that the suspended sediment in the plume has settled already. It can be seen that the relative concentration c/c_0 increases for the first two sample locations and subsequently decreases to the background concentration. The increase in the first location shows that the particles start to settle, at the second location the amount of settling particles has increased as indicated by the higher relative concentration. This shows that the buoyant jet impinges in the range of these two points.

7.1.2. Velocity profile

For each combination of initial conditions a vertical velocity profile at three locations is measured. To obtain the graph shown in Figure 7.2, the velocity measurements at each measurement height are averaged over a duration of 30s. The velocity profile is determined by measuring a profile of 30mm for 60s at each height, subsequently raising the sensor 15mm obtaining overlapping velocity profiles. These overlapping measurements are averaged as well, giving one velocity value at each millimeter along the vertical velocity profile. The resulting graph in Figure 7.2 shows the velocity profile obtained for experiment 10, 11 and 12, where $z/D = 0$ is the height of the center of the diffuser outlet and $x/D = 0$ is the horizontal location of the diffuser outlet. The lower bound of the y-axis gives the location of the bottom boundary. The red arrows indicate measurements with an SNR value lower than or equal to 40dB. This value is based on the jump in the SNR data profiles, corresponding to the location of the erroneous velocity profile explained in Section 7.2.2. An example of a graph showing this jump is given in Appendix A Section A.2.1. The development of the buoyant jet can be noticed by the Gaussian profile visible at $x/D = 5$ and the downward direction of the velocity vectors at the bottom

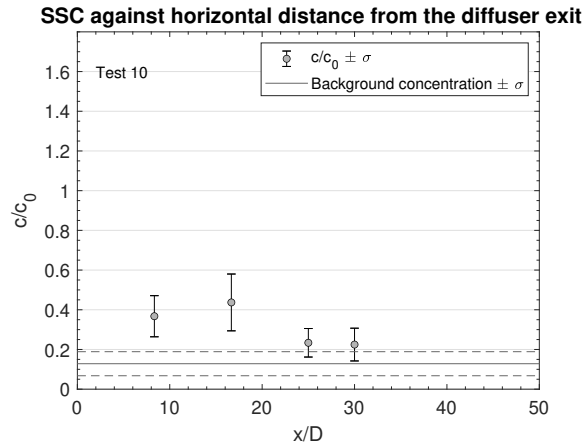


Figure 7.1: Dimensionless SSC at the sample locations 1, 2, 3 and 4 compared to the background concentration for test 10 ($h=100$ mm, $u_0=0.27$ m/s)

of the profile at $x/D = 10$ and $x/D = 15$. Indicating that the buoyant jet trajectory bends downward until it reaches the bottom, subsequently moving further as a density current. The increase in velocity for $z/D > 0$ is the erroneous velocity profile explained in Section 7.2.2. The velocity profile measured at $50D$ from the impingement point is shown in Figure 7.3 and depicts the velocity inside the near bottom turbidity current. It can be seen that the velocity has decreased significantly at this location but there is still a forward velocity present at the lowest measurement points, this is the density current. Almost all measurements are shown in red because of their low SNR values. However, since the amount of particles is low at all measurement heights at this location, this is expected and does not mean that these measurements are wrong. The x -, y - and z -velocity profiles for test 10 are shown in Figure 7.4, the y - and z -velocity profiles show a velocity of approximately 0 m/s. The z -velocity profile shows a slightly negative velocity below the diffuser centerline, indicating the settling particles and the bending of the buoyant jet.

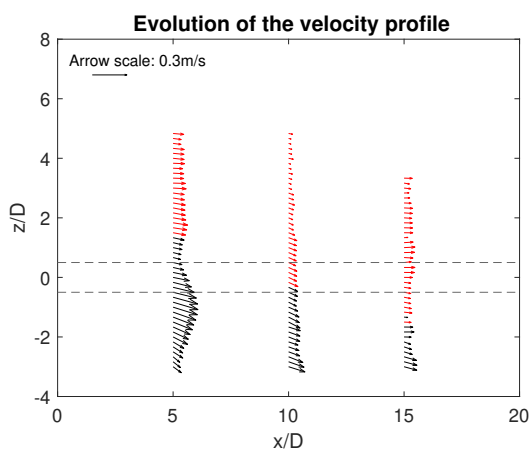


Figure 7.2: Velocity profile for experiment 10, 11 and 12, where $z/D=0$ is the center of the diffuser exit, the dotted lines indicate the diffuser boundaries, the lower bound of the y -axis is the location of the bottom boundary and the red arrows resemble less reliable measurements

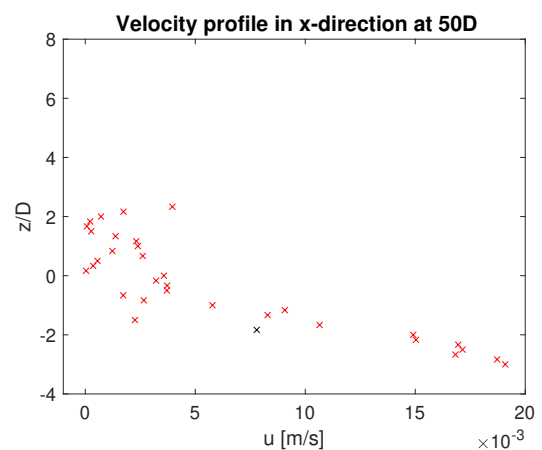


Figure 7.3: Velocity profile in x -direction at $50D$ from the impingement point, the red arrows resemble less reliable measurements

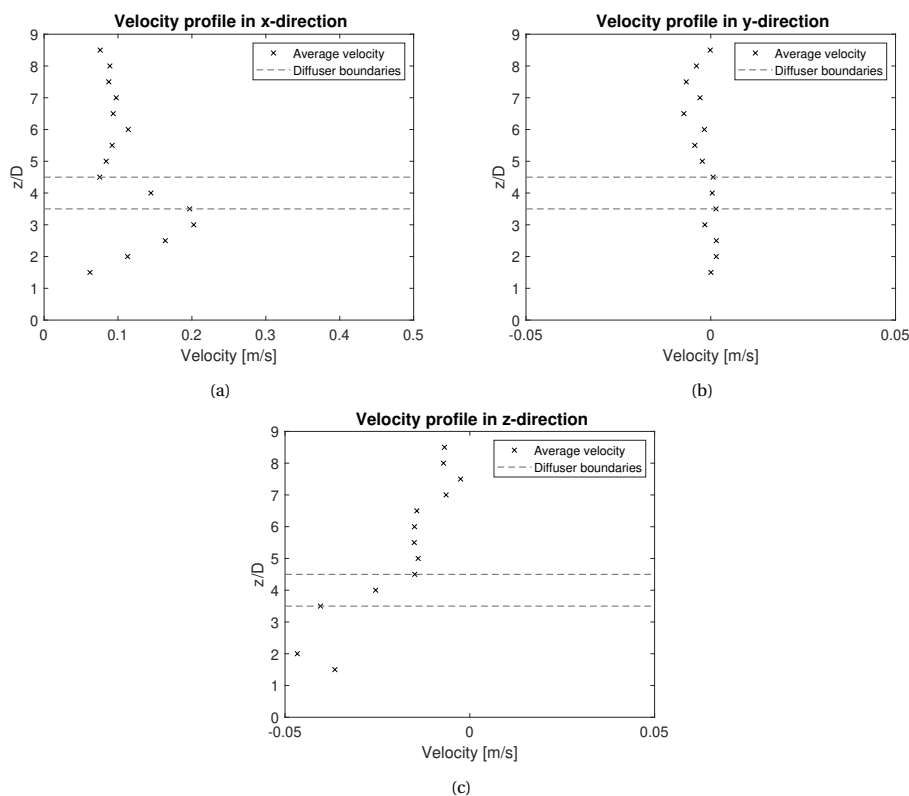


Figure 7.4: Velocity profile for test 10 in (a) x-direction (b) y-direction and (c) z-direction

7.1.3. Bottom deposition pattern

The bottom deposition pattern is determined based on the GoPro footage. First the base frame is determined, see Figure 7.5 (a). This frame serves as a reference for determining the amount of bottom deposition. Then the superposed image is determined by converting the images over a time interval of 15s into greyscale images and superposing these images. A certain start and end time can be chosen, for example, in the image shown in Figure 7.5 (b), the start time is $t=420s$ and the end time is $t=435s$. To create the image in Figure 7.5 (c), the superposed image is divided by the base frame and a step filter is applied to smoothen the edges of the deposition pattern. Figure 7.5 (c) shows the bottom deposition, and is used to determine the contours shown in Figure 7.6. This is done by visually locating the points composing the boundary of the deposition and converting these points into a plot. Since the first 120s of each test are needed to obtain the desired flow velocity, the first deposition contour is determined at $t=120s$. The contour at $t=420s$ shows the final deposition pattern, five minutes after the first contour. The bottom deposition pattern of experiment 18 is shown in Figure 7.6, this experiment has the same initial conditions as experiment 10, 11 and 12, shown in the previous figures. It can be seen that the contour is approximately symmetrical and increases in y-direction with time.

7.1.4. Impingement range

The high speed camera footage is used to determine the impingement range of the buoyant jet. However, due to the density current followed after impingement no distinction could be made between the furthest edge of the impingement range and the subsequent density current. Furthermore, due to the strong light from below the plume it was difficult to make a distinction between the location of the nearby edge of the impingement range and the light from the bottom panel, the flow is too opaque to observe a difference. Moreover, the density current develops in all directions, thus also in the direction of the diffuser. This means that what is determined as the beginning of the impingement range, actually is the outer boundary of the density current. Based on the current footage no distinction can be made between the two, however, the difference is assumed to be small due to the low discharge heights. This will cause the density current to spread more towards the positive x-direction since the bottom velocity still has a large component in x-direction. For experiment 18 the start of the impingement range is approximated by visual inspection of a 30s average image, and is $x/D \approx 5$. This agrees with the shown concentration and deposition pattern when compared to Figure 6.13 and Figure

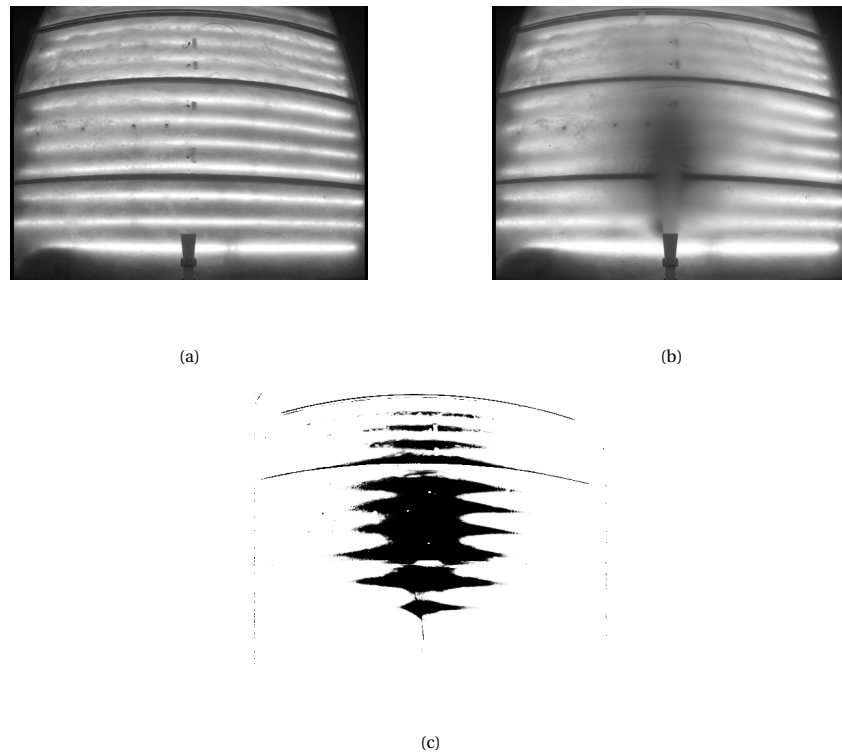


Figure 7.5: Image processing steps to determine the bottom deposition pattern, with (a) the base frame, (b) the superposed image, and (c) the final filtered image at $t=420s$

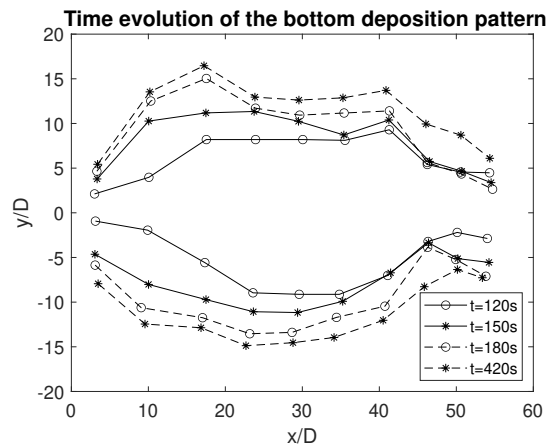


Figure 7.6: Bottom deposition pattern through time, experiment 18

7.6. It can be seen that the concentration is higher than the background concentration at $x/D \approx 8$, indicating that the buoyant jet has reached the bottom and $x/D \approx 5$ corresponds to the start of the lateral spreading of the contour.

7.1.5. Comparison particle sizes

In addition to the experiments done with a particle size of 65-105 micron, two visualization experiments for a particle size of 40-70 micron were done. These tests have a diffuser height of 100mm and initial velocity of 0.27m/s and 0.37m/s, and are compared to test 18 and 19, which have the same starting conditions.

Figure 7.7 shows the comparison of the final bottom deposition pattern for an initial velocity of (a) 0.27m/s and (b) 0.37m/s. For $u_0=0.27m/s$, the spreading in the x-direction of the finer particle size is less than for

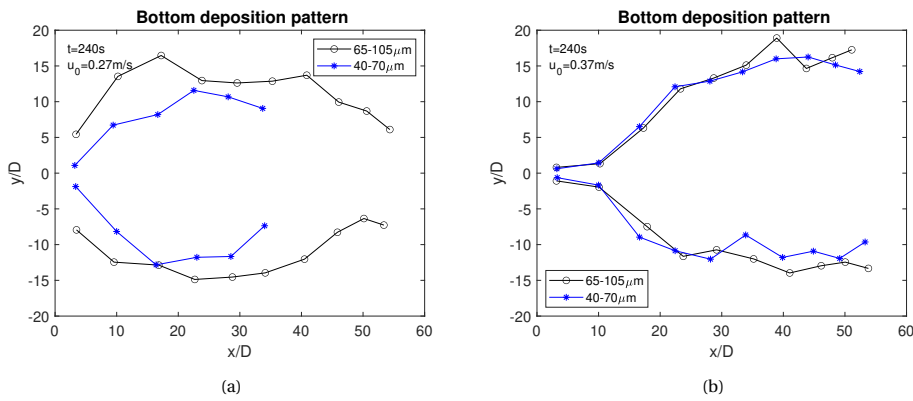


Figure 7.7: Bottom deposition pattern for both particle sizes, 65-105 micron in black and 40-70 micron in blue, and an initial velocity of (a) 0.27m/s and (b) 0.37m/s at t=420s

the coarser particle size. This difference can be explained by the way the contour is determined, namely in the same way as explained in Section 7.1.3. The finer particles will stay longer in suspension because of their lower settling velocity, thus the particle build up height is less, making it harder to detect the visual edge. This can be noticed when comparing Figure 7.8 (a) and (b), showing the filtered images of the bottom deposition for an initial velocity of 0.27 m/s at time $t=420s$ for a particle size of 65-105 micron and 40-70 micron, respectively. The grey area in the left image shows the amount of settled particles, a darker area means more particles are present. In the right image the grey area is less evident, indicating that less particles have settled. This shows that the coarser particles settle faster than the finer particles. The bottom deposition pattern for a higher velocity shows no significant difference between both particle sizes, but a similar difference in thickness of the bottom deposition is noticed as in the case of $u_0=0.27m/s$.

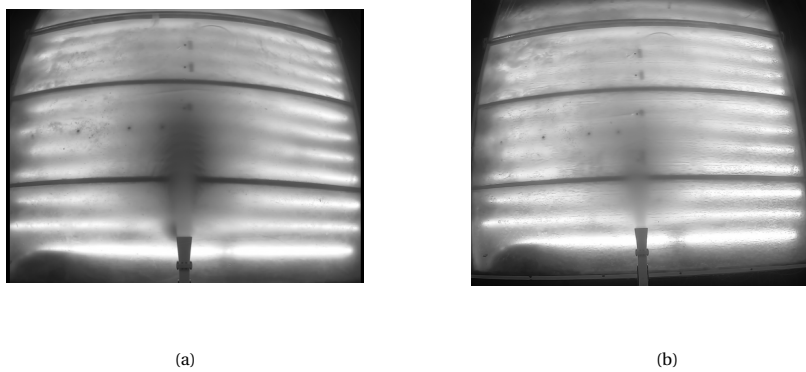


Figure 7.8: Filtered average image of bottom deposition for a particle size of (a) 65-105 micron, test 18 and (b) 40-70 micron, test 30 at $t=420s$

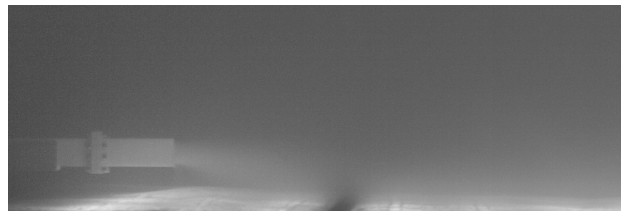
A comparison of the start of the impingement range (x/D), determined through image processing of the high speed camera footage, between the two particle sizes is shown in Table 7.1. The determined start of the impingement range for both particle sizes are quite similar for both initial velocities. However, since fine particles stay longer in suspension, the beginning of the impingement range is expected to be further away from the source. This cannot be seen in Table 7.1, and can be explained by the small difference in d_{50} and the determination of the start of the impingement range through visual inspection of the camera footage.

Table 7.1: Comparison of the impingement point for a particle size of 40-70 micron and 65-105 micron

u_0 [m/s]	40-70 micron x/D	65-105 micron x/D
0.27	3.5	5
0.37	11	10

7.1.6. Densimetric Froude number <1

To investigate the behaviour of the buoyant jet for a densimetric Froude number inside the subcritical region, meaning it is lower than the one (see Section 3.2.4), a visualization experiment was done. The Froude number was lowered by decreasing the initial velocity to 0.03m/s, while keeping all other initial conditions the same. The experiment was done at a diffuser height of 50mm. In Figure 7.9 the averaged image of the high speed camera footage for a densimetric Froude number of 0.5 and 3.5 are shown. The experiment with a densimetric Froude number of 3.5 was experiment number 26, which has the same initial conditions except for a higher initial velocity of 0.27m/s to obtain a densimetric Froude number of 3.5. Despite of the higher initial velocity in Figure 7.9 (b) the buoyant jet bends earlier than the buoyant jet in Figure 7.9 (a). The maximum velocity in a buoyant jet with $Fr_0 < 1$ is located at the boundary of the buoyant jet, preventing entrainment of ambient fluid. This also causes particles to stay inside the buoyant jet for a longer time, causing the bending of the buoyant jet to start later than for $Fr_0 > 1$. Figure 7.10 shows the GoPro footage, where the diffuser contour can be noticed at the right of the figure. In front of the diffuser some slightly darker spots can be noticed, these are a combination of the buoyant jet and settled particles. Due to the high intensity of the LEDs, only a part of this is visible, but in reality the buoyant jet and particle deposition are continuous. It can be noticed that the darker spots increase in width only slightly, meaning that the buoyant jet barely spreads laterally, this indicates that there is practically no entrainment of the ambient fluid, as would be expected with a densimetric Froude number lower than one.



(a)



(b)

Figure 7.9: Averaged image of the high speed camera footage for a densimetric Froude number of (a) 0.5 and (b) 3.5

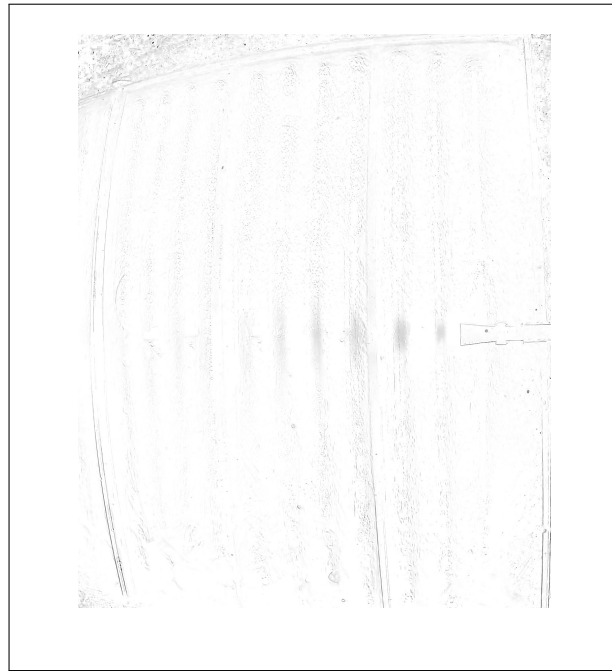


Figure 7.10: GoPro image of the average image relative to the background, the diffuser can be seen on the right and the slightly darker spots in front of the diffuser is the buoyant jet

7.2. Troubleshooting

During the experiments two problems were encountered and further investigated, the explanation of both problems is given in this section. The first problem was the fall-out of sediment at the diffuser outlet, this phenomena was noticed while starting with the first experiments. The second encountered problem was discovered while analysing the data, where an erroneous velocity profile was noticed.

7.2.1. Fall-out of sediment at diffuser outlet

During testing a phenomena was encountered where sediment seemed to fall out the bottom of the diffuser outlet, as can be seen in Figure 7.11. Multiple actions were taken to determine the cause of this phenomena.

- Alignment of the diffuser
- Increase the flow rate
- Change the start up procedure
- Use of a by-pass over the pump to limit the flow rate
- Polish the bottom edge of the diffuser exit
- Calculate the critical flow velocity
- Measure the x-velocity profile at the diffuser exit

The alignment of the diffuser was checked, bad alignment of the diffuser might influence the velocity profile inside and at the exit of the diffuser. It was found that the coupling piece and the diffuser were not properly aligned. However, after alignment and testing it was concluded that the problem was not solved.

A next step in searching for the cause of the problem was taken by testing if the phenomena was present at multiple flow rates. The flow rate was increased step by step and it was concluded that at a flow rate of 0.6 l/s and above, corresponding to a flow velocity of 0.4 m/s through the system, the phenomena is not present anymore. However, this did not solve the problem since testing at flow rates above 0.6 l/s would be less relevant for deep sea mining purposes.



Figure 7.11: Sediment fallout

The valve located at the pump outlet regulates the flow rate, to check if this valve influences the occurrence of the phenomena, the pace with which the valve is opened and closed is altered. For example, for one test the valve is completely open initially, the flow rate is now at its maximum. Then the valve is closed slowly until the required flow rate is reached. The idea behind this, is that by closing the valve rapidly the flow inside the pipe also changes rapidly, causing a sudden flow change that influences the outlet flow profile. However, if the valve is closed slowly the flow does not encounter a sudden change and the flow profile has time to recover. Unfortunately, after testing different procedures, for example first opening the valve completely and then slowly closing it until the right flow is reached, it was found that this did not solve the problem.

In order to limit the use of the pump valve to regulate the flow rate a by-pass was used. With the by-pass an extra flexible hose connected to the pump inlet and exiting inside the reservoir is meant. The amount of mixture flowing through the by-pass can be regulated by a ball-valve, hereby the flow through the pump can be limited. The idea behind this is similar to the previous point, limiting the closure of the pump valve to minimize the interference with the flow. However, after testing it was found that this also did not solve the problem.

The next step was to polish the edge of the diffuser outlet to create a smoother path for the flow to follow when exiting the diffuser. However, this as well did not solve the issue.

The critical flow velocity, the minimum velocity necessary to keep particles of a certain size in suspension, was calculated to see if this was causing the sediment to form a granular bed. The calculated critical flow velocity for particles of 65 micron is 0.23 m/s and for the particles of 105 micron 0.41 m/s. This is based on the MTI model [29], however this is an empirical model based on data for circular pipelines with a diameter larger than 200 mm, while the coupling piece and diffuser have a rectangular cross-section with a height of 30 mm. Other models used to calculate the critical velocity pose the same problem. Inside the PVC pipe section the velocity is around 0.55 m/s and it slows down to an average velocity of approximately 0.3 m/s at the diffuser exit. Thus the exit velocity is lower than the critical velocity, which might explain why the sediment falls out of the diffuser exit. However, it remains uncertain if this causes the problem since the critical velocity calculations are based on a model that is not valid for a small diameter and rectangular pipe section.

During testing of all these possible solutions, the x-velocity profile at the diffuser exit was measured. Figure 7.12 shows the profiles at the diffuser exit at both flow rates. It can be seen that the flow in the x-direction shows a Gaussian profile, as should be according to theory. As can be seen in both figures the highest speed is not encountered in the centre of the diffuser as would be expected. However, this could be caused by the fact that the velocity profiles are not measured immediately at the exit of the diffuser but approximately 6 cm in front. This is because the ADV could not measure closer to the exit due to the length of the receiver arms. The Lagrangian model of Chapter 5 was used to determine the expected bending of the centerline velocity at a distance of 6 cm from the diffuser outlet. This resulted in an expected height difference of 4mm for an initial flow velocity of 0.27m/s and 2mm for an initial flow velocity of 0.37m/s. Indicating that the bending of buoyant jet lowers the profile. For the initial flow velocity of 0.27m/s it can be seen that the measured velocities at

the bottom of the diffuser are lower than those at the top. This is not the case for the other flow velocity. This shows that there is a difference in velocity profile between the two flow velocities but this could be the result of the phenomena and shows that it is possible that the phenomena has an influence on the measured results.

In addition, it was noticed that the phenomena did not always occur even though the initial conditions were the same, adding to the confusion of what might be the cause. In the end it was decided that due to time limitations the search for the cause of this phenomena would stop and the presence of this phenomena in experiments at velocity of 0.27 m/s would be accepted.

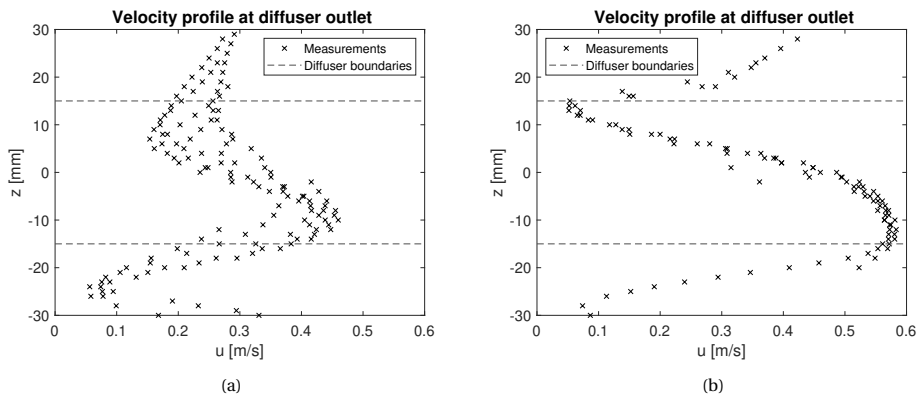


Figure 7.12: Velocity profile of the velocity in x-direction at the diffuser outlet for an initial velocity of (a) 0.27m/s and (b) 0.37m/s

7.2.2. Erroneous velocity profile

During multiple tests a velocity significantly larger than zero was noticed in the velocity profiles above the buoyant jet. At these locations the velocity is expected to be around zero, since the buoyant jet does not influence these locations. One of these velocity profiles, measured at location 2 (see Figure 7.13) and the corresponding SNR profile above the buoyant jet are shown in Figure 7.14. The SNR (Signal-to-Noise Ratio) is the amplitude relative to the instrument noise level and is measured in decibels. The higher the ratio the better the signal strength. If the mean of the data over a certain time is taken, which is the case for these graphs, an SNR value of at least 5 dB is recommended by Nortek [33]. As can be seen from Figure 7.14 (b), the SNR value stays above the recommended 5 dB. However, it can also be noted that the SNR value decreases when the measurement height increases, this is due to the decrease in particle concentration. Thus the noise at the highest measurement points is larger than at the lower measurements points resulting in a lower accuracy for the measured velocities at these higher measurement points.

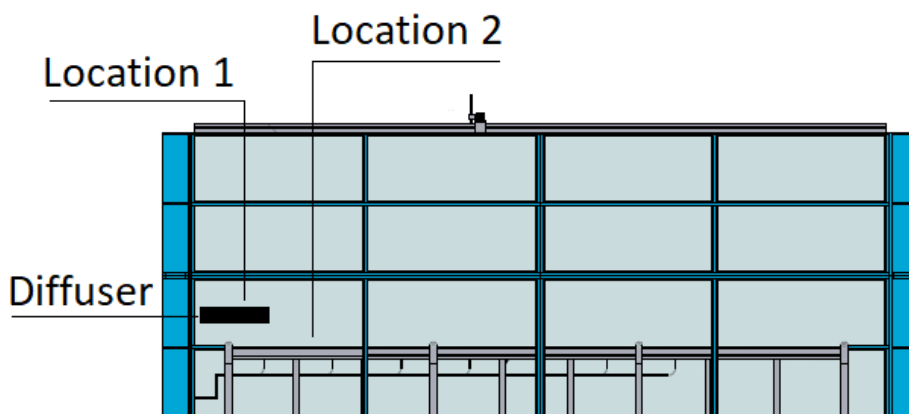


Figure 7.13: Measurement locations of the measured velocity profiles above the diffuser and buoyant jet

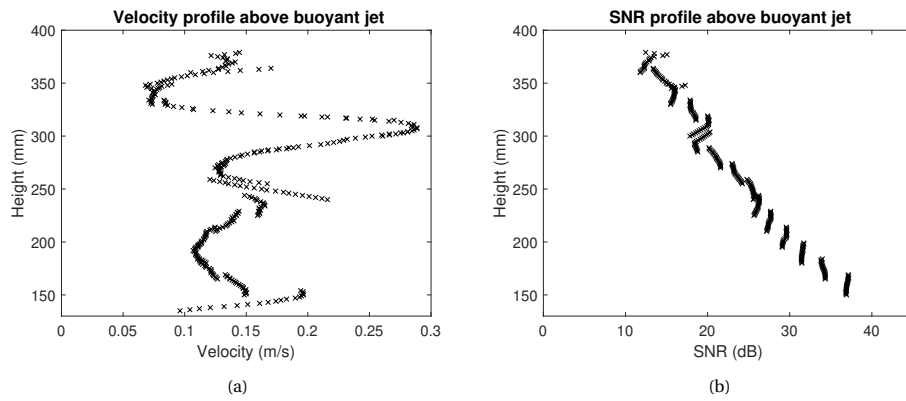


Figure 7.14: Profile of the (a) x velocity and (b) SNR above the buoyant jet

Since the SNR profile only shows a lower accuracy of the measurement points, this could not with certainty be seen as the cause of the high velocities measured. As a next step to find the cause, velocity measurements above the diffuser were taken, location 1 in Figure 7.13, while discharging at an initial flow velocity of 0.27m/s, showing whether the faulty velocity measurements are caused by the flume. Figure 7.15 shows the graphs of the velocity and SNR profile resulting from these measurements. It can be seen that the SNR value stays above 10dB, however, at a height of approximately 220mm and higher the SNR value decreases significantly. The x-velocity profile shows that the velocity is approximately zero at the beginning but increases from a height of approximately 220mm onward. Since these results are not conclusive as well, another test was done to exclude that the faulty velocity profile is caused by the flume. A cord with a nut attached as mass, was lowered into the flume while discharging the buoyant jet. Above the diffuser the cord did not show any movement, indicating that no velocity was present. Therefore it can be assumed that the velocity is zero above the diffuser, and no flow effects due to the flume are present. The cord was also used in front of the diffuser, here the outflow pattern of the diffuser was clearly visible at the height of the diffuser outlet. But at locations higher than the diffuser outlet, no velocity profile was observed. If there would have been a velocity profile with measured velocities equal to those of the maximum velocity in Figure 7.14, this would have been visible since these are approximately equal to the measured velocities at the diffuser outlet height. Therefore, it can be concluded that these measured velocities are faulty and it is concluded that they are caused by the ADV sensor. While inspecting the velocity data it was noticed that the erroneous velocity profile is present at locations where the amount of particles is low and the SNR value becomes lower than 40dB (see Section 7.1.2). Based on this observation it was chosen that all measured values with an SNR value lower than 40dB would be considered less reliable and shown in red in the velocity profiles. The values with higher SNR values are considered reliable and are shown in black in the velocity profiles.

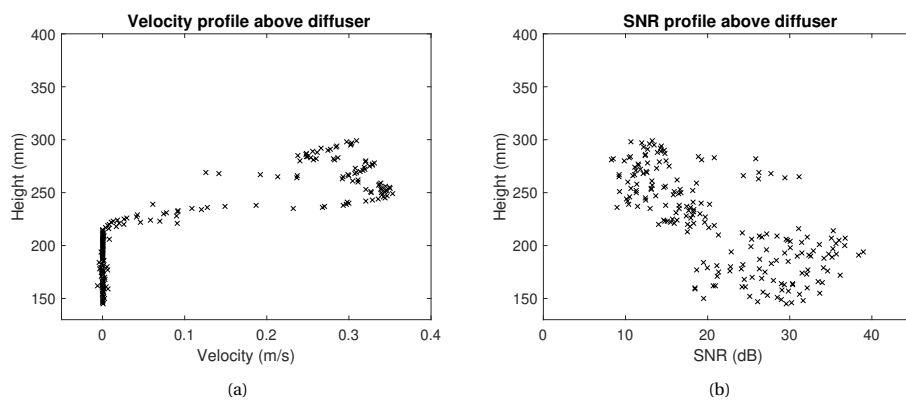


Figure 7.15: Profile of the (a) x velocity and (b) SNR above the diffuser

7.3. Analysis

This section describes the data analysis of the velocity, concentration, bottom deposition pattern and impingement range. The results are analysed based on the offset ratio, $OR = h/D$, where h is the height of the center of the diffuser above the bottom boundary and D is the slot height.

7.3.1. Velocity

The velocity profiles for the tested offset ratios are analysed for each measurement location and both initial velocities. Figure 7.16 and Figure 7.17 show the velocity profiles at different locations for an initial velocity of 0.27m/s and 0.37m/s, respectively. The dotted line shows the boundaries of the diffuser and the red data-points are considered less reliable based on the SNR profile and are therefore not taken into account in this analysis.

The velocity profiles for $u_0=0.27\text{m/s}$ for an offset ratio of 7.33 are shown in Figure 7.16 (a). The Gaussian profile is evident at all measurement locations, and the maximum velocity (or centerline velocity) decreases with increasing distance x/D . The height of the Gaussian profile at $x/D=15$, in this case the height of the density current, since at this location the buoyant jet has already impinged, compared to the other two offset ratios is larger. Since the settling velocity of the particles is equal, this means that it will take longer for the particles to settle, suggesting that the particles will spread further.

The velocity profiles for an offset ratio of 4 are shown in Figure 7.16 (b). At this offset ratio the Gaussian profile is clearly visible at the measurement location closest to the diffuser outlet, $x/D=5$. At the other two measurement locations no Gaussian profile is present. The velocity profile at $x/D=15$ shows a near bottom relative velocity, u/u_0 , of approximately 0.4.

The velocity profiles for an offset ratio of 2.33 are shown in Figure 7.16. Since the buoyant jet impinges at $x/D \approx 1.5$ for this offset ratio and initial velocity (see Appendix A), no Gaussian profile is present. The centerline velocities at $x/D=5$ and $x/D=10$ are visible at $z/D \approx 1$. The centerline velocity at $x/D=10$ is the highest centerline velocity at this measurement location for all offset ratios, however it is unclear how the profile evolves up to the bottom boundary. This is because measurements were stopped at three centimeters above the table. The velocity profile at $x/D=15$ is similar to the velocity profile at this location for an offset ratio of 4, both show a near bottom relative velocity, u/u_0 , of approximately 0.4.

The centerline velocity, the highest velocity below the dotted lines illustrating the diffuser boundaries, at $x/D=5$ is largest for $OR=7.33$ and smallest for $OR=4$. The centerline velocity for $OR=2.33$ is in the middle and a full Gaussian profile is not visible. The near bottom velocity increases with decreasing offset ratio, as would be expected since a lower diffuser height causes the buoyant jet to develop closer to the bottom boundary. However, at measurement location $x/D=15$ the velocity values are similar for an offset ratio of 4 and 2.33.

Figure 7.17 gives the velocity profile for an initial velocity of 0.37m/s. The Gaussian profiles are clearly visible at the first measurement location, $x/D = 5$, for all offset ratios. In this case the centerline velocity is similar for all three offset ratios and the near bottom velocity is highest for an offset ratio of 2.33, at $x/D=5$. At the second measurement location, $x/D=10$, the Gaussian profiles are still visible for an offset ratio of 7.33 and 4, but the location of the profile is lower, indicating the bending of the buoyant jet. The velocity profile for an offset ratio of 2.33 still shows a maximum, but it is not clear what the profile looks like in the last three centimeters to the bottom boundary. Also at this location, the centerline velocities for the three offset ratios are similar in magnitude. For measurement location $x/D = 15$ the velocity profile still has a clear Gaussian profile for an offset ratio of 7.33. For the other two offset ratios the velocity profile shows an increase in velocity towards the bottom, but it is unclear what happens in the last three centimeters above the bottom boundary.

The relative near bottom velocities are approximately 0.4 or 0.6 at $x/D=15$, for an initial velocity of 0.27m/s or 0.37m/s, respectively. This corresponds to a velocity of 0.1m/s for $u_0=0.27\text{m/s}$ and a velocity of 0.2m/s for $u_0=0.37\text{m/s}$. These are the velocities at experiment scale, for the full scale mining operation these velocities will be larger. Both the near bottom velocities at experimental scale and full scale have the potential of resuspending particles [12].

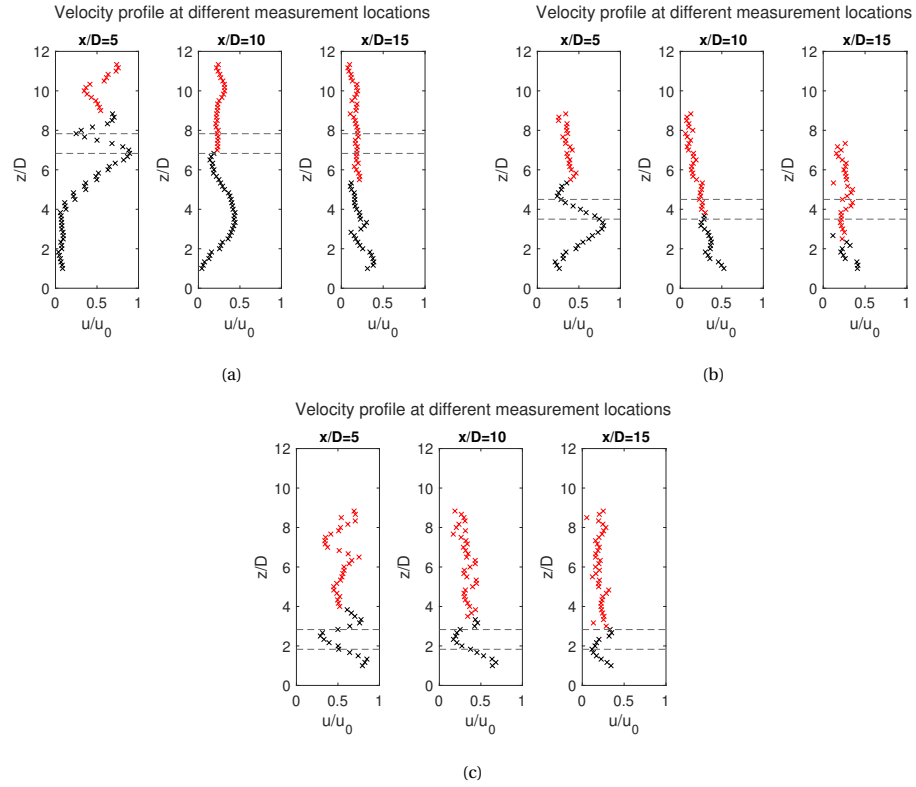


Figure 7.16: Velocity profile at different measurement locations for an offset ratio of (a) OR=7.33, (b) OR=4 and (c) OR=2.33, the dotted lines indicate the diffuser boundaries, the red data points are considered less reliable, $u_0=0.27\text{m/s}$

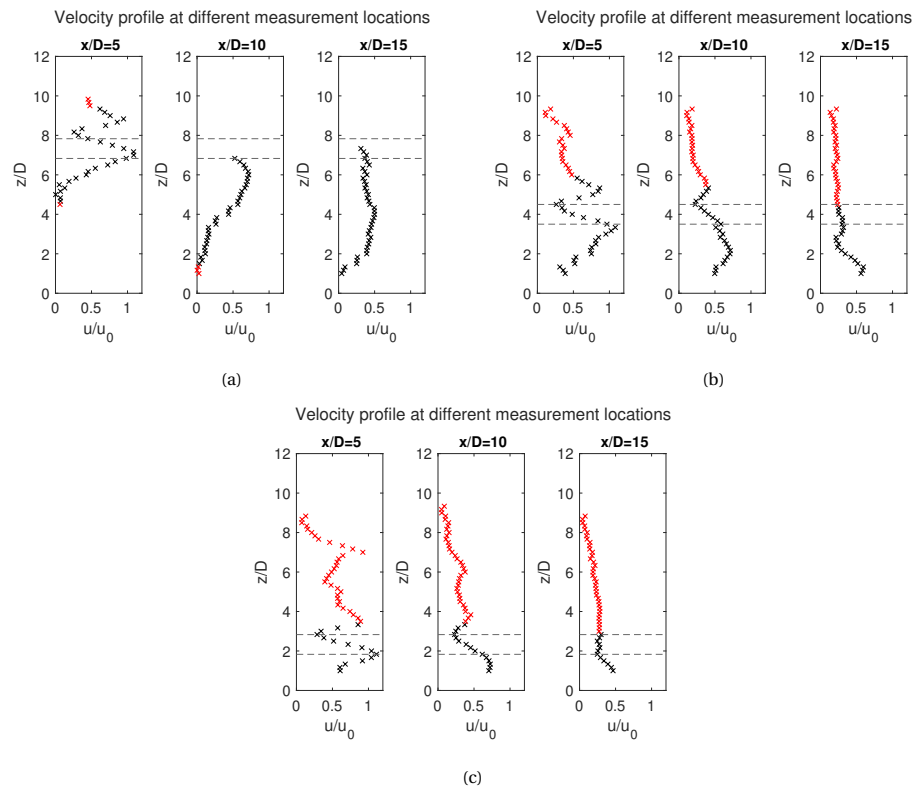


Figure 7.17: Velocity profile at different measurement locations for an offset ratio of (a) OR=7.33, (b) OR=4 and (c) OR=2.33, the dotted lines indicate the diffuser boundaries, the red data points are considered less reliable, $u_0=0.37\text{m/s}$

7.3.2. Concentration

The relative SSC, c/c_0 , is analysed for the three offset ratios and both initial velocities, the resulting graphs are shown in Figure 7.18. It can be seen that for an offset ratio of 2.33, for both initial velocities, the bottom concentration is high and shows a clear maximum with a relative concentration $c/c_0 > 1$. Since the concentration along the centerline is higher than the concentration at the boundaries of a buoyant jet, the maximum indicates the location where the center of the buoyant jet approximately impinges. The measured values are larger than one because the particles have accumulated at the table, where the sample points are located, resulting in a higher concentration than the initial concentration.

For an offset ratio of 7.33 the development of the SSC is similar for both initial velocities, c/c_0 stays low and shows a slight increase around the point where the buoyant jet approximately impinges. A higher diffuser outlet means that it will take longer for the buoyant jet to reach the bottom boundary, therefore the dilution of the buoyant jet will be larger than for a buoyant jet discharge close to the bottom boundary, hence the lower concentration values. In Figure 7.16 and Figure 7.17 it can be noticed that the velocity profiles for OR=7.33, at measurement location $x/D = 5$ and $x/D=10$ are similar. At measurement location $x/D = 15$ the velocity profile for the lower velocity has reached the table, however the velocity profile for the higher velocity has not jet reached the table. This is a difference that can also be noticed in the concentration profile, where for the lower velocity the largest relative concentration is seen just after $x/D = 15$ and for the higher velocity this is at $x/D = 25$.

The offset ratio of 4 shows different behaviour for both initial velocities, for the lower velocity the development is similar to that of OR=7.33, whereas for the higher velocity the behaviour is similar to OR=2.33. This can be explained by looking at the velocity profiles from Figure 7.16 and Figure 7.17. For the lower initial velocity comparing the velocity profiles for the two highest offset ratios shows that the bottom velocities for OR=4 are higher than those for OR=7.33, thus the buoyant jet has reached the bottom. This explains the slightly higher SSC for OR=4 at the first two sample locations. For the higher initial velocity the velocity profile for the two lowest offset ratios show similar near bottom velocities, explaining the similar concentration development.

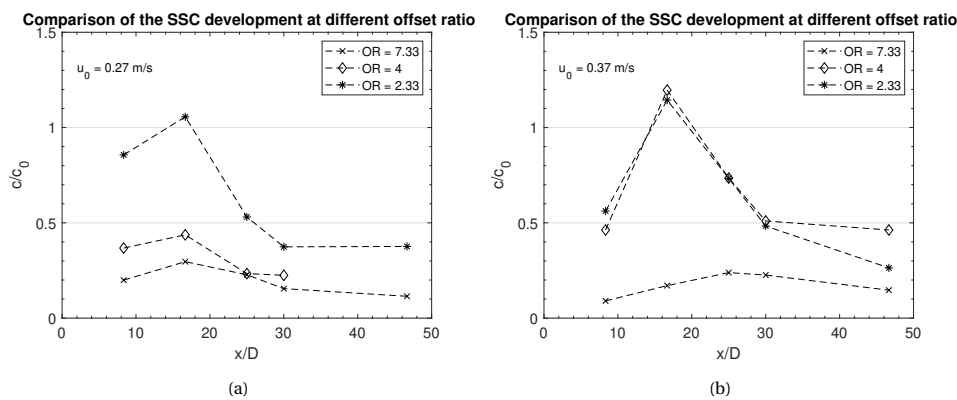


Figure 7.18: SSC at the bottom boundary with increasing distance x/D for different offset ratios and an initial velocity of (a) 0.27m/s and (b) 0.37m/s

7.3.3. Bottom deposition pattern

The bottom deposition pattern at different times and offset ratios is analysed. Figure 7.19 shows the deposition pattern at $t=420$ s for the different offset ratios and the two initial velocities. For an initial velocity of 0.27m/s, the left figure, the width of the bottom deposition is the largest for an offset ratio of 4. The contours for an offset ratio of 2.33 and 4 show an immediate increase in width, indicating that the buoyant jet impinges close to the diffuser outlet. Comparing these contours to the contour for an offset ratio of 7.33 shows a difference until $x/D \approx 17$, the impingement range for this offset ratio starts further away from the source, thus the particles will settle at a larger distance from the source. The right figure, showing the contours for an initial velocity of 0.37m/s, displays similar deposition patterns for all three offset ratios. The increase in width starts at the same distance from the source and the width of the contour is similar as well. This indicates that there

is no significant difference for this velocity when looking at the bottom deposition pattern for different offset ratios.

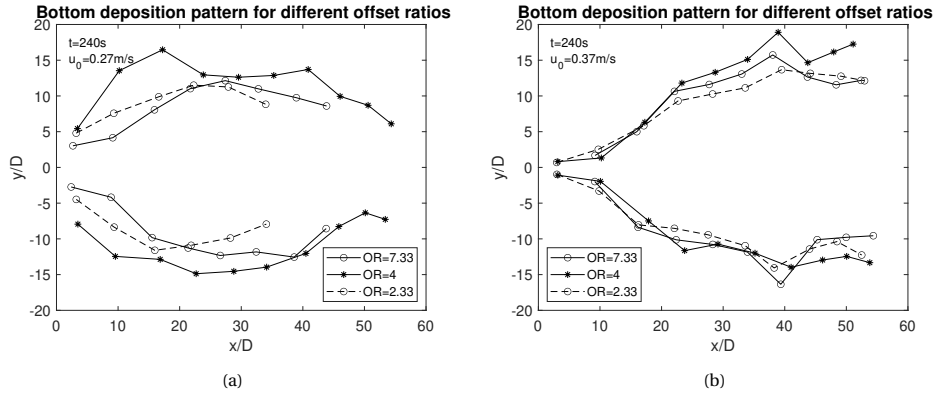


Figure 7.19: Bottom deposition pattern for different offset ratios at $t=240s$, (a) $u_0=0.27m/s$ and (b) $u_0=0.37m/s$

The averaged images used to determine the bottom deposition pattern for an initial velocity of $0.27m/s$ at $t=240s$ are shown in Figure 7.20. The diffuser can be seen at the bottom of each image. The grey area in each image shows the settled particles. A darker area means that more background light is blocked, and thus more particles are present. The buoyant jet can be observed in the first image, OR=7.33, as the straight grey area immediately in front of the diffuser. For the other two images this is less visible, since the buoyant jet impinges closer to the source. It can be noticed that even though the width of the grey area is similar for each offset ratio, the amount of particles is different. For a large offset ratio the least particles are present, indicating that these are spread further away by the density current. The images for an offset ratio of 4 and 2.33 are quite similar, although the grey area for an offset ratio of 2.33 is slightly darker and the darkest area starts closer to the diffuser.

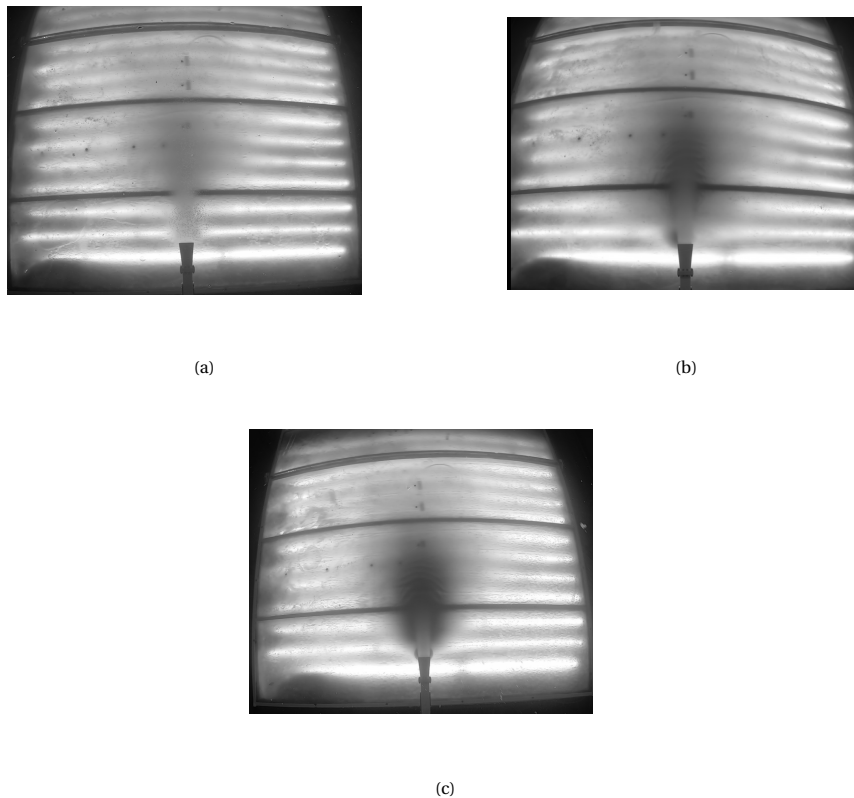


Figure 7.20: Averaged image of the top view of the bottom deposition pattern with an initial velocity of 0.27m/s at $t=420s$, (a) test 8 OR=7.33, (b) test 18 OR=4, and (c) test 26 OR=2.33

7.3.4. Impingement range

Figure 7.21 shows the start of the impingement range for different offset ratios for both tested initial velocities. It can be noticed that the start of the impingement range increases with increasing offset ratio. Also, for an initial velocity of 0.37m/s, increasing the offset ratio from 2.33 to 4 gives a larger increase in x/D than increasing the offset ratio from 4 to 7.33. The same can be said for an initial velocity of 0.27m/s although the difference is smaller. This shows that the start of the impingement range increases with increasing offset ratio, but the increase in impingement range decreases with increasing offset ratio.

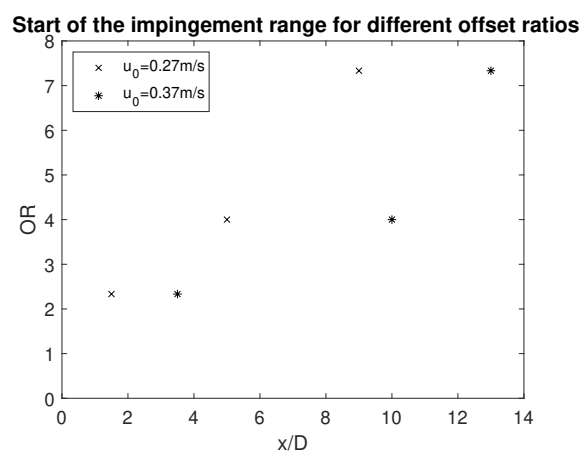
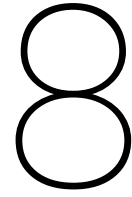


Figure 7.21: Comparison of the start of the impingement range for the three tested offset ratios



Results model

This chapter discusses the results of the model and combines these results with the results of the experiment to validate the model. The initial concentration for all model results shown in this chapter is adapted to the increased reservoir concentration explained in Section 6.8. The figures shown in in this chapter are for $u_0=0.27\text{m/s}$, all graphs for $u_0=0.37\text{m/s}$ are shown in Appendix B.

8.1. Trajectory

The model prediction for the buoyant jet trajectory and width is shown in Figure 8.1, where the bottom boundary is located at $z/D=0$. The datapoints are the locations of the measured centerline velocity during the experiments and give an indication of the centerline trajectory of the buoyant jet during the experiments. It can be noticed that these points are good agreement with the model prediction for all offset ratios. The model prediction of the impingement range shows that the location of the impingement range increases for increasing offset ratios. Furthermore, the width of the impingement range decreases for increasing offset ratios.

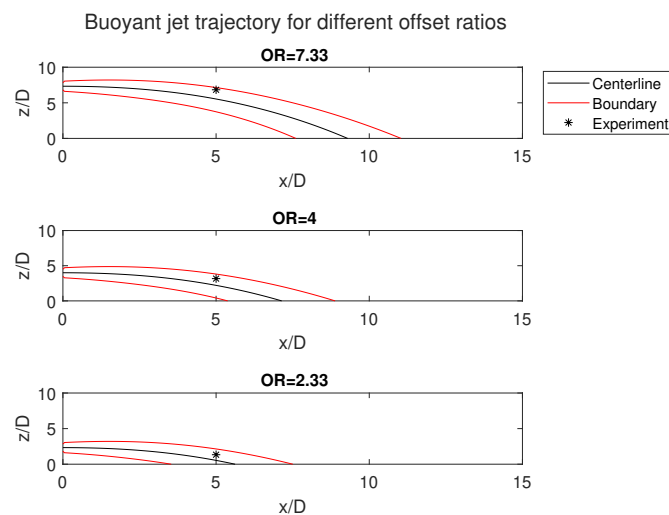


Figure 8.1: Model and experiment results of the buoyant jet trajectory for $u_0=0.27\text{m/s}$

8.2. Suspended sediment concentration

The evolution of the average SSC predicted by the model is shown in Figure 8.2. The average SSC is made dimensionless by the initial concentration and plotted against the length of the buoyant jet trajectory until impingement, s . The datapoints are the concentrations at the impingement point measured during the experiments. It can be noticed that the model prediction and experiment values are in good agreement for an

offset ratio of 7.33 and 4. For an offset ratio of 2.33 the measured concentration is higher. This could be due to the larger accumulation of sediment at the sample location for a low offset ratio. The model prediction shows that the average concentration at impingement decreases with an increasing offset ratio, as is expected since a higher offset ratio means more time for dilution.

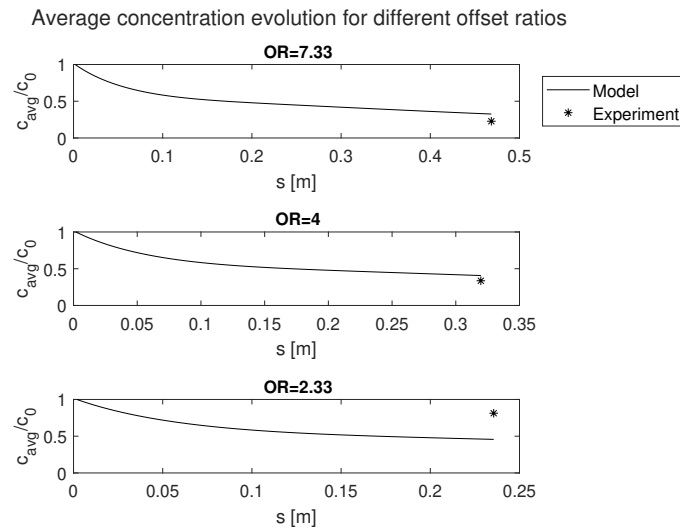


Figure 8.2: Model and experiment results of the average suspended solid concentration for $u_0=0.27$ m/s

8.3. Velocity

The average x-velocity and z-velocity development are shown in Figure 8.3 (a) and (b), respectively. Both are plotted against the length of the buoyant jet trajectory, where the end of the trajectory is the moment the buoyant jet impinges. The datapoints are the average velocities determined by averaging the velocities inside the measured Gaussian profiles of the experiments.

The average x-velocity profile, Figure 8.3 (a), shows that the velocity, u_{avg} , at impingement decreases for an increasing offset ratio. Because it takes longer for the buoyant jet to impinge there is more time for entrainment, decreasing the density difference and causing the velocity to decrease. Because there is no bottom boundary present in the model and the line is cut-off at a given height, the velocity is not zero at the bottom. Comparing the model prediction to the measured datapoints illustrates that they are in good agreement. For a discharge velocity of $u_0=0.37$ m/s the model prediction is still in the same order as the measured values, but the difference is bigger. The standard deviation for the measured velocity is approximately 0.07m/s, which is equal to a standard deviation of approximately $u_{avg}/u_0=0.2$. The model prediction is still inside the standard deviation. Moreover, it is expected that the model overestimates the bending of the buoyant jet because it ignores the interaction between individual particles (see Section 5.1.3). Overestimating the bending in the model implies that the velocity in x-direction would be lower for the model than for the experiment.

The average z-velocity profile, Figure 8.3 (b), shows that the velocity near the bottom boundary increases for an increasing offset ratio, since gravity has more time to accelerate the buoyant jet. It can be noticed that the model prediction overestimates the z-velocity, especially for the second datapoint at an offset ratio of 7.33. The same can be seen for a discharge velocity of $u_0=0.37$ m/s. For both initial velocities the standard deviation of the measurements is approximately 0.03m/s, and it can be noticed that the model prediction lies inside the standard deviation of the measured datapoints for most datapoints. Moreover, it is expected that the model overestimates the bending of the buoyant jet because it ignores the interaction between individual particles (see Section 5.1.3). Overestimating the bending means that the predicted z-velocity would be larger than the measured z-velocity, as is the case in this graph.

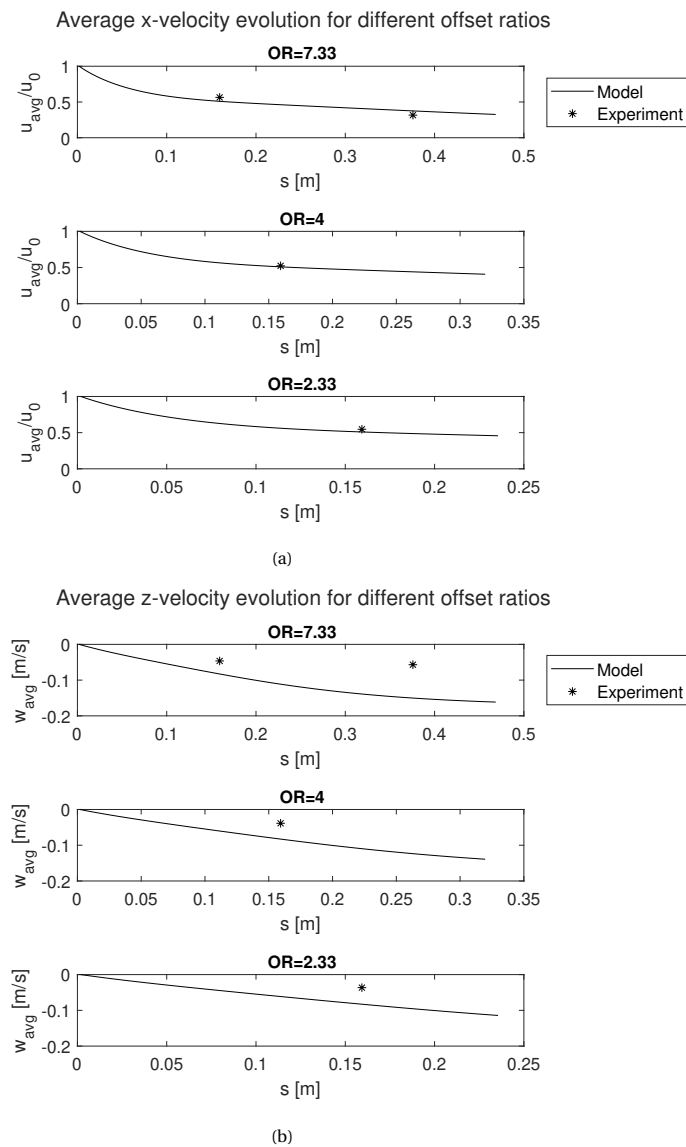


Figure 8.3: Model and experiment results for $u_0=0.27\text{m/s}$, (a) average x-velocity evolution and (b) average z-velocity evolution

8.4. Impingement range

The start of the impingement range is compared to the model prediction, see Table 8.1. Comparing the results of the model with those of the experiments shows that the results are in good agreement. For $u_0=0.27\text{m/s}$ and a diffuser height of 50mm and 100mm, and for $u_0=0.37\text{m/s}$ and a diffuser height of 50mm, the model estimate is larger than the experiment value. This is different than the expectation that the model would overestimate the bending (see Section 5.1.3). This could be explained by the difficulties encountered in determining the impingement range and is only a small difference, maximum $2D$. Moreover, the start of the impingement range is, in this case, the outer boundary of the density current, the actual start of the impingement range will be at larger values of x/D . This would result into a smaller difference between the model and experiment values. For $u_0=0.27\text{m/s}$ and a diffuser height of 200mm, and for $u_0=0.37\text{m/s}$ and a diffuser height of 100mm and 200mm, the model value is smaller than the experiment value. This is in agreement with the expectation that the model would overestimate the bending and would still be the case if the experiment value would be larger than the currently measured value. The estimated difference is at most $3.5D$, and still gives a good first estimate of the impingement of the buoyant jet.

Table 8.1: The start of the impingement range calculated by the model and determined through experiments

u_0 [m/s]	h [mm]	Model x/D	Experiment x/D
0.27	50	3.5	1.5
	100	5.5	5
	200	7.5	9
0.37	50	4	3.5
	100	6.5	10
	200	9.5	13

8.4.1. Deposition width to impingement range ratio

The ratio between the width of the bottom deposition pattern and the predicted length of the impingement range is determined to relate the model prediction to the results of the experiment. This could be used to give an indication of the deposition width when using different input values for the model. The ratios for both tested discharge velocities and all diffuser heights are shown in Table 8.2. These results indicate that multiplying the model prediction of the length of the impingement range with a factor 5 to 6 would give a good first estimate of the width of the bottom deposition.

Table 8.2: Ratio of the deposition width of the experiments over the model prediction of the length of the impingement range

u_0 [m/s]	h [mm]	Ratio [-]
0.27	50	5
	100	7.5
	200	6.5
0.37	50	4
	100	6
	200	5.5

9

Discussion

The objective of the experiments and the model was to investigate the influence of the diffuser height on the spreading of the buoyant jet. This chapter discusses the results, both from the experiments and model. Furthermore, the limitations of the experiments and model and recommendations for further research are discussed.

9.1. Results

The influence of the diffuser height on the velocity, concentration, bottom deposition pattern and impingement range are discussed individually in order to combine the results into a single conclusion in the next chapter.

9.1.1. Velocity

The influence of the diffuser height on the velocity profile of the buoyant jet is similar for both tested discharge velocities. The results of the experiments and model were compared based on the offset ratio, $OR=h/D$, where h is the height of the center of the diffuser above the bottom boundary and D is the slot height. According to the measured velocity profiles of the experiment, the diffuser height influences the magnitude of the centerline velocity of the buoyant jet marginally, therefore it is concluded that the diffuser height does not have a significant influence on the magnitude of the centerline velocity. The velocity profiles show that it takes longer for a buoyant jet discharged at a large offset ratio to impinge than for small offset ratios. Furthermore, the model shows that a lower diffuser height means a higher bottom velocity at impingement. Since the velocity at the lowest three centimeters above the table was not measured during the experiments the conclusion about the bottom velocity is drawn for a height of three centimeters above the table. The velocity profiles measured at this height show that for an offset ratio of 4 and 2.33, the velocity decay and profile are similar. The relative near bottom velocity is approximately 0.4 for $u_0=0.27\text{m/s}$ and 0.6 for $u_0=0.37\text{m/s}$, this corresponds to velocities of 0.1m/s and 0.2m/s, respectively. These velocities are the experimental scale velocities, the full scale velocities will be 0.4m/s and 0.77m/s, respectively. Both have the potential of resuspending particles, since previous research has shown that flow velocities of 0.07m/s will possibly resuspend the settled aggregates [12].

The velocity profiles can be compared to the velocity profiles found by Kishore and Dey (2016) [22] for a submerged offset jet. The evolution of the velocity profile found in this study is similar to that found in these experiments (see Figure 9.1). However, the underlying mechanism is different. In the case of Kishore and Dey a single phase flow is discharged into a fluid of similar density with an initial velocity between 1.1 and 1.8m/s, and the bending of the jet is caused by the Coanda effect. However, in this research a two-phase flow is discharged into a fluid of different density with an initial velocity that is approximately four times smaller, and the bending of the plume is most likely caused by the negative density difference. Despite this difference, the evolution of the velocity profile found in the research into submerged offset jets can be used in the research into the horizontal discharge plume because of their similarities in development. Furthermore, the diffuser outlet and the wall were not aligned in this research. During the mining operation the diffuser will be aligned with the rear of the SMT, which will influence the flow pattern. This will probably create a

recirculation region as was seen in the research of Kishore and Dey, see Figure 9.1 [22]. Depending on the magnitude of the flow in the recirculation region, bottom erosion directly behind the SMT may develop. Due to the flow pattern these particles will mix with the plume, increasing the size of the plume.

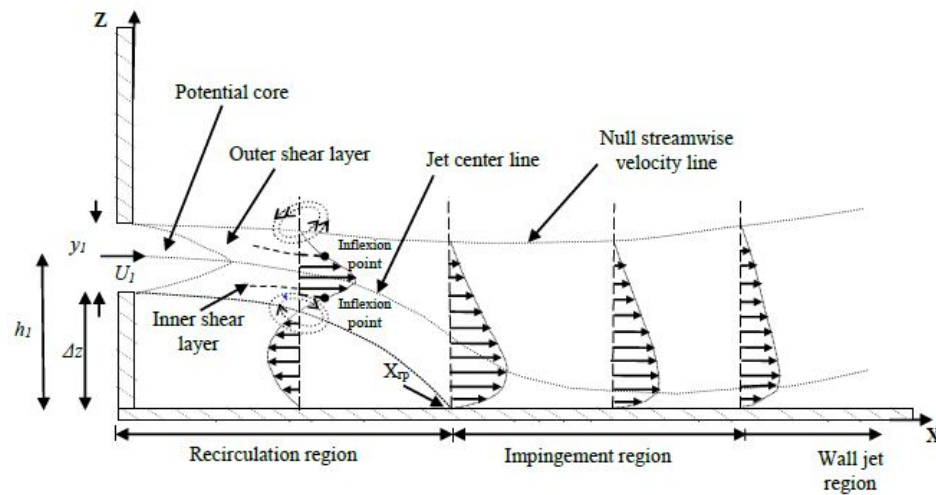


Figure 9.1: Schematic overview of the flow zones in a submerged offset jet [22]

9.1.2. Concentration

Both the experiments and the model show that the bottom concentration increases for a decreasing diffuser height. The sediment concentration during the experiments is determined by taking samples at different locations, these samples are taken one by one. Meaning that the first sample is taken at the beginning of the experiment and the last sample near the end. Since the amount of discharged and settled particles during an experiment increases with time, the measured values might differ from the instantaneous concentration and measurements taken later in the experiment might be higher.

9.1.3. Bottom deposition pattern

The results of the experiment show that for an initial velocity of 0.27m/s and offset ratio of 4, the width of the deposition contour is the largest. For a higher initial velocity the diffuser height has no influence on the lateral spreading of the particles. The images shown in Figure 7.20 indicate that increasing the offset ratio causes particles to spread further away from the source, hence the light grey color in the figure for a large offset ratio. Thus, a small offset ratio means that particles will settle close to the source and therefore less particles will spread further away from the source. The bottom deposition pattern cannot be determined by the model, but a relation between the width of the bottom deposition pattern determined through the experiments and the length of the impingement range predicted by the model can be determined. Multiplying the model prediction of the length of the impingement range with a factor 5 to 6 would give a good first estimate of the width of the bottom deposition.

9.1.4. Impingement range

Both the experiments and the model show that increasing the offset ratio increases the start of the impingement range. However, this influence decreases when the diffuser height is increased. During the experiments, the start and end of the impingement range were difficult to determine because no distinction between the buoyant jet and the density current, that develops in all directions after impingement, could be made. Therefore it was chosen to use the boundary of the density current closest to the diffuser as the start of the impingement range. The actual start of the impingement range is in this case always underestimated.

9.2. Limitations and recommendations

This section discusses the limitations and recommendations of the experiment and the model.

9.2.1. Experiment

The dimensions of the flume influenced the particle choice, the particles chosen for this research are round and coarser than the particles discharged during the mining operation. It was not possible to use finer particles or real sediment, since these would not have settled before the edges of the table. Moreover, the finer particles would reflect of the sidewalls and interfere with the buoyant jet. The sediment mixture discharged by the SMT consists of clay and silt particles suspended in salt water, which have the potential to form flocs that could be beneficial for the deposition of sediment. This could not be tested in this flume because it was not made for salt water testing. Besides, since time was limited in this research the preparation time for these kind of experiments was not acceptable.

During the mining operation, the combination of deep sea sediment and salt water will cause flocculation, resulting in the formation of aggregates containing a large number of single grains. These aggregates have different densities, sizes and shapes than single particles, therefore the settling behaviour of these aggregates is different and they have larger settling velocities. The glass beads used in this research do not form aggregates. Settling velocities in this research are in the order of 0.1m/s, whereas settling velocities of the aggregates are thought to be 0.01m/s for the largest aggregates and 0.0001 m/s for the smallest aggregates [12]. Even though settling velocities are increased by flocculation during the mining operation, compared to this research they are still at least one order in magnitude smaller. Therefore it is expected that the real sediment will spread further than is found in this research.

The experiments in this research were done with a fixed diffuser, however during the mining operation the diffuser will be part of the SMT which is moving at a velocity of approximately 0.5m/s during the discharge of the sediment-water mixture [23]. The movement of the SMT will create a wake, thereby influencing the behaviour of the buoyant jet. CFD simulations have shown that the height of the plume is increased by the wake of the SMT [34]. Due to the increased flow velocity caused by the wake, the velocity inside the buoyant jet will probably increase, resulting in increased spreading of the sediment. Furthermore, depending on the size of the wake and the velocity of the fluid inside the wake, this could potentially resuspend settled particles.

The mixing of the water-particle mixture was done by two submersible pumps located at the bottom of the reservoir. It was found that this caused uneven mixing through the reservoir and caused the initial concentration to be higher than expected. Therefore it is recommended to improve the mixing, this could be done using a system similar to a food or concrete mixer, where the length of the blades cover a large part of the reservoir. This helps create even mixing throughout the reservoir.

The initial SSC in this research is at the higher side of the SSC values expected during deep sea mining. A lower concentration would reduce the buoyancy flux by reducing the mixture density. Due to the reduced buoyancy flux, the velocities inside the plume would be lower as well, resulting into a reduction of the spreading of the sediment.

During the investigation into the cause of the sediment fall-out at the diffuser outlet, it would have been helpful to see the flow inside the diffuser. Although many possible solutions to the problem were investigated, the real cause of the problem was not found. Moreover, the implications of this phenomena on the measurements is not clear. However, comparing the results to the experiments with a higher initial velocity, where the phenomena did not occur, does not show a difference in overall behaviour. Because of the occurrence of this phenomena, it is advised to do further testing with a see-through diffuser, giving more insight in the flow through the diffuser.

During the data analysis it was found that the footage from both the GoPro and the high speed camera were difficult to assess. The quality of the GoPro footage could be enhanced by replacing the current photo paper, which is damaged by the cleaning of the flume. The addition of a second layer of photo paper might help to reduce the visibility of the LED strips in the footage. The high speed camera images could be enhanced by using horizontal light instead of vertical.

A densimetric Froude number inside the subcritical region should be avoided since the experiment showed that the particles will, in this case, hardly settle near the source (see Section 7.1.6). Since the spreading of the buoyant jet needs to be limited, it is beneficial if particles settle close to the source. It is therefore recom-

mended to keep the densimetric Froude number above one.

9.2.2. Model

It was necessary to make certain adaptations and assumptions to the model because modelling the full problem is too complex and time-consuming. Currently no bottom boundary, individual particles, continuous input and possibility to add a current are present in the model. The model validation shows that the model gives a good first estimate of the buoyant jet behaviour. However, a next step would be to add these parts, thereby increasing the accuracy of the model prediction of the buoyant jet behaviour in the region until impingement. Moreover, this model can be used as input for modelling the density current to predict the spreading after impingement.

Conclusion and recommendations

This chapter presents the conclusion and recommendations based on the results, data analysis and discussion presented in the previous chapters.

10.1. Conclusion

The research objective was to investigate the influence of the diffuser height on the behaviour of a horizontally discharged negatively buoyant jet. The main research question to be answered is:

'Can the spreading of the sediment plume, created by a horizontal discharge diffuser, be reduced by the choice of diffuser height above the seafloor?'

To be able to answer the main research question, the conclusions of the sub questions are treated first, after which a conclusion for the main research question is given.

At the moment there are no regulations in place to reduce the environmental impact of the deep sea mining sediment plume. Contractors have to provide proof that enough measurements are taken to limit the environmental impact of their operation.

A buoyant jet develops when a fluid is discharged into an ambient fluid with a continuous source of momentum and buoyancy. In the case of SMT, a negatively buoyant jet is discharged, meaning that there is a negative density difference between the discharged mixture and the ambient fluid. The buoyant jet width increases due to turbulent entrainment of the ambient water by dominant eddies. The entrainment of ambient water also causes dilution of the buoyant jet, thereby decreasing the density difference. The buoyant jet is completely mixed with the ambient fluid when the density difference goes to zero, at this point the momentum and buoyancy values approach the ambient values.

There are several parameters that influence the spreading of the buoyant jet. These parameters can be divided into parameters that can be influenced and parameters that are fixed conditions. The parameters that can be influenced are related to the SMT and can be chosen during the design phase or during operation, these are the SSC, discharge velocity, diffuser geometry and SMT velocity. The fixed conditions are the local conditions, current, temperature, salinity, turbidity, topography and sediment.

The results of the experiment and model suggest that increasing the diffuser height causes the particles to spread further away from the source. Comparing the results based on the offset ratio, h/D , with h the height of the center of the diffuser above the bottom boundary and D the slot height, shows that for an offset ratio of 4 and 2.33 the difference between the results is small. The velocity profiles show that it takes longer for a buoyant jet discharged at a large offset ratio to reach the bottom boundary than for lower offset ratios. Furthermore, the near bottom velocity at experiment scale is 0.1-0.2 m/s, indicating that there is a potential for erosion of settled sediments. The sediment concentration at the bottom boundary shows a lower concentration for a large offset ratio, indicating that most particles do not settle close to the source. Moreover, the bottom de-

position pattern shows no significant difference in width of the pattern, but it does show that a higher offset ratio decreases the amount of settled particles near the diffuser. Increasing the offset ratio also increases the distance to the start of the impingement range, however the amount of increase decreases with increasing offset ratio.

The results of this research suggest that the spreading of the sediment plume can be reduced by the choice of diffuser height above the seafloor. Based on the tested diffuser heights in this research a diffuser height of 100mm is recommended. Since a higher diffuser decreases the amount of particles settling close to the source and a lower diffuser increases the potential for erosion. This research has shown that up to a distance of 15D from the diffuser, the near bottom velocities are large enough to cause erosion. Research into the near bottom velocity decay and magnitude further away from the source, inside the turbidity current, is necessary as well to understand the full spreading behaviour and the potential for erosion.

10.2. Recommendations

The recommendations for future research are given in this section, for further recommendations based on the experiment and model see Section 9.2.

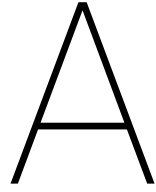
- The false velocity profile above the buoyant jet needs further investigation to find the cause of this limitation of the ADV. It is thought that the false profile is caused by the lack of particles, causing the ADV to measure the velocity profile at the lower measurement heights again. This could be tested by adding particles from the top of the flume and measuring the velocity profile above the buoyant jet.
- Further research into the deep sea mining horizontal discharge plume is recommended. Experiments with finer particles were not possible in this flume, however they are still necessary to gain insight in the behaviour of these small particles in a buoyant jet. Especially the behaviour of the actual deep sea sediment in combination with salt water, causing flocculation, is recommended for future research. Furthermore, research into the influence of the forward velocity of the SMT is necessary, since it is expected to have a large influence on the behaviour of the horizontal discharge plume, due to the creation of a wake.
- During the experiments, the measured velocity profile at the outlet of the diffuser showed a higher average velocity than expected. This is due to the diffuser design, the width expanded while the height was kept constant. However, the end of the expansion is also the outlet of the diffuser, giving the flow velocity no time to adjust. When designing the diffuser, take into account that the flow velocity needs time to decrease, therefore my advice would be to end with a straight section with the dimensions of the wished outlet dimensions. Furthermore, during this research the diffuser showed the potential of bed formation, expanding the height of the diffuser instead of the width of the diffuser would be beneficial for reducing the fall-out of sediment resulting from the bed formation.
- For future research it is recommended to place a screen under the diffuser outlet while testing, simulating the rear of the SMT. This will create an area of reduced entrainment and a near bottom velocity opposite to the discharge velocity, potentially causing bottom erosion directly behind the SMT. Due to the flow pattern these particles will mix with the plume, increasing the size of the plume.

Bibliography

- [1] M.L. Albertson, Y.B. Dai, R.A. Jensen, and H. Rouse. Diffusion of submerged jets. *Transactions of the American Society of Civil Engineers*, 115:639–644, 1950.
- [2] D. Aleynik, A. C. Dale, and M. E. Inall. Near-field hydrodynamic modelling of two case study sites, 2015. URL <https://www.eu-midas.net/library>.
- [3] International Seabed Authority. Environmental management plan for the clarion-clipperton zone, 2011.
- [4] International Seabed Authority. Decision of the council of the international seabed authority relating to amendments to the regulations on prospecting and exploration for polymetallic nodules in the area and related matters, 2013.
- [5] International Seabed Authority, 2019. URL <https://www.isa.org.jm/>.
- [6] K. Cederwall. *Hydraulics of marine wastewater disposal*, volume 42. Chalmers Institute of Technology, Hydraulics Div., Sweden, 1968. ISBN 978-007-247236-3.
- [7] H. Chen. *Turbulent Buoyant Jets and Plumes in Flowing Ambient Environments*. PhD thesis, Aalborg University, Denmark, 1991.
- [8] Y. A. Cimbala and J. M. Çengel. *Fluid Mechanics: Fundamentals and Applications*, volume 1. McGraw-Hill, 2006. ISBN 978-007-247236-3.
- [9] H. J. S. Fernando. *Handbook of Environmental Fluid Dynamics; Overview and fundamentals*, volume 1. CRC Press, 2013. ISBN 978-1-4398-1669-1.
- [10] H. B. Fischer, E. J. List, R. C. Y. Koh, J. Imberger, and N. H. Brooks. *Mixing in Inland and Coastal Waters*. Academic Press, 1979. ISBN 978-0-0805-1177-1. doi: 10.1016/B978-0-08-051177-1.50001-5.
- [11] Bundesanstalt für Geowissenschaften und Rohstoffe. Environmental impact assessment, 2018.
- [12] B. Gillard, K. Purkiani, D. Chatzievangelou, A. Vink, M. Iversen, and L. Thomsen. Physical and hydrodynamic properties of deep sea mining-generated, abyssal sediment plumes in the clarion clipperon fracture zone (eastern-central pacific). *Elementa Science of the Anthropocene*, 7, 01 2019. doi: 10.1525/elementa.343.
- [13] K. M. Gjerde, P. Weaver, D. Billett, G. Paterson, A. Colaco, A. Dale, J. Greinert, C. Hauton, F. Jansen, P. M. Arbizu, K. Murphy, and A. Sweetman. Report on the implications of midas results for policy makers with recommendations for future regulations to be adopted by the eu and the isa, 2016. URL <https://www.eu-midas.net/library>.
- [14] S. K. Haldar. *Mineral Exploration*, pages 85–101. Elsevier, 2018. ISBN 9780128140222. doi: 10.1016/B978-0-12-814022-2.00005-8.
- [15] S. Hong, H. Kim, J. Choi, T. Yeu, S. Park, C. Lee, and S. Yoon. A self-propelled deep-seabed miner and lessons from shallow water tests. In *Proceedings of the International Conference on Offshore Mechanics and Arctic Engineering - OMAE*, volume 3, 01 2010. doi: 10.1115/OMAE2010-20313.
- [16] Google Images, 2019. URL https://www.google.com/search?q=flow+separation+adverse+pressure+gradient&rlz=1C1SQJL_n1NL861NL861&source=lnms&tbm=isch&sa=X&ved=2ahUKEwjRpaCosuzoAhUPzqQKHQMTDKIQ_AUoAXoECBQQAw&biw=1536&bih=754#imgrc=in7XuNZrHyyXIM&imgdii=ia5JDKDdEdVwqM.

- [17] J. A. Jankowski and W. Zielke. The mesoscale sediment transport due to technical activities in the deep sea. *Deep Sea Research Part II: Topical Studies in Oceanography*, 48(17):3487 – 3521, 2001. ISSN 0967-0645. doi: [https://doi.org/10.1016/S0967-0645\(01\)00054-6](https://doi.org/10.1016/S0967-0645(01)00054-6). URL <http://www.sciencedirect.com/science/article/pii/S0967064501000546>. Environmental Impact Studies for the Mining of Poly-metallic Nodules from the Deep Sea.
- [18] J. A. Jankowski and W. Zielke. Data support for modelling of deep-sea mining impacts, 2011.
- [19] J. A. Jankowski, A. Malcherek, and W. Zielke. Numerical modeling of suspended sediment due to deep-sea mining. *Journal of Geophysical Research*, 101:3545–3560, 02 1995. doi: 10.1029/95JC03564.
- [20] D. O. B. Jones, S. Kaiser, A. K. Sweetman, C. R. Smith, L. Menot, A. Vink, D. Trueblood, J. Greinert, D. S. M. Billett, P. M. Arbizu, T. Radziejewska, R. Singh, B. Ingole, T. Stratmann, E. Simon-Lledó, J. M. Durden, and M. R. Clark. Biological responses to disturbance from simulated deep-sea poly-metallic nodule mining. *PLOS ONE*, 12, 02 2017. doi: 10.1371/journal.pone.0171750. URL <https://doi.org/10.1371/journal.pone.0171750>.
- [21] Sreenivas K R and Ajay Prasad. Vortex-dynamics model for entrainment in jets and plumes. *Physics of Fluids*, 12, 08 2000. doi: 10.1063/1.870455.
- [22] G. R. Kishore and S. Dey. Hydraulics of submerged offset-jets. In *6th IAHR International Symposium on Hydraulic Structures*, pages 407–416, Portland, Oregon, 2016. doi: 10.15142/T3550628160853.
- [23] A. M. Lang, S. Dasselaar, K. Aasly, and E. Larsen. Report describing the process flow overview. Technical report, Blue Nodules, 2019.
- [24] J. H. W. Lee and V. Cheung. Generalized lagrangian model for buoyant jets in current. *Journal of Environmental Engineering*, 116(6):1085–1106, 1990. doi: [https://doi.org/10.1061/\(ASCE\)0733-9372\(1990\)116:6\(1085\)](https://doi.org/10.1061/(ASCE)0733-9372(1990)116:6(1085)).
- [25] J. H. W. Lee and V. H. Chu. *Turbulent jets and plumes: a Lagrangian approach*. Springer Science+Business Media, 2003. ISBN 978-1-4613-5061-3. doi: 10.1007/978-1-4615-0407-8.
- [26] J. H. W. Lee, V. Cheung, W. P. Wang, and S. K. B. Cheung. Lagrangian modeling and visualization of rosette outfall plumes. In *Proc. Hydrodynamics 2000*, pages 23–27, 2000.
- [27] W. Y. Lee, A. C. Y. Li, and J. H. W. Lee. Structure of a horizontal sediment-laden momentum jet. *Journal of Hydraulic Engineering*, 139:124–140, 02 2013. doi: 10.1061/(ASCE)HY.1943-7900.0000662.
- [28] P. Liu and K.M. Lam. Two-phase velocity measurement in a particle-laden jet. *Journal of Hydro-environment Research*, 7(1):18 – 29, 2013. ISSN 1570-6443. doi: <https://doi.org/10.1016/j.jher.2012.08.001>. URL <http://www.sciencedirect.com/science/article/pii/S1570644312000731>.
- [29] V. Matoušek. Delf university of technology, lecture notes: Dredge pumps and slurry transport, 2004.
- [30] MIDAS. Research highlights, 2016. URL <https://www.eu-midas.net/library>.
- [31] K. A. Miller, K. F. Thompson, P. Johnston, and D. Santillo. An overview of seabed mining including the current state of development, environmental impacts, and knowledge gaps. *Frontiers in Marine Science*, 4:418, 2018. ISSN 2296-7745. doi: 10.3389/fmars.2017.00418. URL <https://www.frontiersin.org/article/10.3389/fmars.2017.00418>.
- [32] Taylor G.I. Morton, B.R. and J.S. Turner. Turbulent gravitational convection from maintained and instantaneous sources. *Proc. Royal Soc.*, A234:1–23, 1956. doi: <https://doi.org/10.1098/rspa.1956.0011>.
- [33] Nortek. The comprehensive manual for velocimeters, 2018.
- [34] Global Sea Mineral Resources NV. Environmental impact statement, 2018.
- [35] Secretariat of the Pacific Community. Deep sea minerals: Manganese nodules, a physical, biological, environmental, and technical review. Technical report, SPC, 2013.

- [36] I. Papakonstantis and E. Tsatsara. Trajectory characteristics of inclined turbulent dense jets. *Environmental Processes*, 5, 05 2018. doi: 10.1007/s40710-018-0307-6.
- [37] N. Rajaratnam and K. Subrarnanya. Plane turbulent reattached wall jets. *Journal of the Hydraulics Division*, 94(1):95–112, 1968.
- [38] World Ocean Review, 2014. URL <https://worldoceanreview.com/en/wor-3/mineral-resources/manganese-nodules/>.
- [39] O. E. Sequeiros. Estimating turbidity current conditions from channel morphology: A froude number approach. *Journal of Geophysical Research: Oceans*, 117(C4), 2012. doi: 10.1029/2011JC007201. URL <https://agupubs.onlinelibrary.wiley.com/doi/abs/10.1029/2011JC007201>.
- [40] E. Simon-Lledó, B. J. Bett, V. A. I. Huvenne, T. Schoening, N. M.A. Benoist, R. M. Jeffreys, J. M. Durden, and D. O. B. Jones. Megafaunal variation in the abyssal landscape of the clarion clipperton zone. *Progress in Oceanography*, 170:119 – 133, 2019. ISSN 0079-6611. doi: <https://doi.org/10.1016/j.pocean.2018.11.003>. URL <http://www.sciencedirect.com/science/article/pii/S0079661118301824>.
- [41] Lab Unlimited, 2013. URL <https://www.labunlimited.com/s/ALL/4AJ-9920492/Aqualytic-turbidimeter-Turbi-Direct-4194000>.
- [42] F. M. White. *Fluid Mechanics*, volume 6. McGraw-Hill, 2009. ISBN 978-007-127038-0.
- [43] T. Yamazaki, B. Barnett, and T. Suzuki. Optical determination of the jet deep sea sediment disturbance. In *Proceedings of the International Symposium on Environmental Studies of Deep-Sea Mining*, pages 153–168. Metal Mining Agency of Japan, 1997.



Results experiment

A.1. Concentration

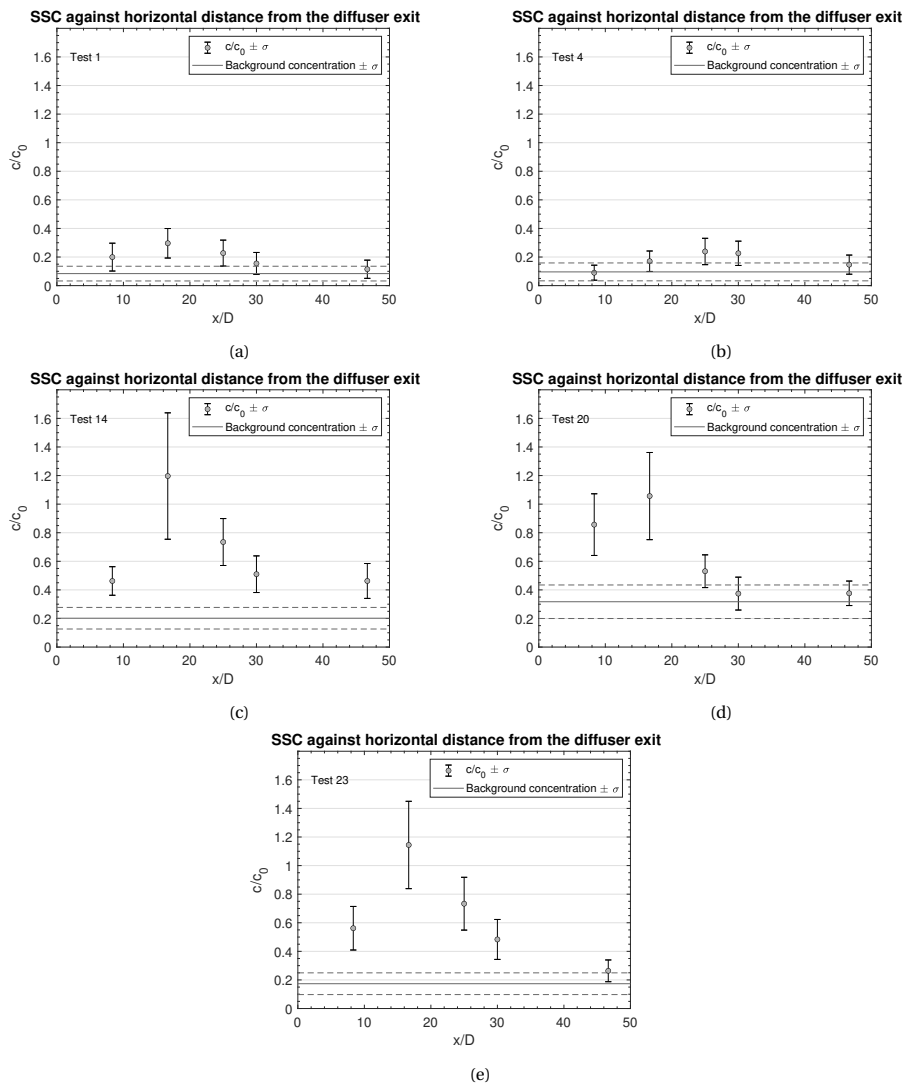


Figure A.1: Dimensionless SSC at the sample locations 1, 2, 3, 4 and 5 compared to the background concentration for (a) experiment 1, $h=200$ mm and $u_0 = 0.27$ m/s, (b) experiment 4, $h=200$ mm and $u_0 = 0.37$ m/s, (c) experiment 14, $h=100$ mm and $u_0 = 0.37$ m/s, (d) experiment 20, $h=50$ mm and $u_0 = 0.27$ m/s, and (e) experiment 23 $h=50$ mm and $u_0 = 0.37$ m/s

A.2. Velocity

A.2.1. SNR profile

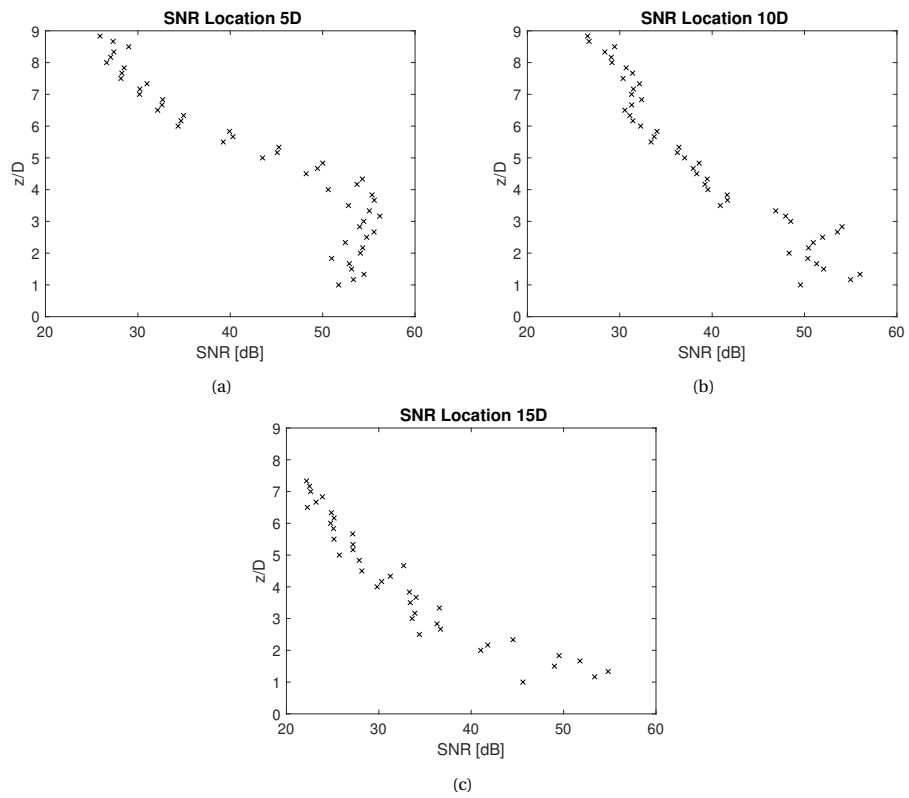


Figure A.2: SNR profile for (a) test 10, (b) test 11 and (c) test 12

A.2.2. Velocity profile

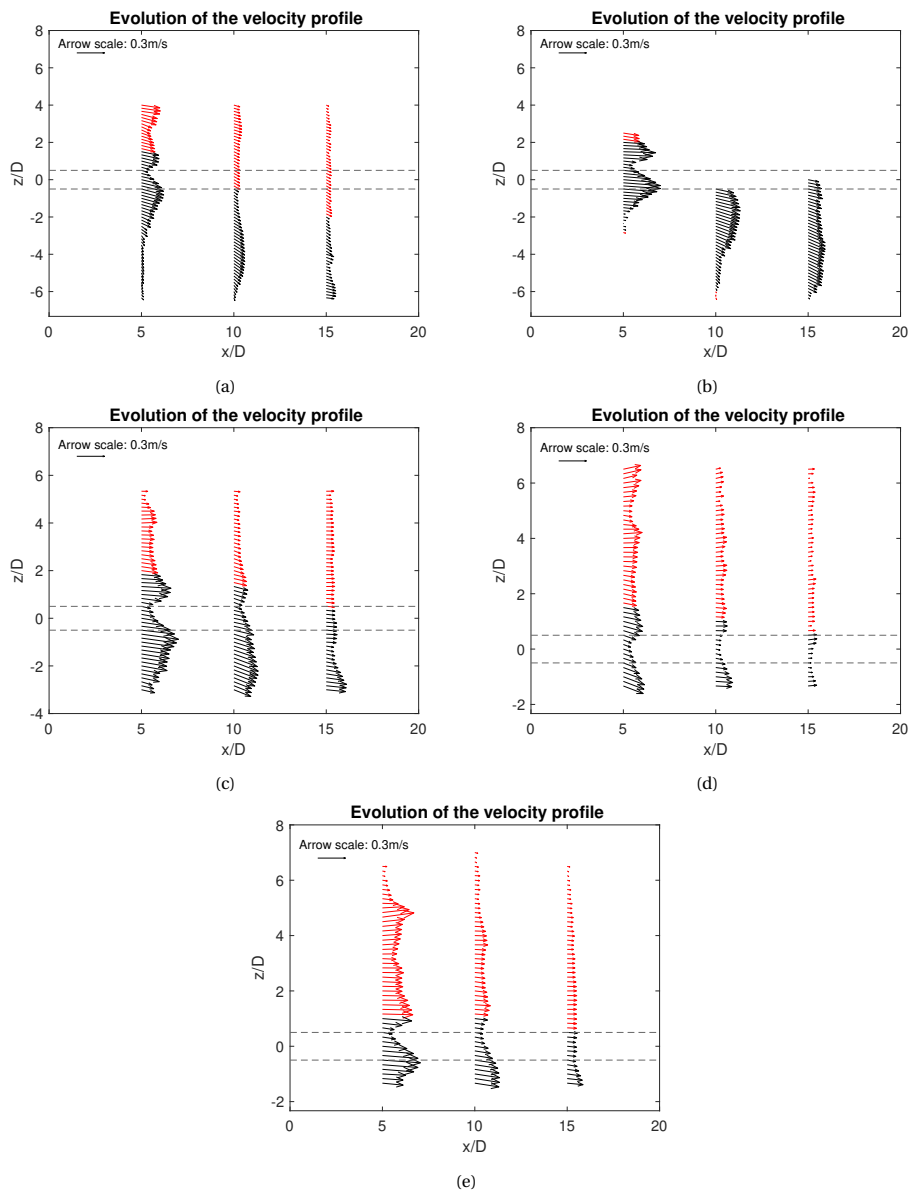


Figure A.3: Velocity profile at different measurement locations for (a) test 1, 2 and 3, (b) test 4, 5 and 6, (c) 14, 15 and 16, (d) 20, 21 and 22, and (e) 23, 24 and 25; where the dotted lines indicate the diffuser boundaries

A.3. Bottom deposition pattern

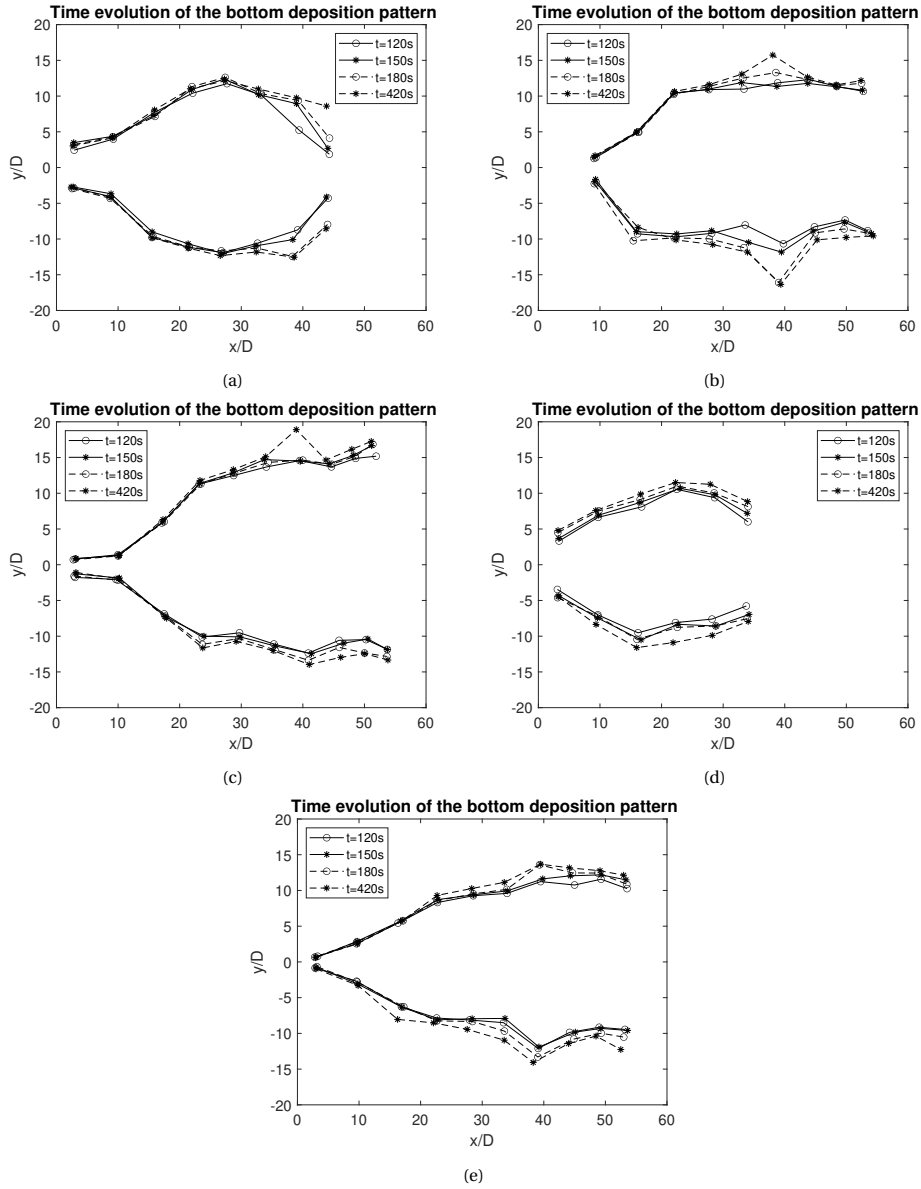


Figure A.4: Time evolution of the bottom deposition pattern for (a) test 8, $h=200mm$ and $u_0=0.27m/s$, (b) test 9, $h=200mm$ and $u_0=0.37m/s$, (c) test 19, $h=100mm$ and $u_0=0.37m/s$, (d) test 26, $h=50mm$ and $u_0=0.27m/s$, and (e) test 27, $h=50mm$ and $u_0=0.37m/s$

A.4. Impingement range

Table A.1: Approximate start of the impingement range (x/D) for different experiments, with in red the experiments for a particle size of 40-70 micron

Experiment	h [mm]	u_0 [m/s]	x/D
8	200	0.27	9
9	200	0.37	13
18	100	0.27	5
19	100	0.37	10
26	50	0.27	1.5
27	50	0.37	3.5
30	100	0.27	3.5
31	100	0.37	11

B

Results model

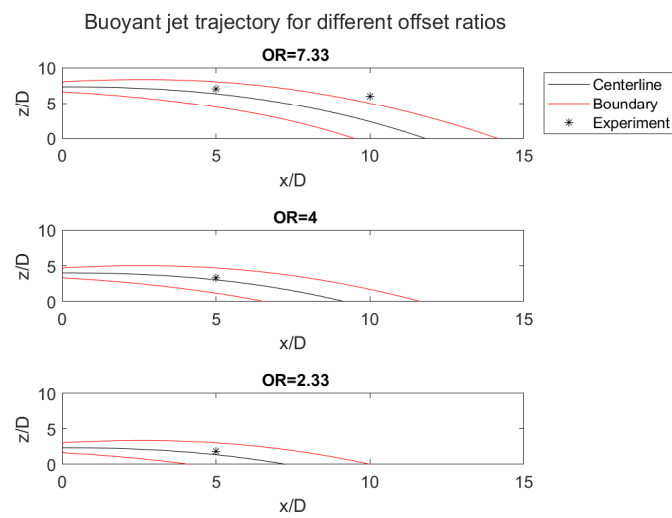


Figure B.1: Model and experiment results of the buoyant jet trajectory for $u_0=0.37\text{m/s}$

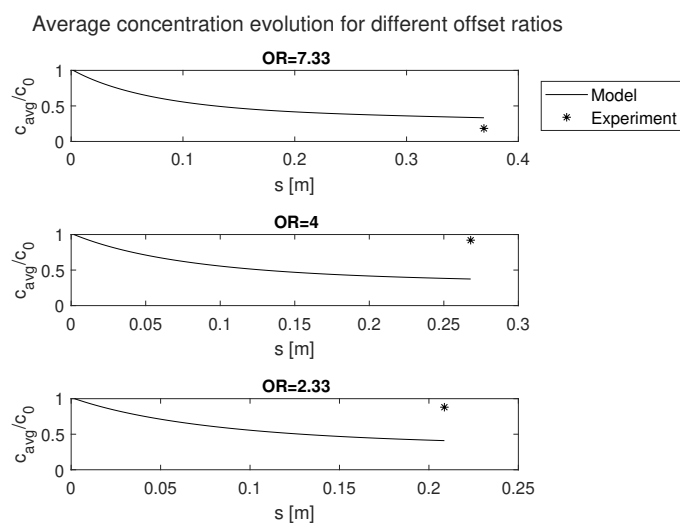


Figure B.2: Model and experiment results of the average suspended solid concentration for $u_0=0.37\text{m/s}$

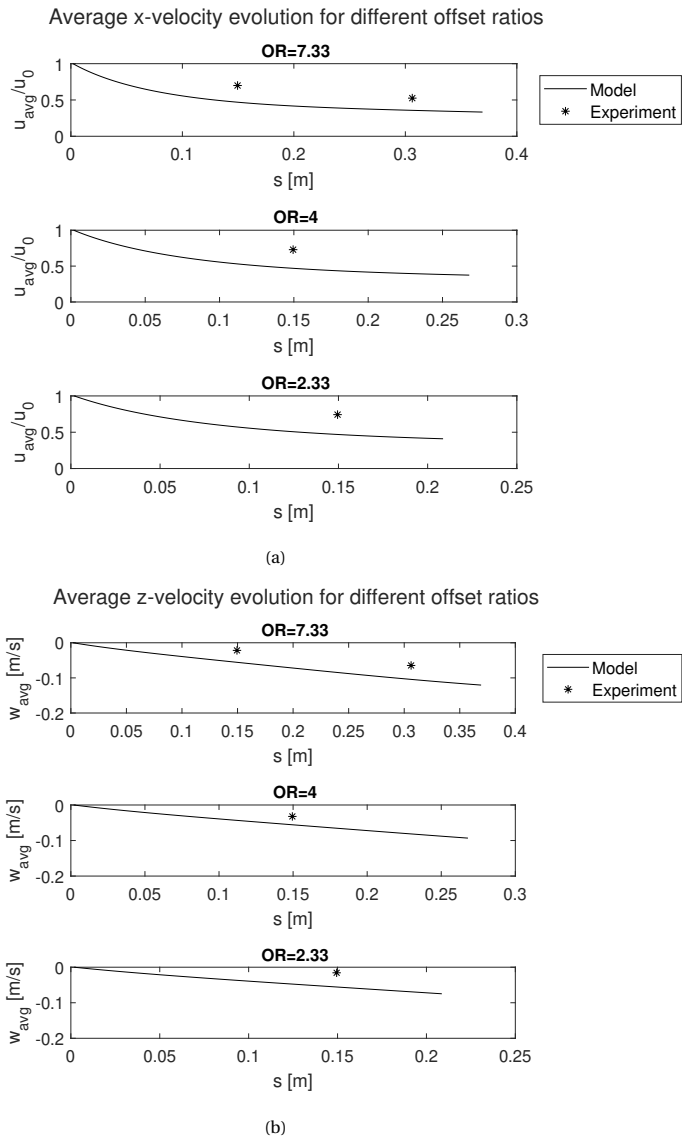


Figure B.3: Model and experiment results for $u_0=0.37\text{m/s}$, (a) average x-velocity evolution, and (b) average z-velocity evolution